



DISSERTATION

Short period ocean tidal variations in Earth rotation

Ausgeführt zum Zwecke der Erlangung des akademischen Grades eines Doktors der technischen
Wissenschaften unter der Leitung von

Univ.-Prof. Dipl.-Ing. Dr.techn. Johannes Böhm
E 120-4
Department für Geodäsie und Geoinformation

eingereicht an der Technischen Universität Wien
Fakultät für Mathematik und Geoinformation

von

Dipl.-Ing. Matthias Madzak

Matr.-Nr.: 0525011
Stadlauerstraße 53/12
1220 Wien

Acknowledgments

I want to thank my supervisor Johannes Böhm for all the support and freedom throughout my academic career and for being open to all my questions, ideas and concerns.

Wolfgang Bosch did not just introduce the oceanographers world to me, he also encouraged my writing with all his knowledge, experience and serenity.

The scientific community, in particular the team at Goddard, showed me numerous intriguing and beautiful aspects of Geosciences, which still fascinate me.

I very much appreciate my colleagues and friends for making the last years a really great time.

Special thanks go to Reimar for challenging me wherever he can, and supporting me readily, and Nina, whom I do not want to miss both in my private and working life.

And to my parents, who care.

Thank you!

Abstract

Profound knowledge of the variable Earth rotation is required to derive accurate and reliable statements and parameters from space geodetic techniques. The geophysical know-how, which forms the basis of Earth rotation studies, benefits in turn from precise measurements and time-series of Earth rotation parameters (ERP). They allow science to broaden the expertise in the field of dynamic processes and interactions of the system Earth and thereby to improve global geophysical models. This dissertation deals with Earth rotation variations in the diurnal and sub-diurnal frequency range with the main objective of developing a new high-frequency ERP prediction model. It should, furthermore, answer the question, if an empirical ocean tide model, being the most independent data source, can be used to derive accurate ERP predictions which could potentially replace the current conventional model.

The conventional prediction model for short-period ocean tidal effects on Earth rotation recommended by the International Earth Rotation and Reference Systems Service (IERS) has been found to yield imperfect geodetic results and introduces biases in Global Positioning System (GPS) orbits. An updated model for polar motion and Universal Time 1 (UT1) is, therefore, highly desirable by the scientific community. Due to the high precision of measurements, several empirical ERP models have been developed by harmonic analysis of the residuals of space geodetic techniques. However, they lack of independence, and single-technique models differ in inter-technique comparisons. There are, in addition, combination models determined from several techniques, presumed to be the most precise models currently available. On the other hand, ocean tide models have been improving over the last decades and may serve as input to an independent ERP prediction model. The present thesis addresses the pivotal question of whether an empirical ocean tide model may be used for the development of an high-frequency ERP model and seeks to detect challenges and limitations thereof.

As empirical ocean tide models do not include any hydrodynamic equations, the determination of consistent oceanic tidal currents is one major task addressed in this dissertation. An algorithm based on simplified momentum equations and continuity constraints is developed to derive barotropic volume transports and, therewith, motion terms of oceanic tidal angular momentum (OTAM). The resultant OTAM values indicate the necessity for different weights of the continuity equation for different components. Equatorial components of diurnal tides require a large weight of 10000 compared to weights between 400 and 800 for the polar component. Semi-diurnal tides, on the other hand, show reasonable results for smaller weights between 100 and 200 for the equatorial components and between 400 to 2000 for polar components. If these variable weights are used, OTAM from estimated volume transports and assimilation models differ by 4.7–19.7% (mean over x-, y-, and z-component).

A final model, based on the empirical ocean tide model EOT11a, supplemented by ten additional tidal constituents through quadratic admittance interpolation of angular momentum val-

ues, is derived and used as a priori model in the analysis of Very Long Baseline Interferometry (VLBI) observations. In a comparison with other types of high-frequency ERP models, VLBI data between 2011 and 2013 are analyzed using the Vienna VLBI Software. Post-fit ERP residual spectra and baseline length repeatabilities are calculated in order to validate four models. The results show that the empirical ERP model yields superior results than those based on ocean tide models. It improves the majority of baselines regarding their repeatabilities and gives generally smallest ERP residuals.

The model based on empirical ocean tides is found to perform similarly accurate as the IERS conventional model with respect to baseline length repeatabilities. When using the empirical ERP model as reference, the newly derived model shows smaller baseline length variations for 40% of all 161 baselines, the conventional model improves 41%. For the comparison of post-fit residual spectra, the EOT11a-based model yields smaller amplitudes for more tidal frequencies than the conventional model and the same number as the empirical model. However, three main tidal constituents show a significant degradation with respect to post-fit residual spectra. Given that a similar behavior is visible for another ERP model based on ocean tides, imperfect hydrodynamic modeling or observational inaccuracies of altimetry are possible causes. These findings emphasize the need for further studies on high-frequency ERP predictions. An independent and consistently derived model, such as the one developed in the present work, may serve as new reference for diurnal and sub-diurnal polar motion and UT1 variations in the analysis of space geodetic techniques.

Kurzfassung

Fundierte Kenntnisse über Erdrotationsschwankungen tragen maßgeblich zur genauen und zuverlässigen Parameterschätzung aus geodätischen Weltraumverfahren bei. Die geophysikalischen Grundlagen bilden die Basis zur wissenschaftlichen Vertiefung auf diesem Gebiet. Vice versa profitieren sie von präzisen Beobachtungen und Messungen der Erdrotationsparameter. Deren Zeitserien erlauben es der Wissenschaft, das Verständnis über globale dynamische Prozesse sowie Interaktionen des Systems Erde zu erweitern und damit globale geophysikalische Modelle zu entwickeln. Die vorliegende Dissertation befasst sich mit Erdrotationsschwankungen im täglichen und subtäglichen Bereich und der Entwicklung eines neuen Vorhersagemodells für kurzperiodische Änderungen der Erdrotation. Außerdem wird versucht die Frage zu beantworten, ob ein empirisches Modell der Meereszeiten herangezogen werden kann, um ein genaues Erdrotationsmodell zu entwickeln und damit das aktuelle Standardmodell zu ersetzen.

Das konventionelle Vorhersagemodell des internationalen Erdrotationsdienstes (IERS) für kurzperiodische Erdrotationsschwankungen weist Defizite bei der Berechnung von geodätischen Größen auf und erzeugt systematische Abweichungen bei der GPS-Bahnbestimmung. Ein neues, verbessertes Modell für Polbewegung und Drehgeschwindigkeit der Erde wird daher von wissenschaftlicher Seite gefordert. Wegen der hohen Präzision heutiger Messungen mit modernen geodätischen Weltraumverfahren gewinnen empirische Modelle immer mehr an Bedeutung. Sie stellen allerdings keine unabhängigen Datenquellen dar und liefern oftmals nur für das Raumverfahren, aus dem sie abgeleitet werden, gute Ergebnisse. Allerdings deuten Studien auf eine sehr gute Übereinstimmung zwischen kombinierten Modellen aus Beobachtungen verschiedener Verfahren hin. Auch Modelle für Meereszeiten haben in den letzten Jahren Fortschritte hinsichtlich Genauigkeit, räumlicher Auflösung und Konsistenz erzielt und bilden so eine mögliche Grundlage zur Entwicklung eines unabhängigen Erdrotationsmodells. Die vorgestellte Arbeit umfasst die notwendigen Arbeitsschritte zur Entwicklung eines Erdrotationsmodells basierend auf empirischen Meereszeiten und zeigt diesbezügliche Probleme und Einschränkungen auf.

Da empirische Modelle für Meereszeiten nicht mittels hydrodynamischer Modellierung berechnet werden, müssen konsistente Strömungen aus vorhandenen Höhenvariationen der Meeresoberfläche abgeleitet werden. Die Entwicklung eines Algorithmus zur hydrodynamischen Bestimmung von barotropen, horizontalen Geschwindigkeiten stellt daher einen gewichtigen Teil dieser Arbeit dar. Die aus den Geschwindigkeiten abgeleiteten Relativedrehimpulse legen nahe, die Kontinuitätsgleichung für verschiedene Komponenten unterschiedlich zu gewichten. Äquatoriale Komponenten von täglichen Partialtiden zeigen größere Übereinstimmung mit Relativedrehimpulsen aus hydrodynamischen Modellen bei großen Gewichten von 10000. Für die polare Komponente wird ein Gewicht zwischen 400 und 800 verwendet. Halbtägliche Partialtiden zeigen bereits für geringere Gewichte zwischen 100 und 200 für äquatoriale und 400 und 2000 für polare Komponenten die größte Übereinstimmung. Die Relativedrehimpulse unterscheiden sich

dann von jenen mit hydrodynamischen Modellen gerechneten um 4.7–19.7% (Mittelwert über x-, y- und z-Komponenten).

Das finale Modell basiert auf Daten des empirischen Meereszeitenmodells EOT11a und wird um zehn Partialtiden mittels quadratischer Interpolation der Drehimpulsfunktionen erweitert. Für die Validierung werden VLBI-Beobachtungen der Jahre 2011–2013 mit der Vienna VLBI Software ausgewertet. ERP Residuenspektren werden für vier Validierungsmodelle ebenso abgeleitet wie Wiederholbarkeiten von Basislinienlängen. Die Ergebnisse zeigen einen Genauigkeitsvorsprung des empirischen ERP Modells gegenüber den anderen. Es minimiert im Allgemeinen sowohl die post-fit Residuen der Erdrotationsparameter als auch die Wiederholbarkeit der Basislinien.

Das neu entwickelte Modell basiert auf empirischen Meereszeiten und verbessert die Basislängen-Wiederholbarkeit in vergleichbarem Ausmaß wie das konventionelle Modell des IERS. Mit dem empirischen Modell als Referenz verbessert das neue Modell 40% aller 161 Basislinien, das konventionelle Modell 41%. Im Vergleich der Residuenspektren schneidet das EOT11a-basierte Modell ebenfalls ähnlich wie das konventionelle Modell ab. Größere Diskrepanzen sind an Frequenzen von drei Haupttiden zu erkennen. Da ein weiteres, ebenfalls auf Altimetrie-Beobachtungen basierendes Modell ähnliche Abweichungen aufweist, sind Fehler bei der hydrodynamischen Modellierung und Messungenauigkeiten der Altimetrie mögliche Ursachen. Diese Ergebnisse unterstreichen die Wichtigkeit eines unabhängigen und konsistent abgeleiteten Modells, wie jenes in dieser Arbeit vorgestellte, für die Vorhersage von kurzperiodischen Erdrotationsschwankungen in der Auswertung von geodätischen Weltraumverfahren.

Contents

1	Introduction	1
1.1	The Earth's variable rotation	1
1.2	Motivation and objectives of this study	2
1.3	Outline of the thesis	3
2	Earth rotation variations	5
2.1	Reference systems and Earth orientation	5
2.2	Observed and modeled Earth rotation variations	8
2.2.1	Earth rotation velocity	8
2.2.2	Orientation of the Earth rotation axis	9
2.3	Geophysical excitation of Earth rotation	11
2.4	Observations of Earth rotation variations	16
2.4.1	Very Long Baseline Interferometry	16
2.4.2	Global Navigation Satellite Systems	17
2.5	High-frequency models for Earth rotation variations	18
3	Ocean tides	21
3.1	Observations of the ocean surface	21
3.2	Tide generating forces	22
3.3	Astronomical arguments	26
3.4	Dynamic and equilibrium theory	29
3.5	Non-gravitational tides	31
3.6	Ocean tide models	32
3.7	Ocean tidal effects on Earth rotation	35
4	Estimation of oceanic currents from measured elevations	39
4.1	Dynamic equations	40
4.1.1	Equilibrium tide	41
4.1.2	Loading and self-attraction	43
4.2	Algorithm and numerics	44
4.3	Inversion Results	47

5	New Earth rotation corrections based on empirical ocean tide models	61
5.1	Minor tides and admittance	67
5.1.1	Admittance transferred to ocean tidal angular momentum	74
5.2	Inclusion of minor tides	77
6	Comparison and validation of high-frequency Earth rotation models	85
6.1	Parameter estimation process	85
6.2	Validation using VLBI observations	87
6.2.1	Input data	88
6.2.2	Analysis strategy	88
6.2.3	Validation results	89
6.3	Final model validation	94
7	Summary and conclusions	97
7.1	Discussion of validation results	98
7.2	Concluding remarks and outlook	99
A	Auxiliary material	101
	List of Figures	105
	List of Tables	107
	Acronyms	109
	Bibliography	111

Chapter 1

Introduction

The Earth is a complex, dynamic system, undergoing variations of its geometric properties, its gravity field, and its rotation on a wide variety of timescales. Periodical changes of the Earth's rotation occur on periods from hours to decades and longer, reflecting the diverse processes that lead to these irregularities. Mass redistribution due to tidal forces, exerted by gravitational attraction of celestial objects are the major source of changes in Earth rotation speed and direction of the rotation axis. These non-uniformities have considerable implications on observations of objects in space as well as precise navigation on Earth using space geodetic techniques, such as VLBI or Global Navigation Satellite Systems (GNSS), which are used to realize e.g. geodetic reference frames. Thus, studies of Earth rotation and the development of correction models are beneficial for global society in an era of rapid environmental changes. In addition, scientific studies and—if possible—continuous monitoring and observations extend our knowledge and understanding of the Earth as a dynamic system.

1.1 The Earth's variable rotation

Describing how the deformable Earth changes its shape and its rotation is an important task of modern geodesy and geodynamics. The rotation of the solid Earth varies—under the principle of conservation of angular momentum—due to external torques by celestial objects, mass distribution within the Earth system, and angular momentum transfer between the solid Earth and the covering fluid components, namely atmosphere and oceans. This allows the derivation of the rotation of the solid Earth by computing the change of angular momentum of the fluid parts of the Earth. Both the orientation of the rotation axis and the rotation speed change periodically and episodically over time. The description of changes requires a reference, to which the variations are referred to. The axis movement with respect to the crust is *polar motion*, that with respect to (inertial) space *precession* and *nutation*. Rotation speed changes are usually defined as excess over the nominal length of day, ΔLOD .

Due to Earth's flattening, gravitational forces from outside the equatorial plane exert a torque on the equatorial bulge. This causes the rotation axis to revolve around the ecliptic pole with a

period of about 25800 years. This precession, having an aperture of 23.5° , denotes the largest deviation from uniform rotation. It is superimposed by nutation, consisting of harmonic variations with periods between several days and 18.6 years due to periodic changes of the relative positions of Moon and Sun, respectively. The polar motion signal is dominated by an annual peak of about 3 m, mainly due to seasonal mass redistribution in the atmosphere, and the Chandler wobble (CW), a free mode of the Earth at a period of 433 days and a variable amplitude of up to 6 m. The excitation mechanism of the latter, originating from the non-alignment of the figure axis and the rotation axis, is still under debate. Besides a linear trend of 1.8 ms/cy, ΔLOD consists of variations up to several milliseconds (ms) on timescales up to decades.

The largest variations of Earth rotation occur on periods of several days to many years. However, irregularities at even higher frequencies exist and are detectable in observations. These short period variations, i.e., periods of one day and shorter, have been subject of many scientific studies and are also topic of this thesis. High-frequency polar motion and ΔLOD reach maximum total amplitudes in the order of 1 milliarcseconds (mas) and 1 ms, respectively. The main cause of high-frequency variations in Earth rotation are ocean tides induced by the gravitational potential of Moon and Sun. Tidal variations of the ocean water masses induce changes in the Earth's inertia tensor as well as angular momentum exchange with the solid Earth.

1.2 Motivation and objectives of this study

Harmonic variations of Earth rotation can be predicted by theoretical or semi-empirical models. The Earth orientation parameters (EOP), describing the transformation between an Earth-fixed and a space-fixed reference frame, play an important role when observations from Earth to space or vice-versa, are carried out. Even though prediction models have improved greatly over the last decades, continuous monitoring of the parameters is a crucial task in order to account for the irregular or not-included part of Earth orientation.

The need for most-accurate prediction models is obvious in cases where Earth orientation cannot be estimated in post-processing, such as spacecraft navigation. But also when estimating EOP in post-processing using least-squares, accurate functional and a priori models are required to derive accurate results. The a priori information is even more important when parameters are not estimated. For example, VLBI Intensive sessions usually do not have enough observations to estimate ERP in the analysis, requiring these parameters to be fixed to their a priori values.

The high-frequency Earth rotation variations require a priori modeling, even though the effect is small compared to long-term variations. However, the standard model mentioned in the IERS Conventions 2010 does not accurately explain all ocean tidal effects. Many efforts have been made to improve the conventional model by developing an empirical model based on VLBI or GNSS observations (e.g., Artz *et al.*, 2011; Gipson, 1996; Rothacher *et al.*, 2001).

These empirical models agree to the $10 \mu\text{s}$ level for polar motion and $1 \mu\text{s}$ for UT1-UTC. However, they lack of independence and consistency: Inter-technique comparisons show less

agreement than intra-technique ones, i.e., observations from VLBI and GNSS do not fully agree. In addition, empirical estimation might potentially overlay other geophysical effects. An independent ERP model can be derived from ocean tide models by calculating OTAM as has been accomplished by several authors (Brosche *et al.*, 1989; Chao *et al.*, 1996; Ray *et al.*, 1994). These models, based on hydrodynamic or assimilation ocean tide models, typically lack of accuracy when used in the analysis of space geodetic techniques.

The aim of this work is to derive a high-frequency ERP model based on empirical ocean tide models. These models are based purely on satellite altimetry observations and provide therefore a data source which is independent of observation techniques used for the operational estimation of ERP. As relative angular momentum requires the knowledge of oceanic flows, a basic hydrodynamic approach by Ray (2001) is used to derive tidal currents from measured elevations. This approach keeps the tidal heights fixed throughout the inversion process. The ultimate goal of this thesis is to provide an independent, consistent, and accurate high-frequency ERP model which can be used a priori in the analysis of space geodetic techniques.

1.3 Outline of the thesis

Following this introductory section, Chapter 2 describes the theoretical framework of Earth rotation variations. The concepts of celestial and terrestrial reference systems are presented as well as the corresponding reference frames, being the realization of the former. Subsequently, the Earth orientation parameters, required for the transformation from one frame to the other, are introduced. The reader gets an insight into modeling and observations of Earth rotation variations and their excitation mechanisms. The basic concepts of VLBI and GNSS are outlined.

Chapter 3 provides an insight into ocean tides and their impact on Earth rotation. After a brief overview of observation techniques of the ocean surface, the main tide generating force and its representation, the tidal potential, are introduced and described. In addition, the spherical harmonic expansion of the potential is explained. The subsequent sections deal with two important astronomical argument representations, followed by an overview of existing ocean tide models. The final part of this chapter describes ocean tidal effects on Earth rotation, including effective angular momentum functions.

Chapter 4 is dedicated to the approach of deriving oceanic currents from measured elevations, based on Ray (2001). The equations of motion and the continuity equation are introduced and the required correction terms are explained in proper notation. Algorithmic details, such as C-grid, numerical considerations, and preconditioning, are introduced. The results of a first test run using model HAMTIDE11a are shown and compared to a hydrodynamic solution. Several issues and “tuning” possibilities are discussed in order to find an optimal parameterization.

The findings of Chapter 4 are used in Chapter 5 to derive ERP correction models based on empirical ocean tides. Proper weighting parameters for different tidal constituents are empirically found by comparing OTAM from several ocean tide models. The theory of admittance as a

possibility to include minor tides in the ERP model, is described in this chapter as well.

Chapter 6 shows validation results using VLBI observations. The concept of least squares as parameter estimation process and the analysis software package as well as input data are described. The results are illustrated as differences of amplitude spectra and baseline length repeatabilities.

The final Chapter 7 summarizes the main findings of this thesis, draws the conclusions and gives a short outlook to future work and challenges of the presented topic.

Chapter 2

Earth rotation variations

2.1 Reference systems and Earth orientation

When describing and studying Earth rotation variations, there is a need for reference systems to which they can be referred. Since the Earth rotation axis varies with respect to an inertial system as well as to the solid Earth, there is the need for two coordinate systems: The space-fixed celestial reference system (CRS) and the Earth-fixed terrestrial reference system (TRS). Both are in principle four-dimensional, containing three geometric coordinates and a time coordinate.

Following the conventional terminology, a reference system is an ideal concept and based on mathematical and physical statements, while a reference frame is the constructed materialization of the former (Kovalevsky *et al.*, 1989). Modern reference systems are realized through coordinates of a set of points and objects determined from observations (Plag *et al.*, 2009).

Celestial reference frames

A CRS, representing an approximation to an inertial system, is based on positions of selected celestial objects. The origin is the barycenter of the solar system, the direction of the axes are defined by the equatorial plane and the ecliptic or by positions of extragalactic radio sources. The time standard is the Barycentric Coordinate Time (TCB, Soffel *et al.*, 2003; Torge & Müller, 2012).

The current conventional celestial reference frame is the International Celestial Reference Frame 2 (ICRF2, Fey *et al.*, 2009). It contains coordinates of 3414 radio sources, 295 of which are “defining” sources with high position stability and low source structure index. Those defining sources will be used for future maintenance and extensions of the ICRF2 (Fey *et al.*, 2009).

The catalog coordinates are derived from approximately 6.5 million group-delay measurements and 4540 VLBI sessions between 1979 and 2009. They are declared to have a noise floor of about 40 μas and an axis stability of about 10 μas (Fey *et al.*, 2009).

Terrestrial reference frames

The International Terrestrial Reference System (ITRS) is a geocentric reference system co-rotating with the Earth. The origin of the ITRS is the center of mass including oceans and atmosphere, the z axis agrees with the mean direction of the rotation axis between 1900 and 1905 (Torge & Müller, 2012).

The unit length is the meter, according to the International System of Units (SI), the orientation is maintained in accordance with the orientation of the Bureau International de l'Heure (BIH) Terrestrial System (BTS) at epoch 1984.0. To ensure the time evolution of the orientation, a no-net-rotation over the whole Earth with respect to horizontal motions is imposed.

A realization of the ITRS consists of Cartesian coordinates at a reference epoch of globally distributed sites and their constant velocities. The contributing space geodetic techniques are VLBI, Satellite Laser Ranging (SLR), GNSS and Doppler Orbitography Radiopositioning Integrated by Satellites (DORIS). The most recent realization of the ITRS is the ITRF2008 (Altamimi *et al.*, 2011). It is an improved solution compared to the previous realization, the ITRF2005, in terms of precision of positions and velocities. The origin and the scale are believed to be as accurate as 1 cm and 1.2 parts per billion (ppb) or 8 mm at the equator, respectively (Altamimi *et al.*, 2011).

Earth orientation parameters

The transformation between two three-dimensional coordinate systems requires three independent angles, the Euler angles, if the origins of both systems coincide. However, the procedure of transformation using Euler angles would require time-consuming matrix operations due to the large temporal variations of those angles (Torge & Müller, 2012, p. 43). Therefore, and by tradition, the transformation is split into two parts, using an intermediate reference frame, which requires a set of five angles to perform the full coordinate transformation from a terrestrial to a celestial reference frame. It is usually written as (Soffel & Langhans, 2013)

$$\mathbf{r}_{\text{cel}}(t) = \mathbf{Q}(t) \cdot \mathbf{R}(t) \cdot \mathbf{W}(t) \cdot \mathbf{r}_{\text{ter}}(t) \quad (2.1)$$

where $\mathbf{Q}(t)$, $\mathbf{R}(t)$, and $\mathbf{W}(t)$ are transformation matrices due to the motion of the celestial pole in the celestial reference system (precession-nutation), the rotation of the Earth (spin), and the motion of the pole in the intermediate system (polar motion), respectively (Petit & Luzum, 2010). The five elements required to perform the transformation as described in Equation 2.1 are called EOP. The terrestrial coordinates $\mathbf{r}_{\text{ter}}(t)$ are first transformed to an intermediate system using the relation between the three ERP and the matrices \mathbf{W} and \mathbf{R} (Sovers *et al.*, 1998),

$$\mathbf{W} = \mathbf{X}\mathbf{Y} = \begin{pmatrix} \cos p_x(t) & 0 & -\sin p_x(t) \\ 0 & 1 & 0 \\ \sin p_x(t) & 0 & \cos p_x(t) \end{pmatrix} \begin{pmatrix} 1 & 0 & 0 \\ 0 & \cos p_y(t) & \sin p_y(t) \\ 0 & -\sin p_y(t) & \cos p_y(t) \end{pmatrix} \quad (2.2)$$

$$\mathbf{R} = \begin{pmatrix} \cos H(t) & -\sin H(t) & 0 \\ \sin H(t) & \cos H(t) & 0 \\ 0 & 0 & 1 \end{pmatrix}. \quad (2.3)$$

H is the hour angle of the true equinox of date which is related to UT1, p_x and p_y are the polar motion coordinates in x and y direction, respectively. The intermediate frame is finally transformed to the celestial frame using $\mathbf{Q}(t)$. The separation of polar motion and precession-nutation, as described below, is done so that polar motion is long period in the terrestrial reference frame and precession-nutation is long period in the celestial reference frame (Gross, 2007).

In contrast to three Euler angles, five EOP are not independent. Since $\sigma_{\text{cel}} = \sigma_{\text{ter}} + \Omega$, where Ω is the mean angular velocity of the Earth and σ is the frequency of motion, retrograde motions with nearly diurnal frequency in the terrestrial system, $\sigma_{\text{ter}} \approx -\Omega$, have low frequencies in the celestial system. More precisely, Brzeziński & Capitaine (2011) show that

$$\mathbf{p}(t) = -\mathbf{n}(t)e^{-i\Omega t} \quad (2.4)$$

where $\mathbf{p}(t) = p_x(t) - ip_y(t)$, $i \equiv \sqrt{-1}$, Ωt is an approximation of Greenwich mean sidereal time (GMST), and $\mathbf{n}(t) = \delta\psi(t) \sin \varepsilon_0 + i\delta\varepsilon(t)$ where $\delta\psi$ and $\delta\varepsilon$ are corrections in longitude and obliquity to the adopted nutation model, i.e., the nutation parameters. ε_0 is the mean obliquity of the ecliptic (Gross, 2007).

There is a need for a reference pole in the intermediate system when transforming terrestrial to celestial coordinates (cf. Equation 2.1). The International Astronomical Union (IAU) defined the celestial intermediate pole (CIP) to be that reference pole (McCarthy & Petit, 2004, Chapter 5). The CIP extends the definition of the celestial ephemeris pole (CEP) by clarifying the separation of polar motion and precession-nutation due to their interchangeability (Equation 2.4; Gross, 2007). Then, polar motion is defined as motion of the CIP in the terrestrial frame at all frequencies outside the range $[-1.5, -0.5]$ cycles per sidereal day (cpsd). Motions within that range are assigned to precession-nutation, as it was the case for the CEP (Capitaine, 2000). Figure 2.1 illustrates the conventional relation between precession-nutation and polar motion in the terrestrial and celestial reference frame.

The location of the CIP, which is continuously observed by space geodetic techniques and provided by the IERS is given by the polar motion parameters $p_x(t)$ and $p_y(t)$. Similarly, the two celestial pole offsets, δX and δY , describe the variations of the celestial pole. The fifth EOP describes the variation of the Earth rotation velocity. It is provided as UT1–Universal Time Coordinated (UTC) (Petit & Luzum, 2010). The set of the three terrestrial EOP, polar motion and UT1–UTC, are usually referred to as ERP.

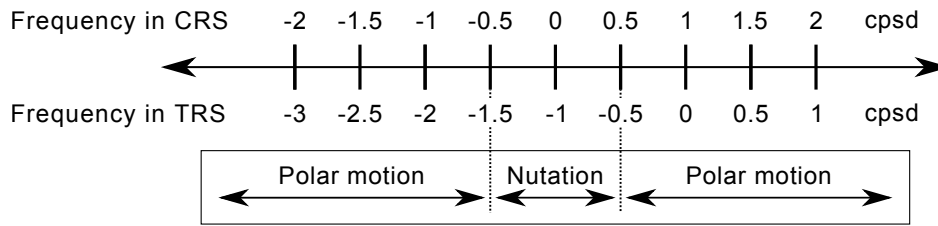


Figure 2.1: Frequency convention of the CIP. Motions of the CIP at frequencies in the range $[-0.5, 0.5]$ cpsd as viewed in the celestial reference frame (top) or—equivalently—in the range $[-1.5, -0.5]$ cpsd as viewed in the terrestrial reference frame (bottom) are considered to be precession-nutation. All other motions are considered to be polar motion. Redrawn from Dehant & Mathews (2007).

2.2 Observed and modeled Earth rotation variations

This section gives an overview of the observed signals in Earth rotation parameters as well as their excitation mechanisms. It is separated into (1) rotation speed, UT1–UTC or length-of-day (LOD), and (2) axis orientation (polar motion and precession–nutation), thus in conformity with the EOP.

The processes leading to variations in Earth rotation can be split into external gravitational forces by celestial bodies acting on the Earth, excitation by geophysical fluids like atmosphere, oceans, and hydrosphere (Gross, 2007). Geophysical processes can be subdivided into tidal motions being periodic and usually well predictable, and non-tidal effects being irregular motions due to several types of forcing, e.g., electromagnetic, gravitational, hydrodynamic or radiational (Schindelegger, 2013). Usually tidal motions have the same periods as their forcing mechanisms. However, there exist free wobbles which are only dependent on the internal structure of the Earth. Two prominent free modes are the CW and the Free Core Nutation (FCN), which are both excited by geophysical processes.

2.2.1 Earth rotation velocity

The Earth’s rotational period is the LOD. Its variations, ΔLOD , are related to changes in Universal Time and to variations in the axial component in the Earth’s spin rate (cf. Equation 2.12) by (Defraigne & Smits, 1999; Dehant & Mathews, 2007)

$$\frac{\Delta\text{LOD}(t)}{\text{LOD}} = -m_3(t) = -\frac{\partial(\text{UT1} - \text{UTC})}{\partial t} \quad (2.5)$$

where m_3 is the perturbation of a constant angular velocity of the Earth.

Figure 2.2 shows observed daily LOD variations from the combined IERS C04 time series. The Fourier spectrum (Fig. 2.2, right) was calculated using a discrete Fourier transform (FFT) and shows the one-sided amplitude spectrum for the periods between around 6 days and 19 years. A linear trend was removed from the time series before computing the FFT.

The LOD signal consists of following components: (1) A linear trend of 1.8 ms/century (cy)

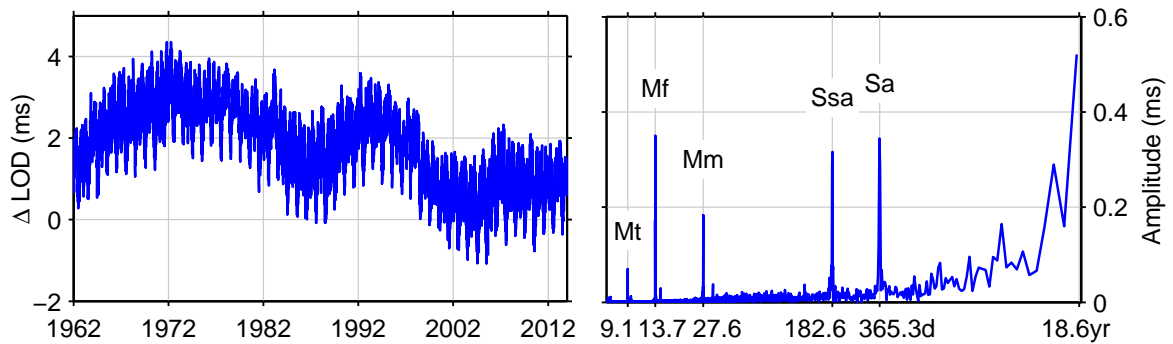


Figure 2.2: Observed LOD variations from the combined IERS C04 time series. The daily values between 1962 and December 2013 are shown on the left, the corresponding amplitude spectrum (linear trend removed) is shown on the right.

due to tidal dissipation—Lambeck (1988) states that at least 95% of the energy is dissipated in the oceans; (2) decadal variations of a few milliseconds mostly because of core-mantle coupling (Ponsar *et al.*, 2003); (3) tidal variations of around 1 ms due to solid Earth, atmospheric and oceanic tides; (4) seasonal variations of about 0.5 ms due to atmospheric and oceanic tides; and (5) smaller variations on other timescales (Gross, 2007; Rummel *et al.*, 2009).

Periods labeled with an M, (termonthly Mt, 9.1 days; fortnightly Mf, 13.7 days and monthly Mm, 27.6 days) denote tidal frequencies originating from lunar attraction. The semi-annual solar contribution at 6 months (Ssa) and the annual cycle (Sa) are solar constituents dominated by thermal effects (Wunsch *et al.*, 1997). The 18.61 years cycle originates from the period of the lunar declination (Doodson & Warburg, 1941, Chapter 5).

Both for the seasonal and intraseasonal variations, atmospheric winds are the most dominant excitation mechanisms for LOD. For the case of components between four days and one year, about 85% of the observed variance is explained by angular momentum changes of zonal winds. The influences of atmospheric surface pressure due to mass distributions, oceanic currents and oceanic bottom pressure explain each 2–4% of the observed variance. Similar figures are found for the interannual variations between one and five years, where, however, the influence of the ocean is even smaller (Gross *et al.*, 2004).

Due to the daily resolution of the IERS C04 LOD time series, periods < 2 days cannot be seen in the Fourier spectrum (Fig. 2.2, right). However, there are albeit small daily and sub-daily UT1 variations which can be observed by space geodetic techniques. Chao *et al.* (1996) show that as much as 90% of those diurnal and sub-diurnal UT1 variations can be explained by OTAM.

2.2.2 Orientation of the Earth rotation axis

Figure 2.3 shows observed polar motion variations from 1962 through 2013. The spectrum shows that the signal is dominated by a yearly signal of about 80–100 mas and the CW, a free response to equatorial torques, with a period of around 433 days and an amplitude of about 140 mas (Gross, 2000). Furthermore there exists a long term libration of the rotation pole known

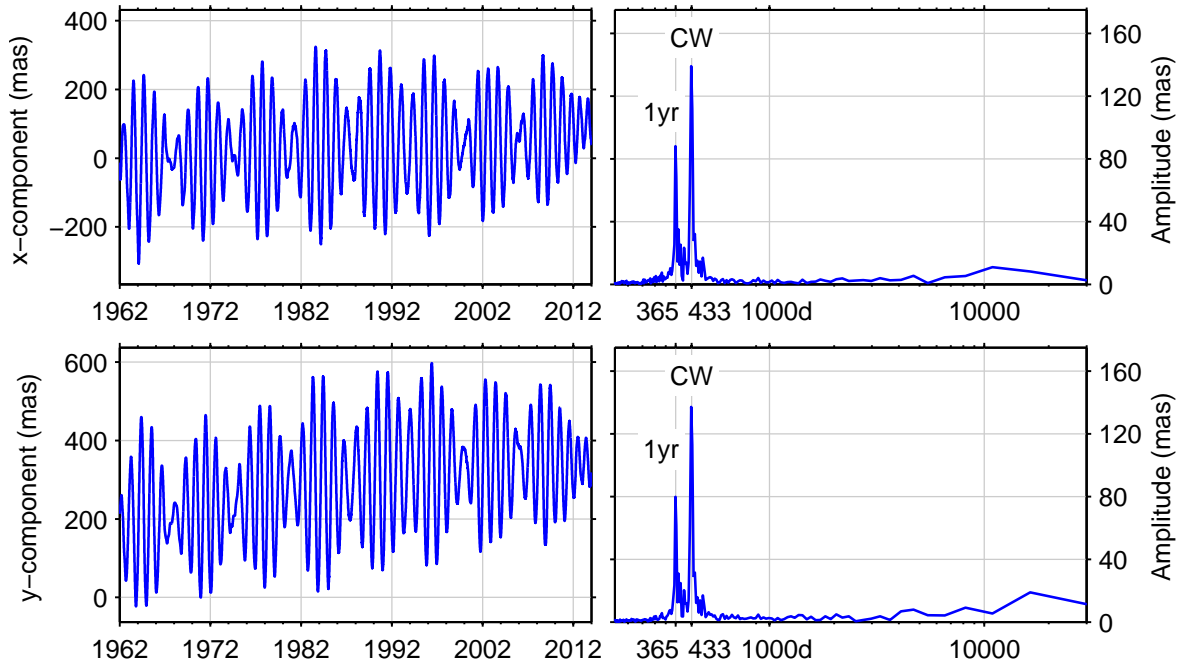


Figure 2.3: Observed polar motion variations from the combined IERS C04 time series. The daily values between 1962 and December 2013 are shown on the left, the corresponding amplitude spectrum (linear trend removed) with the one year and Chandler wobble period is shown on the right.

as the Markowitz wobble at a period of 31 years with an amplitude of about 20 mas (Poma, 2000; Vondrák, 1999). A linear trend of about 3.5 mas/year and smaller amplitudes at all measurable timescales are observed as well (Gross, 2007).

The annual oscillation in the x and y component of polar motion is a forced wobble driven by seasonal mass redistribution of atmosphere, oceans and hydrology (Lambeck, 1980). Leonhard Euler discovered that a rotating body whose principal axis of inertia is not aligned with the rotation axis will perform a free nutation, i.e., the rotation axis rotates around the figure axis. This Eulerian free wobble of the Earth is called the CW (Lambeck, 1980). Since any free oscillation in physics will undergo a damping effect, excitation mechanisms need to drive the CW. Several authors show that the CW is excited mostly by atmosphere and oceans, especially ocean-bottom pressure fluctuations (e.g., Brzeziński & Nastula, 2002; Gross, 2000; Liao *et al.*, 2003).

Since polar motion is a circular and thus two-dimensional motion, it is useful to separate it into motions of positive (prograde, in direction of the Earth's rotation) and negative frequency (retrograde) components (Eubanks, 1993). Prograde and retrograde amplitudes and phases are defined by (Gross, 2007)

$$\mathbf{p}(t) = p_x(t) - ip_y(t) = A_p e^{i\alpha_p} e^{i\sigma(t-t_0)} + A_r e^{i\alpha_r} e^{-i\sigma(t-t_0)} \quad (2.6)$$

where p and r indicate prograde and retrograde amplitudes and phases, respectively. σ is the positive frequency and t_0 is the reference epoch. Since the Earth rotates daily prograde, luni-

solar tides have an apparent retrograde motion and thus their frequencies are negative (Dickman, 1993).

2.3 Geophysical excitation of Earth rotation

The derivation of rigid-body dynamics can be found in literature, such as Moritz & Mueller (1987) or Lambeck (1980). The quintessence is that the response of an applied torque \mathbf{L} is equal to the change of angular momentum $\frac{\partial}{\partial t}\mathbf{H}$. Since the Earth is a more complex and dynamic system, deformations of the Earth have to be taken into account. Furthermore, gravitational forces of the Sun, the Moon and planets cause changes of the rotational behavior of the Earth.

Euler's second law, in an Earth-fixed reference frame, is written as (Gross, 2007; Munk & MacDonald, 1960)

$$\mathbf{L}(t) = \frac{\partial \mathbf{H}(t)}{\partial t} + \boldsymbol{\omega}(t) \times \mathbf{H}(t), \quad (2.7)$$

where $\mathbf{L}(t)$ are external torques, $\mathbf{H}(t)$ is angular momentum and $\boldsymbol{\omega}(t)$ is the angular velocity of the Earth with respect to an inertial reference frame.

The angular momentum can be split into two parts: (1) Relative angular momentum $\mathbf{h}(t)$ due to relative motion of particles and (2) changes of the inertia tensor $\mathbf{I}(t)$ (Munk & MacDonald, 1960):

$$\mathbf{H}(t) = \mathbf{h}(t) + \mathbf{I}(t) \cdot \boldsymbol{\omega}(t) \quad (2.8)$$

Substituting Equation (2.8) into Equation (2.7) gives the Liouville equation in an Earth-fixed reference frame:

$$\mathbf{L}(t) = \frac{\partial}{\partial t} [\mathbf{h}(t) + \mathbf{I}(t) \cdot \boldsymbol{\omega}(t)] + \boldsymbol{\omega}(t) \times [\mathbf{h}(t) + \mathbf{I}(t) \cdot \boldsymbol{\omega}(t)] \quad (2.9)$$

The body-fixed axes are defined so that the relative angular momentum due to motion of the crust and mantle vanishes. This frame is called Tisserand mean-mantle frame. If this definition is used, the relative motions of the core, the atmosphere and the ocean have a relative angular momentum, those of the crust and mantle do not (Gross, 2007).

The deviations from uniform rotation of the Earth are small: Velocity changes are of the order of 10^{-8} (a few milliseconds in LOD), polar motion changes of the order of 10^{-6} (several hundred milliarcseconds). Thus, the Liouville equation (2.9) can be linearized with initially uniform rotation. Then, angular velocity and inertia tensor of the Earth can be written as

$$\boldsymbol{\omega}_0 = \begin{pmatrix} 0 \\ 0 \\ \Omega \end{pmatrix} \quad (2.10)$$

$$\mathbf{I}_0 = \begin{pmatrix} A & 0 & 0 \\ 0 & B & 0 \\ 0 & 0 & C \end{pmatrix}, \quad (2.11)$$

where A , B and C are the mean principal moments of inertia ($A < B < C$). Dynamically the Earth is nearly axisymmetric: $(B - A)/A = 2.2 \cdot 10^{-5} \ll 1$ (Gross, 2007). This allows averaging of the equatorial principal moments of inertia A and B and replacing them by the mean value $A' = (A + B)/2$.

Then, introducing mass displacements and relative angular momentum, the time-dependent angular velocity and inertia tensor can be written as

$$\boldsymbol{\omega}(t) = \boldsymbol{\omega}_0 + \begin{pmatrix} m_1(t) \\ m_2(t) \\ m_3(t) \end{pmatrix} \Omega \quad (2.12)$$

$$\mathbf{I}(t) = \mathbf{I}_0 + \Delta\mathbf{I}(t) \quad (2.13)$$

By substituting Equations (2.13) and (2.12) into Equation (2.9) and neglecting products and squares of small quantities, we obtain the Euler-Liouville equations:

$$\begin{aligned} \frac{\dot{m}_1(t)}{\sigma_r} + m_2(t) &= \psi_2 + \frac{L_1(t)}{\Omega^2(C - A)} \\ \frac{\dot{m}_2(t)}{\sigma_r} - m_1(t) &= \psi_1 + \frac{L_2(t)}{\Omega^2(C - A)} \\ \dot{m}_3(t) &= \dot{\psi}_3 + \frac{L_3(t)}{\Omega C} \end{aligned} \quad (2.14)$$

with the Euler frequency

$$\sigma_r = \left(\frac{C - A'}{A'} \right) \Omega \quad (2.15)$$

and the excitation functions ψ_i (Munk & MacDonald, 1960)

$$\begin{aligned} \psi_1 &= \frac{\Omega h_1 + \dot{h}_2 + \Omega^2 \Delta I_{13} + \Omega \Delta \dot{I}_{23}}{\Omega^2(C - A')} \\ \psi_2 &= \frac{\Omega h_2 - \dot{h}_1 + \Omega^2 \Delta I_{23} - \Omega \Delta \dot{I}_{13}}{\Omega^2(C - A')} \\ \psi_3 &= \frac{-h_3 - \Omega \Delta I_{33}}{\Omega C} \end{aligned} \quad (2.16)$$

If external torques are set to zero, the last term of the Euler-Liouville equations vanishes. The right-hand side of Equations (2.14) consists of relative angular momentum components $\mathbf{h}(t)$ and

inertia tensor components ΔI as well as their time derivatives. If those values are known from observations or models, Equation (2.14) can be solved for $\mathbf{m}(t)$ and $\boldsymbol{\omega}(t)$ can be derived.

The two equatorial components are coupled differential equations and it is therefore convenient to use complex notation as follows (Schindelegger *et al.*, 2013)

$$\begin{aligned} \hat{m} &= m_1 + im_2 \\ \hat{h} &= h_1 + ih_2 \\ \Delta \hat{I} &= \Delta I_{13} + i\Delta I_{23} \\ \hat{\psi} &= \psi_1 + i\psi_2 \end{aligned} \tag{2.17}$$

Without excitation, the solution of the equatorial component of Equation (2.14) is

$$\hat{m} = \hat{m}_0 e^{i\sigma_r t}, \tag{2.18}$$

which is a prograde, undamped circular motion of frequency σ_r , corresponding to the Euler period of $2\pi/\sigma_r = 304.46$ sidereal days (Gross, 2007).

Allowing excitation, the solutions of the Euler-Liouville equations for equatorial and axial components are

$$\begin{aligned} \hat{m} &= e^{i\sigma_r t} \left(\hat{m}_0 - i\sigma_r \int_0^t \hat{\psi}(\tau) e^{-i\sigma_r \tau} d\tau \right) \\ m_3 &= \psi_3 + \text{const} \end{aligned} \tag{2.19}$$

It can be seen that in the linearized Euler-Liouville equations, the variation of the direction of the rotation pole (m_1 and m_2) and the variation of the rotation velocity (m_3) can be completely separated (Eubanks, 1993; Moritz & Mueller, 1987).

Due to the existence of atmosphere and oceans and a fluid core, as well as a deformable crust and mantle, the Earth cannot be regarded as rigid. However, if Tisserand mean-mantle frame axes are used, there are no relative angular momentum changes of the crust and mantle. Besides if the ocean is assumed to be in equilibrium, there are no changes of relative angular momentum due to oceanic currents. If, furthermore, the relatively small effect of the atmosphere is neglected, only the core contributes to relative angular momentum changes due to changes in rotation (Gross, 2007).

Smith & Dahlen (1981) show that for a both dynamically and geometrically axisymmetric Earth, the induced relative angular momentum changes due to core motion caused by a spin of the mantle at frequencies $\sigma \ll \Omega$ is

$$\begin{pmatrix} \Delta h_1 \\ \Delta h_2 \\ \Delta h_3 \end{pmatrix} = \begin{pmatrix} E & iE' & 0 \\ -iE' & E & 0 \\ 0 & 0 & \tilde{E} \end{pmatrix} \begin{pmatrix} m_1(\sigma) \\ m_2(\sigma) \\ m_3(\sigma) \end{pmatrix} \tag{2.20}$$

where

$$E = \frac{\sigma^2}{\Omega} A_C \quad (2.21)$$

$$E' = -\sigma(1 - \varepsilon_C) A_C \quad (2.22)$$

$$\ddot{E} = -\Omega C_C \quad (2.23)$$

to first order in the core-mantle boundary ellipticity ε_C . A_C and C_C are the equatorial and axial principal moments of inertia of the core (Gross, 2007). The third linear equation in (2.20) shows that the Earth's core is decoupled in the axial component from the rotation of the mantle and can therefore not follow changes in the rotation rate of the mantle (Wahr *et al.*, 1981).

Changes in the Earth's rotation also affect the Earth's inertia tensor I . If there were no oceans and under the assumption that the response of the Earth to centripetal potential due to rotation changes is analogous to the nonrotating (Earth) and static (potential) case, the changes in the Earth's inertia tensor are

$$\begin{pmatrix} \Delta I_{13} \\ \Delta I_{23} \\ \Delta I_{33} \end{pmatrix} = \frac{a^5 \Omega^2}{3G} \begin{pmatrix} k_2 & 0 & 0 \\ 0 & k_2 & 0 \\ 0 & 0 & n_0 + \frac{4}{3} k_2 \end{pmatrix} \begin{pmatrix} m_1 \\ m_2 \\ m_3 \end{pmatrix} \quad (2.24)$$

where a is the mean radius of the Earth, G is the gravitational constant, k_2 is the second-degree body tide Love number of the whole Earth (Dahlen, 1976; Gross, 2007) or of the mantle (Dickman, 2005). The change in the Earth's mean moment of inertia due to purely radial deformations is accounted for by n_0 .

Adding equilibrium oceans to the system, Equation (2.24) is modified to

$$\begin{pmatrix} \Delta I_{13} \\ \Delta I_{23} \\ \Delta I_{33} \end{pmatrix} = \begin{pmatrix} D + \Delta D & \Delta D_{12} & \Delta D_{13} \\ \Delta D_{12} & D - \Delta D & \Delta D_{23} \\ \Delta D_{13} & \Delta D_{23} & \ddot{D} \end{pmatrix} \begin{pmatrix} m_1 \\ m_2 \\ m_3 \end{pmatrix} \quad (2.25)$$

where

$$D = (k_2 + \Delta k_{ocn,w}) \frac{a^5 \Omega^2}{3G} \quad (2.26)$$

and

$$\ddot{D} = \left[n_0 + \frac{4}{3} (k_2 + \Delta k_{ocn,s}) \right] \frac{a^5 \Omega^2}{3G}. \quad (2.27)$$

The ‘‘oceanic Love number’’ Δk_{ocn} accounts for the equilibrium oceans by modifying the Love

number k_2 .

When the effects described in Equations (2.20) and (2.25) are applied in the Liouville equations, they become

$$\hat{m} + \frac{i\dot{\hat{m}}}{\sigma_{cw}} = \hat{\chi} - \frac{i\dot{\hat{\chi}}}{\Omega} \quad (2.28)$$

$$\frac{\dot{m}_3}{\Omega} = -\frac{\dot{\chi}_3}{\Omega} \quad (2.29)$$

where σ_{cw} , the theoretical CW frequency, is

$$\sigma_{cw} = \left(\frac{C - A' - D}{A'_m + \varepsilon_C A_C + D} \right) \Omega. \quad (2.30)$$

$A'_m = A' - A_C$ denotes the equatorial principal moment of inertia of crust and mantle. The excitation functions χ_i are written as

$$\hat{\chi} = \frac{\hat{h} + \Omega(1 + k'_2) \Delta \hat{I}}{\Omega(C - A' - D)} \quad (2.31)$$

and

$$\chi_3 = k_r \frac{h_3 + \Omega(1 + \alpha_3 k'_2) \Delta I_{33}}{\Omega C_m}. \quad (2.32)$$

The parameter

$$k_r = \left\{ 1 + \left[n_0 + \frac{4}{3} (k_2 + \Delta k_{ocn,s}) \right] \frac{a^5 \Omega^2}{3G} \frac{1}{C_m} \right\}^{-1} \quad (2.33)$$

accounts for rotational deformations on the axial component. Solid Earth loading is accounted for by the use of the second-degree load Love number k'_2 , the factor α_3 modifies k'_2 due to coupling of the core to the mantle (Dickman, 2003; Gross, 2007).

The equations above describe the response to small excitations in Earth rotation variations for an elastic Earth with a fluid core and oceans in equilibrium. If numerical values for the constants as well as the observed period of the CW $T_{cw} = 434.2$ sidereal days for the theoretical period are used, the excitation functions can be rewritten (Gross, 2007):

$$\hat{\chi} = \frac{1.608\hat{h} + 1.100\Omega\Delta\hat{I}}{\Omega(C - A')} \quad (2.34)$$

$$\chi_3 = \frac{0.997h_3 + 0.748\Omega\Delta I_{33}}{\Omega C_m} \quad (2.35)$$

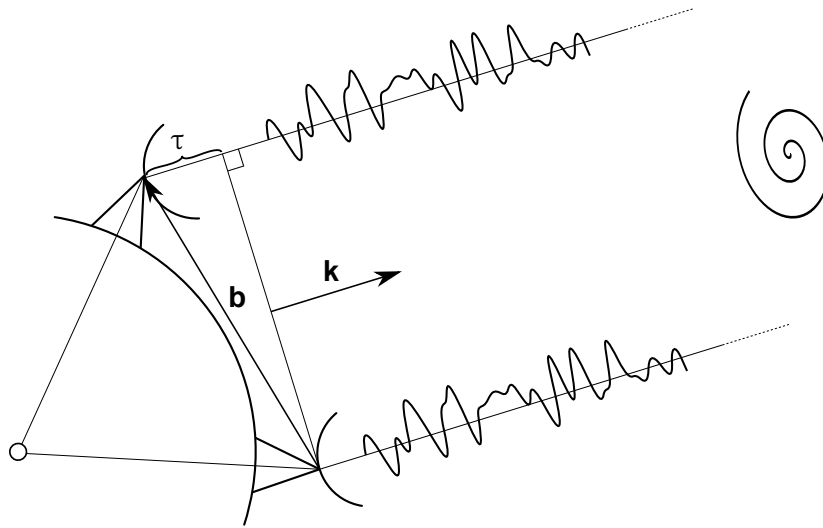


Figure 2.4: Geometric principle of VLBI where the signal emitted by an extragalactic radio source is recorded at two sites at the Earth's surface using VLBI telescopes.

Wahr (2005) gives the following values for the coefficients in Equation (2.34) including mantle anelasticity: $1.61 - 0.02i$ for \hat{h} and $1.10 - 0.01i$ for $\Omega\Delta\hat{I}$.

2.4 Observations of Earth rotation variations

Prior to the appearance of space geodetic techniques, Earth rotation measurements were carried out using lunar occultations of stars by the Moon or star transits using optical measurements. The terrestrial pole was observed by measuring changes in the apparent latitudes of stations (Gross, 2007). Nowadays, VLBI, GNSS, and SLR and Lunar Laser Ranging (LLR) are the most accurate observation techniques to monitor changes in Earth orientation (Rummel *et al.*, 2009).

2.4.1 Very Long Baseline Interferometry

VLBI measures the difference in arrival time of a radio signal from the same extragalactic radio source at two or more stations on the Earth. Figure 2.4 shows the basic geometric principle of a single-baseline VLBI observation. Because of the far distance of the sources, the radio waves arrive as planar wavefronts. Hence, the baseline vector \mathbf{b} between the two stations, the unit vector \mathbf{k} pointing to the radio source and the time delay τ form the basic VLBI equation (Schuh & Böhm, 2013)

$$\tau = -\frac{\mathbf{b} \cdot \mathbf{k}}{c} \quad (2.36)$$

where c is the velocity of light. Atomic clocks at the stations add a precise time-stamp to the recorded signal, allowing the derivation of the time delay by cross-correlating the signals in post-processing.

VLBI signals are recorded at two frequencies—2.3 GHz (S-Band) and 8.4 GHz (X-Band)—to enable first-order corrections for the effect of the ionosphere (Gross, 2007; Sovers *et al.*, 1998). The future VLBI2010 Global Observing System (VGOS) is designed to observe at a broader frequency band between 1 and 14 GHz to avoid Radio Frequency Interference (RFI) and to significantly improve the measurement precision (Niell *et al.*, 2006). VLBI is “sensitive to (all) processes that change the relative position of the radio telescopes with respect to the source” (Gross, 2007), such as Earth orientation, station and source positions, or tropospheric parameters.

The parameter estimation process, usually a least squares adjustment, minimizes the weighted sum of the squared residuals. Details on the least squares method can be found in Chapter 6. The theoretical delay is calculated from a delay model which requires some prior information about the parameters. Sovers *et al.* (1998) divide the delay model into three categories: (1) Geometric delay being by far the largest component and including effects such as station positions and displacements due to tectonic motions or tidal effects, Earth orientation, or source parameters; (2) atmospheric delay, describing the behavior of the signal if not in vacuum and (3) instrumental delay.

Due to the essentially fixed radio sources, VLBI is uniquely able to provide unambiguous and stable ties between the terrestrial and celestial reference frame (Blewitt, 2007). It is the only technique that allows the estimation of all five EOP (Schuh & Böhm, 2013). All other techniques can derive only a subset or a linear combination of the EOP or their time derivatives (Gross, 2007; Rummel *et al.*, 2009), making VLBI the premier measurement technique for determining the International Celestial Reference Frame (ICRF), precession-nutation and UT1–UTC (Eubanks, 1993).

2.4.2 Global Navigation Satellite Systems

Global satellite systems emitting microwaves for the purpose of positioning, timing, and navigation are summarized as GNSS. The three major GNSS are the GPS of the United States, the Russian Globalnaja Nawigazionnaja Sputnikowaja Sistema (GLONASS) and the European Galileo system (Hofmann-Wellenhof *et al.*, 2008). The satellites at altitudes of around 20000 km transmit modulated signals at two carrier frequencies in the L-Band (for the case of GPS: L1 = 1575.42 MHz and L2 = 1227.60 MHz), allowing to measure the distance to at least four satellites from a terrestrial receiver and thus to estimate the receiver’s position.

Least squares adjustment and Kalman filter algorithms are typical tools for the post-processing analysis of GNSS observations. Several instrumental corrections—both satellite- and receiver-related—have to be applied and atmospheric propagation effects have to be considered. Other effects, such as the number of full phase cycles, are estimated together with station positions, satellite orbits and EOP. In order to estimate precisely the unknown parameters, a priori models are required and processing strategies, such as building linear combinations or differences in order to eliminate parameters, are applied (Steigenberger, 2009).

Due to the possibility of continuous measurements, the large number of observations, and

the dense ground network, GNSS plays a decisive role in the realization of the ITRS and in monitoring the atmosphere and the Earth rotation parameters (Angermann *et al.*, 2013; Blewitt, 2007; Dick & Thaller, 2014). The GNSS solution of polar motion shows a roughly five times smaller precision than the one from VLBI when comparing them to the IERS combined solution (Dick & Thaller, 2014). But one has to bear in mind the much larger weight of GNSS in those combined time series. The accuracy of polar motion estimates are given as $30 \mu\text{s}$ (IGS, 2013), VLBI-derived polar motion estimates can be as accurate as $50\text{--}80 \mu\text{s}$ (Schuh & Böhm, 2013).

However, only polar motion and its time derivative can be determined independently from GNSS. UT1 cannot be separated from the satellite orbit since it is correlated with the right ascension of the ascending node of the satellite and also nutation cannot be determined solely from GNSS (Gross, 2007; Steigenberger, 2009). Although nutation and UT1 cannot be derived in an absolute sense, their time derivatives—being related to orbital elements—can be determined using satellite techniques (Rothacher *et al.*, 1999). Hence, GNSS provides the rates of UT1, i.e., LOD for the combined C04 EOP time series of the IERS (Dick & Thaller, 2014). However, it should be pointed out that mismodeling in GNSS analysis, e.g., mismodeling of the radiation pressure, may lead to biases in the polar motion estimates which could not be seen in a GNSS-only validation (Rothacher *et al.*, 2001; Springer *et al.*, 1999).

2.5 High-frequency models for Earth rotation variations

A priori ERP models are required to reduce the observables of space geodetic techniques in order to accurately estimate geodetic or geophysical parameters in the analysis (Sovers *et al.*, 1998; Steigenberger, 2009). The accuracy of these models is even more important in cases where parameters are not estimated but fixed to their a priori values. This is required for example in VLBI Intensive sessions. Those one-hourly, single-baseline VLBI experiments, providing near real-time estimates of UT1–UTC, contain about 20–30 observations (Haas *et al.*, 2010) and—due to low number of observations and poor network geometry—do not allow the estimation of ERP.

However, the current standard—the IERS Conventions 2010 model—is not accurate enough to fulfill the future Global Geodetic Observing System (GGOS) requirements, as described in Plag *et al.* (2009) (Artz, 2011).

One approach to derive an a priori high-frequency ERP model is to use observations from space geodetic techniques and fitting the tidal amplitudes to the residuals. Such empirical models have been derived from VLBI (e.g., by Artz *et al.*, 2011; Gipson, 1996; Herring & Dong, 1994), GPS (e.g., by Rothacher *et al.*, 2001), and SLR (e.g., by Watkins & Eanes, 1993) observations. A GPS-VLBI combined empirical model has been derived by Artz *et al.* (2012). Recent empirical models agree to a level of $7.5 \mu\text{s}$ in polar motion and $0.5 \mu\text{s}$ in UT1 for most tidal constituents (Artz *et al.*, 2011). However, empirical models bear the danger of simply covering signals in the (sub-)diurnal band. Additionally, they do not allow the study and separation of different geophysical effects.

High-frequency ERP models can also be derived from ocean tide models as ocean tides cause the most important excitations at those periods (Nilsson *et al.*, 2010; Ray *et al.*, 1994). ERP models based on ocean tides provide a more independent source, making them preferable to empirical models. The standard model recommended by the IERS Conventions 2010 is one example of this model type. Several other authors have developed other ERP models based on ocean tides, e.g., Chao & Ray (1997), Dickman (1993), or Gross (1993).

Chapter 3

Ocean tides

3.1 Observations of the ocean surface

Most of the recent ocean tide models comprise observations of the ocean surface, such as the series of FES models (Le Provost *et al.*, 1998). There exist purely hydrodynamic models mainly being driven by gravitational forces, e.g., by Seiler (1991) or a newer model by Müller *et al.* (2012). Those models, however, are less accurate than observation-based models (Stammer *et al.*, 2014, p. 266) and thus not suitable for the derivation of accurate ERP prediction values.

Sea surface observations using direct measurements have a long history, especially at coastal regions (Pugh & Woodworth, 2014). However, even when offshore measurements are included, the spatial distribution over the oceans is sparse. Global observations became only available after the first operational satellite altimetry missions. ERS-1, launched in 1991 and operated by the European Space Agency (ESA), was the first operational satellite with a radar altimetry device on board. In 1992, the TOPEX/Poseidon mission started as an US and French cooperation. It was dedicated to sea surface measurements with an accuracy of less than 5 cm. Since then, several satellite missions were launched and the technique of satellite altimetry improved greatly. Today, more than two decades of observations are available allowing the derivations of models which mutually agree better than 1 cm in the open ocean (Stammer *et al.*, 2014).

The global coverage, the time-span of observations, and improved correction models and calibration of satellite altimetry allow a pure empirical estimation of ocean tides (Mayer-Gürr *et al.*, 2012; Ray, 1999). Empirical models have shown to perform similar to hydrodynamic assimilation models (Ray *et al.*, 2011). However, the coverage of satellite altimetry is not exactly global as there are no observations at higher latitudes than the satellite orbit's inclination. The inclination of the TOPEX/Poseidon and Jason missions is 66° .

Altimetry devices on satellites typically emit radar pulses in two frequency bands, e.g., in C-band (5.3 GHz) and Ku-band (13.6 GHz) for the TOPEX/Poseidon and Jason missions. Measurements of the altimeter range, i.e., the distance between the satellite and the ocean surface, are usually averaged over one second. If the height of the satellite is known, the sea surface height (SSH) can be obtained. The mean height of the satellites is between 700 and 1400 km, which is

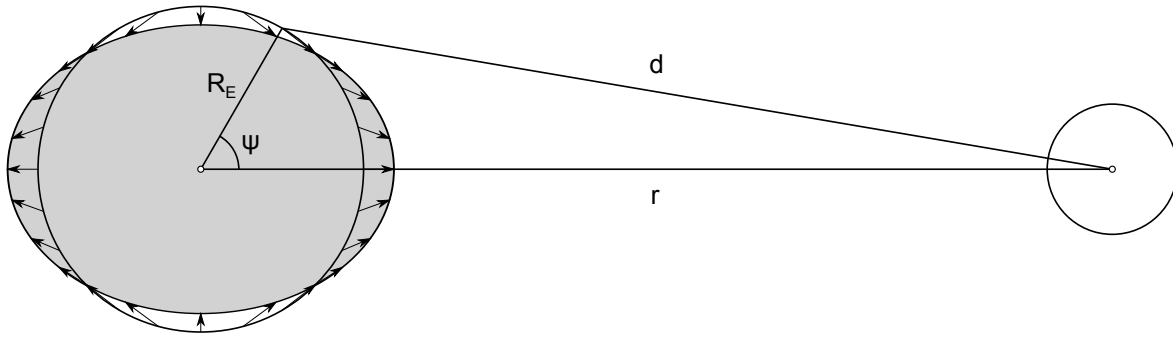


Figure 3.1: Illustration of the tidal force acting on a point on the Earth surface due to a celestial body.

a compromise between several factors, such as atmospheric drag, influence of the gravity field, power requirements, and exposure to radiation (Pugh & Woodworth, 2014). A short repeat period (9.9 days for TOPEX/Poseidon and Jason; 35 days for the ESA missions) is at the expense of a good spatial resolution: The track separation of TOPEX/Poseidon and Jason is 316 km whereas for the ESA missions it decreases to 80 km.

The altimeter range has to be corrected for atmospheric delays and geophysical effects as well as instrumental biases. Another offset between the apparent and the real ocean surface is the sea state bias (SSB). It consists of (1) the electromagnetic bias, stemming from the fact that backscatter is larger from troughs than from crests of a wave inside the footprint and, thus, making the range too long; and (2) the skewness bias, being the difference between the mean and the median scattering surface. The skewness bias is primarily dependent on the significant wave height (SWH). After applying all corrections, the SSH can be averaged to define a mean sea level (Pugh & Woodworth, 2014).

3.2 Tide generating forces

Tides are periodic motions of the solid or fluid parts of the Earth due to inhomogeneous potential fields across the Earth arising from celestial bodies. These forces as well as induced tidal deformations and incremental centrifugal forces are the major contributors of periodic changes of Earth rotation.

After Newton's law of gravitation, the acceleration acting on a point caused by a celestial body is

$$\mathbf{a}_p = \frac{GM_{\text{cel}}}{d^2} \frac{\mathbf{r}_{\text{cel}} - \mathbf{r}_p}{d} \quad (3.1)$$

where G is the gravitational constant, M_{cel} is the mass of the celestial body, \mathbf{r}_{cel} and \mathbf{r}_p are the position vectors of the center of mass of the celestial body and the point, respectively, and $d = |\mathbf{r}_{\text{cel}} - \mathbf{r}_p|$ is the distance between those points. The difference illustrates the notion of the tidal force being a differential one (Agnew, 2007).

Instead of the gravitational force field (vector field), the gravitational potential field (scalar field) is commonly used to represent the gravitational effect of the celestial bodies. The gravitational force on a unit mass element is given by the gradient of the gravitational potential, $f_g = -\nabla V_g$. For a point on the Earth's surface it can be written as (Agnew, 2007)

$$V_g = \frac{GM_{\text{cel}}}{d} = \frac{GM_{\text{cel}}}{r} \left(1 + \frac{R_E^2}{r^2} - 2 \frac{R_E}{r} \cos \psi \right)^{-\frac{1}{2}}, \quad (3.2)$$

where R_E is the radius of the Earth, r is the distance from the Earth center to the center of mass of the celestial body and ψ is the geocentric angle between the point on the Earth's surface and the center of mass of the celestial body.

The brackets term in Equation (3.2), i.e., the reciprocal distance, can be expanded into a series of Legendre polynomials (Pugh & Woodworth, 2014):

$$\begin{aligned} V_g &= \frac{GM_{\text{cel}}}{r} \left(1 + \frac{R_E}{r} P_1(\cos \psi) + \frac{R_E^2}{r^2} P_2(\cos \psi) + \frac{R_E^3}{r^3} P_3(\cos \psi) + \dots \right) = \\ &= \frac{GM_{\text{cel}}}{r} \sum_{n=0}^{\infty} \left(\frac{R_E}{r} \right)^n P_n(\cos \psi), \end{aligned} \quad (3.3)$$

where $P_n(\cos \psi)$ are Legendre polynomials. The first term (degree $n = 0$) in Equation (3.3) is constant except for variations in r , and thus produces no force. The second term ($n = 1$) produces a constant force along the orbital direction which must be subtracted to get the tidal force, and, hence, the time-dependent tidal potential can be written as (Agnew, 2007)

$$V_{\text{tid}}(t) = \frac{GM_{\text{cel}}}{r(t)} \sum_{n=2}^{\infty} \left(\frac{R_E}{r(t)} \right)^n P_n(\cos \psi). \quad (3.4)$$

The degree-two term ($n = 2$) in Equation (3.4) is the main tide-producing term, containing about 98% of the total tidal potential (Torge & Müller, 2012).

Normalizing the tidal potential, i.e., setting the value of the Moon to 1, the effect of the Sun is 0.46, that of Venus $5 \cdot 10^{-5}$ and that of Jupiter $6 \cdot 10^{-6}$. Hence, the "lunisolar" tides have by far the biggest effect and are probably the only ones measurable (Agnew, 2007). Since $\frac{R_E}{r} \approx \frac{1}{60}$ for the Moon, the sum in Equation (3.4) decreases rapidly. This allows to neglect terms $n \geq 4$ for most purposes (Pugh & Woodworth, 2014).

The geocentric angle ψ can be expressed by Earth-fixed coordinates using spherical coordinates of the point (latitude φ , longitude λ) and the celestial body (φ' , λ') so that (Moritz & Mueller, 1987)

$$\cos \psi = \sin \varphi \sin \varphi' + \cos \varphi \cos \varphi' \cos(\lambda - \lambda') \quad (3.5)$$

and the spherical harmonic expansion of the tidal potential can be written as

$$V_{\text{tid}}(t) = \frac{GM_{\text{cel}}}{r(t)} \sum_{n=2}^{\infty} \left[\left(\frac{R_E}{r(t)} \right)^n \sum_{m=0}^n \left((2 - \delta_{0m}) \frac{(n-m)!}{(n+m)!} P_{nm}(\sin \varphi) P_{nm}(\sin \varphi') \cos m(\lambda - \lambda') \right) \right] \quad (3.6)$$

where $\delta_{0m} = 1$ if $m = 0$, otherwise 0, and P_{nm} are unnormalized associated Legendre functions which are defined by (Lambeck, 1980; Teschl, 2014)

$$P_{nm}(x) = (-1)^m (1-x^2)^{m/2} \frac{d^m}{dx^m} P_n(x) \quad (3.7)$$

where

$$P_n(x) = \frac{1}{2^n n!} \frac{d^n}{dx^n} (x^2 - 1)^n. \quad (3.8)$$

are Legendre polynomials of degree n . Up to $n = 3$ they are given explicitly by

$$P_{00} = 1 \quad (3.9)$$

$$P_{10} = \sin \varphi \quad P_{11} = \cos \varphi \quad (3.10)$$

$$P_{20} = \frac{3}{2} \sin^2 \varphi - \frac{1}{2} \quad P_{21} = 3 \cos \varphi \sin \varphi \quad P_{22} = 3 \cos^2 \varphi \quad (3.11)$$

$$P_{30} = \frac{5}{2} \sin^3 \varphi - \frac{3}{2} \sin \varphi \quad P_{31} = \cos \varphi \left(\frac{15}{2} \sin^2 \varphi - \frac{3}{2} \right) \quad P_{32} = 15 \cos^2 \varphi \sin \varphi \quad P_{33} = 15 \cos^3 \varphi \quad (3.12)$$

The terms

$$\begin{aligned} C_{nm}(\varphi, \lambda) &= P_{nm}(\sin \varphi) \cos(m\lambda) \\ S_{nm}(\varphi, \lambda) &= P_{nm}(\sin \varphi) \sin(m\lambda) \end{aligned} \quad (3.13)$$

are spherical harmonics. Those functions are defined on a sphere and used to represent or approximate spherical functions. Similar to Fourier series in one dimension, any two-dimensional, quadratically integrable function on a sphere can be expanded into a series of spherical harmonics. The spherical harmonic representation of scalar potentials is a common application of spherical harmonics in geosciences (Freedon & Schreiner, 2009).

An illustration of spherical harmonics of degree $n = 2$ to $n = 4$ is shown in Figure 3.2. The actual basis functions are, however, not block functions with only positive (black) and negative (white) values, but harmonic functions. The black/white alternation in Figure 3.2 only illustrates the frequency behavior with different degrees n and orders m . Three basic types of spherical harmonics can be distinguished. (1) Zonal harmonics ($m = 0$), being symmetric about the rotation axis, represent long-period components of the tidal spectrum, ranging from a few days to several years (Moritz & Mueller, 1987). In that frequency spectrum, zonal harmonics can change the polar moment of inertia and thus can only lead to changes in UT1 (rotation speed). Gross

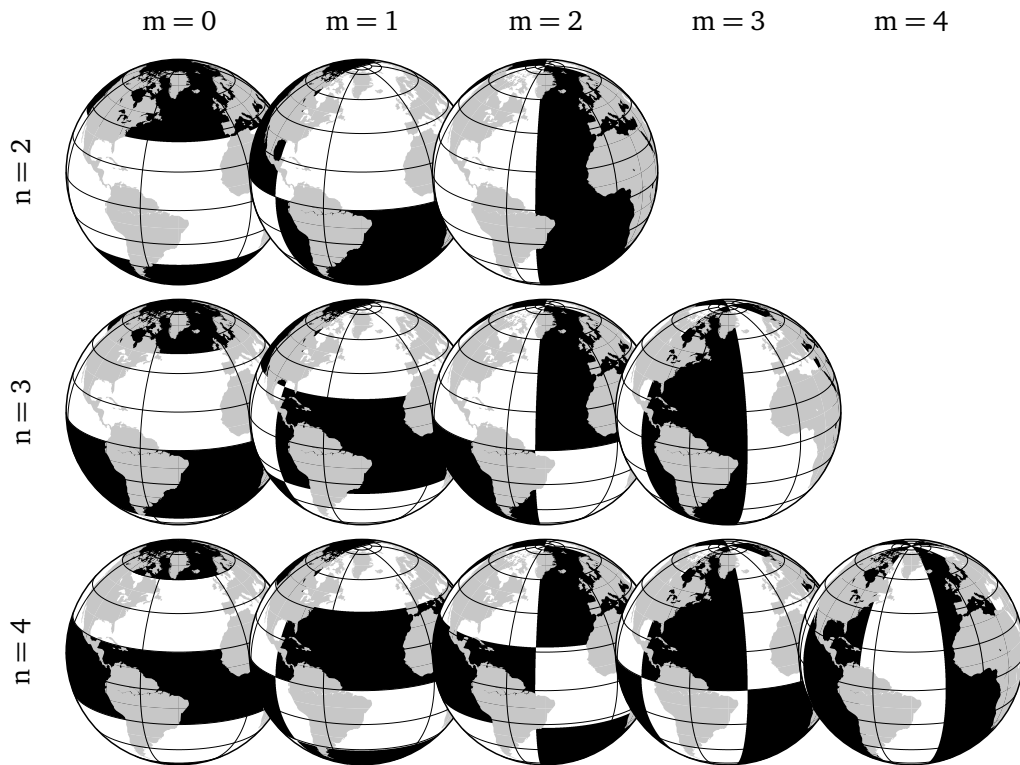


Figure 3.2: Illustration of some spherical harmonics.

(2007) shows, however, that the ocean's response to zonal harmonics can excite polar motion because of the uneven land-ocean distribution on Earth. The zonal spherical harmonics of the tidal potential of degree 2 include implicitly only the declination of the celestial body. The main period of the dominant degree 2-term $V_{\text{tid},20}$, is half the orbital period (14 days for the Moon, around half a year for the Sun); (2) Tesseral harmonics ($0 < m < n$) are latitude and longitude dependent and cause tidal forcing in the diurnal frequency band; (3) Sectorial harmonics ($m=n$) have semi-diurnal periods since they vary with $2\lambda'$, and affect Earth rotation, e.g., through tidal friction (Böhm, 2012; Torge & Müller, 2012).

For the case of solid Earth tides, there is an equivalence of perturbing tidal term, spherical harmonic of the deformation field and, thus, resultant ERP. Because of the complexity of ocean dynamics, the irregular continental shape and the bathymetry, this does not hold for the case of ocean tides. One tidal potential term (degree n , order m) generates ocean tides of other spherical harmonics than that of same degree and order as well (Dehant & Mathews, 2015, p. 253).

The three degree-two tidal potential components are given as

$$V_{\text{tid},20} = GM_{\text{cel}} \frac{R_E^2}{r_{\text{cel}}^3} P_{20}(\sin \varphi) P_{20}(\sin \varphi') \quad (3.14)$$

$$V_{\text{tid},21} = \frac{1}{3} GM_{\text{cel}} \frac{R_E^2}{r_{\text{cel}}^3} P_{21}(\sin \varphi) P_{21}(\sin \varphi') \cos(\lambda - \lambda') \quad (3.15)$$

$$V_{\text{tid},22} = \frac{1}{12} GM_{\text{cel}} \frac{R_E^2}{r_{\text{cel}}^3} P_{22}(\sin \varphi) P_{22}(\sin \varphi') \cos 2(\lambda - \lambda'). \quad (3.16)$$

3.3 Astronomical arguments

If the tidal potential is calculated using Equation (3.6), terrestrial coordinates of the celestial bodies are required. Celestial orbits, on the other hand, can also be expanded into a harmonic series where they vary linear in specific angles. Several tidal potential catalogs have been published using the expansion of celestial arguments, such as the HW95 catalog (Hartmann & Wenzel, 1995). The largest tides of this catalog are presented in Table 3.3. Tidal potential catalogs consist of thousands so-called partial tides, which are spectral components at certain frequencies. Available catalogs differ in their expansion of the tidal potential and their use of astronomical variables. Each partial tide usually consists of an amplitude and an angle argument. The potential amplitudes of the tidal constituents in the diurnal and semi-diurnal frequency bands are shown in Figure 3.3. The angle argument $\phi_j(t)$ is expressed as a linear combination of the astronomical variables F_i using integer coefficients N_{ij} . Each set of these integer multipliers characterizes a particular partial tide, denoted with subscript j . Three variables are required for the lunar orbit, two for the solar orbit. A sixth variable is required to define the time. The angle argument can be calculated using (Beutler *et al.*, 2005)

$$\phi_j(t) = \sum_{i=1}^6 N_{ij} F_i(t). \quad (3.17)$$

Each partial tide contains a constant phase and the frequency is given by the time derivative of Equation (3.17).

Two commonly used sets of astronomical arguments are briefly presented hereafter. Doodson (1921) introduced six independent variables (see Table 3.1) describing relative positions of the Sun and the Moon with respect to the Earth. This set is commonly used by oceanographers. Three of these Doodson variables, s , p and N' , specify the apparent lunar orbit, two of them, h and p_1 , specify the apparent solar orbit, and τ relates the local observer to the hour angle of the Moon.

Numerical values of the Doodson arguments (Table 3.1) can be calculated using (Doodson,

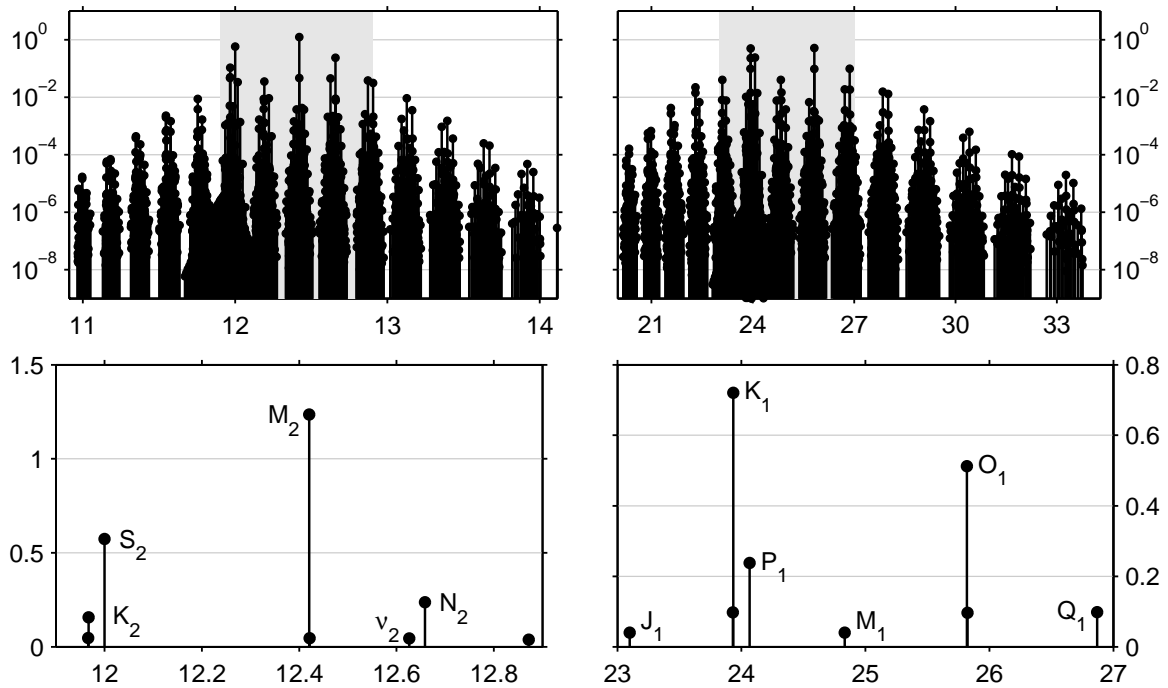


Figure 3.3: Tidal potential amplitudes in m^2/s^2 from the HW95 tidal potential catalog in the semi-diurnal (periods around 12 hours, left) and diurnal (periods around 24 hours, right) range. Top figures show all tidal constituents in logarithmic scale, lower figures show details of the respective grey band in linear scale, i.e., the eight largest tides for each band. Note: The K_1 and K_2 tides consist of a lunar and a solar constituent, in the upper figure they appear as two partial tides, in the lower figure their amplitudes are summed up.

Table 3.1: Doodson arguments (Doodson, 1921).

Symbol	Period	Definition
τ	1.03505 days	Local mean lunar time
s	27.32158 days	Mean longitude of the Moon
h	1 year	Mean longitude of the Sun
p	8.85 years	Longitude of the perigee of the Moon
$N' = -\Omega$	18.61 years	Ω is the longitude of the ascending node of the Moon
p_1	20940 years	Longitude of the perigee of the Sun

Table 3.2: Fundamental (Delaunay) arguments (Petit & Luzum, 2010).

Symbol	Period	Definition
$F_1 \equiv l$	27.53 days	Mean anomaly of the Moon
$F_2 \equiv l'$	365.25 days	Mean anomaly of the Sun
$F_3 \equiv F = L - \Omega$	27.21 days	L is the mean longitude of the Moon
$F_4 \equiv D$	29.53 days	Mean elongation of the Moon from the Sun
$F_5 \equiv \Omega$	18.61 years	Mean longitude of the ascending node of the Moon
$\gamma = \text{GMST} + \pi$	0.99727 days	Greenwich mean sidereal time + π

1921)

$$\begin{aligned}
 \tau &= 15^\circ t + h - s - L, \\
 s &= 277.0248^\circ + 481267.8906^\circ T + 0.0020T^2 + \dots, \\
 h &= 280.1895^\circ + 36000.7689^\circ T + 0.0003T^2 + \dots, \\
 p &= 334.3853^\circ + 4069.0340^\circ T - 0.0103T^2 + \dots, \\
 N' &= 100.8432^\circ + 1934.1420^\circ T - 0.0021^\circ T^2 + \dots, \\
 p_1 &= 281.2209^\circ + 1.7192^\circ T + 0.0005^\circ T^2 + \dots
 \end{aligned} \tag{3.18}$$

where T is Julian centuries (36525 mean solar days) since January 1, 1900 (midnight), t is Greenwich mean solar time, and L is the longitude of a point.

Since the multiplier coefficient of τ is always positive and those of the other arguments are usually within the range -4 to 4, A. Doodson proposed the Doodson numbers to avoid negative coefficients as follows

$$d_j = N_j + [0 \ 5 \ 5 \ 5 \ 5 \ 5]^T. \tag{3.19}$$

The semi-diurnal lunar tide M_2 , for example, has the integer multipliers for the Doodson arguments $[2 \ 0 \ 0 \ 0 \ 0 \ 0]$, being equivalent to a Doodson number of 255.555.

An alternative expression of astronomical variables, commonly used in geodesy, are the fundamental arguments of precession, nutation and Greenwich mean sidereal time, also known as Delaunay variables (Table 3.2, Beutler *et al.*, 2005). The angle arguments are calculated in an analogous manner as for the Doodson arguments (cf. Equation 3.17).

Both sets of astronomical arguments are equivalent and they can be converted by a linear transformation. If the set of Doodson arguments is denoted by β and the Fundamental (Delaunay)

arguments (including γ) by F , then (Gipson, 1996)

$$F = \begin{bmatrix} 0 & 0 & 0 & -1 & 0 & 0 \\ 0 & 0 & 0 & 0 & 0 & -1 \\ -1 & 1 & 1 & 1 & 0 & 1 \\ 0 & 0 & -1 & 0 & 0 & -1 \\ -1 & 1 & 1 & 1 & -1 & 1 \\ 1 & 0 & 0 & 0 & 0 & 0 \end{bmatrix} \beta \quad \beta = \begin{bmatrix} 0 & 0 & 0 & 0 & 0 & 1 \\ 1 & 0 & 1 & 1 & 0 & 1 \\ 0 & 1 & 0 & -1 & 0 & 0 \\ -1 & 0 & 0 & 0 & 0 & 0 \\ 0 & 0 & 1 & 0 & -1 & 0 \\ 0 & -1 & 0 & 0 & 0 & 0 \end{bmatrix} F. \quad (3.20)$$

3.4 Dynamic and equilibrium theory

The tidal potential, as discussed in the previous section, is the main driving force of ocean tides although several other mechanisms, such as ocean bottom friction, Coriolis force, dissipation, ocean bottom topography, atmospheric pressure forcing, or the distribution of land masses have an effect on ocean tides as well. Two different theories describing the reaction of the ocean due to tidal forcing have been developed.

The equilibrium theory neglects the aforementioned effects and is thus mainly of historical interest. However, also modern theories use the phase referencing with respect to the astronomical arguments. It has been developed by Newton and states that the ocean water covering the whole Earth forms a surface in static equilibrium with the tidal potential of a celestial body,

$$\zeta_E = \frac{V_{\text{tid}}}{g}. \quad (3.21)$$

After the initial adjustment of water masses, the two bulges (cf. Figure 3.1) follow the direction to the celestial body due to the rotation of the Earth. The theory considers only mass displacement without making allowance for movements or currents of the water which is why the equilibrium theory cannot reflect reality (Sverdrup *et al.*, 1942, p. 551). Including the oceanic currents would be particularly important for short period tides as equilibrium tidal theory is applied for long-period tides. Furthermore, the equilibrium theory cannot explain extreme tidal ranges of more than 10 m in shelf sea areas as equilibrium tides have amplitudes of less than half a meter (Pugh & Woodworth, 2014, cf. Table 3.3).

The dynamic theory of tides was introduced by Laplace and has replaced the equilibrium theory. It is based on the fact that horizontal forces are important for the movement of water. The type of motion due to periodic horizontal forces will be long waves having the same periods. The dynamic equations (4.1) are complex and include additional conditions for ocean tides such as continuity and momentum balance, the response of the ocean basins, ocean bottom friction, boundary conditions, or the elastic response of the solid Earth (Pugh & Woodworth, 2014; Sverdrup *et al.*, 1942).

Isobaric levels, i.e., levels of constant pressure, are generally inclined to isopycnal levels of

Table 3.3: Ten largest tidal harmonics of long-period, diurnal and semi-diurnal tides. Equilibrium amplitudes in millimeters are shown in column one. The second column shows normalized amplitudes relative to M_2 . Tidal amplitudes are taken from the HW95 catalog (Hartmann & Wenzel, 1995; Pugh & Woodworth, 2014).

	Amplitude	Name	Doodson Nr.	Period	Origin	
Long-period tides ($m = 0$)	135	0.56	M_0	055.555	permanent	Lunar permanent
	62	0.26	S_0	055.555	permanent	Solar permanent
	42	0.17	M_f	075.555	13.66 d	Lunar semi-monthly
	22	0.09	M_m	065.455	27.55 d	Lunar monthly
	19	0.08	S_{sa}	057.555	182.62 d	Solar semi-annual
	18	0.07		055.565	6798 d	
	17	0.07	M'_f	075.565	13.63 d	
	8	0.03	M_{tm}	085.455	9.13 d	Lunar termensual
	4	0.02	MS_m	063.655	31.81 d	
	4	0.02	MS_f	073.555	14.77 d	Lunisolar semi-monthly
Diurnal tides ($m = 1$)	101	0.41	O_1	145.555	25.82 h	Lunar principal
	97	0.40	K_1	165.555	23.93 h	Lunar principal
	47	0.19	P_1	163.555	24.07 h	Solar principal
	45	0.18	K_1	165.555	23.93 h	Solar principal
	19	0.08	Q_1	135.655	26.87 h	Lunar elliptical
	19	0.08	K'_1	165.565	23.93 h	
	19	0.08	O'_1	145.545	25.82 h	
	8	0.03	J_1	175.455	23.10 h	Lunar elliptical
	8	0.03	M_1	155.655	24.83 h	Lunar smaller elliptical
	4	0.02	OO_1	185.555	22.31 h	Lunar second-order
Semi-diurnal tides ($m = 2$)	243	1.00	M_2	255.555	12.42 h	Lunar principal
	113	0.46	S_2	273.555	12.00 h	Solar principal
	47	0.19	N_2	245.655	12.66 h	Lunar larger elliptical
	21	0.09	K_2	275.555	11.97 h	Lunar declinational
	10	0.04	K_2	275.555	11.97 h	Solar declinational
	9	0.04	K'_2	275.565	11.97 h	
	9	0.04	M'_2	255.545	12.42 h	
	9	0.04	ν_2	247.455	12.63 h	Larger evectional
	7	0.03	μ_2	237.555	12.87 h	Variational
	7	0.03	L_2	265.455	12.19 h	Lunar smaller elliptical
Ter-diurnal tides ($m = 3$)						
	3	0.01	M_3	355.555	8.28 h	Lunar parallax

constant density. Then, the flow varies with depth since density varies with depth and horizontal position (Stewart, 2008, p. 163). Such a depth-dependent flow is called baroclinic flow. Barotropic flow, on the other hand, is independent of depth. Depth-averaged flow is commonly used in short period ocean tide models and usually also referred to as barotropic. Assimilation models typically incorporate depth-averaged equations, which are valid from shortest time-scales up to several weeks (Carrère & Lyard, 2003).

3.5 Non-gravitational tides

The linear response of the ocean to tidal forcing as described in the previous sections is the gravitational tide. The tidal potential is well known for a large number of tides and, using the response method (see Section 5.1 for details), one can relate the potential of celestial objects to tidal heights. However, for some tidal constituents, e.g., S_1 , μ_2 , L_2 , S_2 , and M_2 , harmonic analyses find significant discrepancies between observed tidal heights and what is expected from potential catalogs. Two effects, additional to gravitational forcing, changing the height of the ocean surface are radiational tides and non-linear effects (Pugh & Woodworth, 2014, p. 80). The fact that the response method allows the separation of the gravitational part from measured tidal elevations, makes this method such a powerful tool.

Radiational tides

A part of the change of the ocean surface is due to solar heating. An approximation of this effect, called radiational tide by Munk & Cartwright (1966), is the input radiation (Agnew, 2007). Thus, the radiational tides appear at solar tidal frequencies. In the diurnal and sub-diurnal frequency range, the most prominent radiational tides are the S_1 and S_2 tides, at which solar heating contributes significantly to their tidal heights. Both radiational ocean tides S_1 and S_2 are driven by atmospheric processes, i.e., air pressure loading and winds (Ponte, 1994). There is actually no equilibrium tide for S_1 tide, but a small term close to S_1 which cannot be separated from the 24 hours period of S_1 (Pugh & Woodworth, 2014, p. 122). The tidal height of S_1 , mostly driven by atmospheric pressure loading, reaches amplitudes of 2 cm or even more in isolated areas. However, it is less than 1 cm for the most part of the global ocean (Ray & Egbert, 2004).

Also the semi-diurnal S_2 tide has a radiational part, however smaller compared to its gravitationally driven tidal height. As a global average, Arbic (2005) finds an atmospherically driven S_2 tidal height of 14.7% of the gravitational tide and a phase lag of 109.4° .

Even though the physics of the solar heating process is complicated, response analysis allows an approximation of the radiational tide by using the input radiation potential. This is zero during night time and during days roughly proportional to $\cos(\epsilon_{Sun})$, where ϵ_{Sun} is the elevation of the Sun (Agnew, 2007; Pugh & Woodworth, 2014).

Non-linear effects

Non-linear effects are mostly important at coastal regions and in areas of shallow water. There, non-linear physical effects become relevant for the progression of tidal waves. These processes, such as bottom friction, depend on higher orders of the amplitude of the tidal height. Such non-linearities are visible in the time-series of, e.g., tidal height observations. They appear as harmonic variations with frequencies which are differences, multiples, and sums of the non-disturbed, astronomical tidal harmonics (Pugh & Woodworth, 2014). For example, the two largest semi-diurnal tides, M_2 and S_2 , have frequencies $\omega_{M_2} \approx 0.00805^\circ/\text{s}$ and $\omega_{S_2} \approx 0.00833^\circ/\text{s}$. If the square of the sum of M_2 and S_2 is considered, additional harmonic constituents appear as follows: The square of the two cosine functions produce harmonic signals with twice the respective frequencies, $\omega_{M_4} = 2\omega_{M_2}$ and $\omega_{S_4} = 2\omega_{S_2}$, i.e., the tidal constituents M_4 and S_4 . Another non-linear tide in this frequency band, MS_4 , arises at frequency $\omega_{MS_4} = \omega_{M_2} + \omega_{S_2}$. The long-period tide MS_f at frequency $\omega_{MS_f} = \omega_{S_2} - \omega_{M_2}$ has a period of 14.77 days (see Table 3.3). To include other non-linear tides, the process described above needs to be continued for other combinations of tidal constituents and also higher powers. If tidal heights in shallow water regions are modeled in practice, a large number of combinations is necessary (Pugh & Woodworth, 2014).

3.6 Ocean tide models

Three types of ocean tide models can be distinguished. Pure hydrodynamic models solve dynamic equations to derive tidal heights and currents consistent with prescribed physics. If observations of the ocean surface elevation are used to constrain the hydrodynamic equations, e.g., from satellite altimetry or tide gauge observations, the hydrodynamic models are called assimilation models. The third group of models are empirical models which are based only on observations of the surface variability without deploying any hydrodynamic equations. The empirical models therefore only include information about tidal heights but not about tidal currents. The major part of this study deals with the derivation of tidal currents from tidal heights as they are not part of empirical models but play an important role for ERP prediction.

The tidal height of the ocean surface is usually given separately for n harmonic constituents. The total height can be calculated by their sum,

$$\zeta(\varphi, \lambda, t) = \sum_n A_n(\varphi, \lambda) \cos(\omega_n t + \chi_n - g_n(\varphi, \lambda)) \quad (3.22)$$

where φ and λ denote the spherical coordinates latitude and longitude, A_n and g_n are tabulated amplitudes and phase lags with respect to the equilibrium tide maximum, ω_n is the angular velocity of the tidal constituent and t is time. χ_n is an additional angle according to the Doodson-Warburg phase convention. It can be calculated from the sine- and cosine coefficients, C_0 and S_0 ,

Table 3.4: Tidal constituents included in selected ocean tide models. The second column gives the number of constituents for each model.

Model	#	Tides included in model
GOT4.8	12	Sa, Ssa, Mf, Q ₁ , O ₁ , P ₁ , S ₁ , K ₁ , N ₂ , M ₂ , S ₂ , K ₂
EOT11a	13	Mm, Mf, Q ₁ , O ₁ , P ₁ , S ₁ , K ₁ , 2N ₂ , N ₂ , M ₂ , S ₂ , K ₂ , M ₄
HAMTIDE11a	9	Q ₁ , O ₁ , P ₁ , K ₁ , 2N ₂ , N ₂ , M ₂ , S ₂ , K ₂
FES2012	33	Z ₀ , Ssa, Mm, MSf, Mf, Mtm, Q ₁ , O ₁ , P ₁ , S ₁ , K ₁ , J ₁ , E ₂ , 2N ₂ , μ ₂ , N ₂ , ν ₂ , M ₂ , MKS ₂ , λ ₂ , I ₂ , T ₂ , S ₂ , R ₂ , K ₂ , M ₃ , N ₄ , MN ₄ , M ₄ , MS ₄ , S ₄ , M ₆ , M ₈

of the tidal potential,

$$\chi_n = \begin{cases} -90^\circ & \text{diurnal: } C_0 \text{ or } S_0 > 0 \\ 0 & \text{long-period: } C_0 \text{ or } S_0 < 0, \text{ semi-diurnal: } C_0 \text{ or } S_0 > 0 \\ 90^\circ & \text{diurnal: } C_0 \text{ or } S_0 < 0 \\ 180^\circ & \text{long-period: } C_0 \text{ or } S_0 > 0, \text{ semi-diurnal: } C_0 \text{ or } S_0 < 0 \end{cases} \quad (3.23)$$

or, equivalently, from the astronomical amplitudes H_f (Petit & Luzum, 2010, Table 6.6).

Nodal corrections and admittance approach

If the observation period of the ocean surface is long enough and an ocean tide model consists of all significant harmonic tidal constituents, the tidal variation of the ocean surface would be well represented by Equation (3.22). However, since that is not the case, the principal lunar tides are modulated by the 18.6 years period of the ascending node and the 8.85 years period of the perigee of the Moon. To account for this modulation, two nodal correction parameters are applied to the harmonic function. Nodal factors $f_n(t)$ are multipliers for the amplitudes, and nodal angles $u_s(t)$ are added to the cosine argument. For solar constituents, the amplitude factor is one and the additional angle is 0.

Usually only a limited set of partial tides are included in current ocean tide models. An overview of available tides in the ocean tide models mentioned in the following section is given in Table 3.4. All others cannot be significantly identified in the tidal analysis. Hence, both minor tides and side lobes have to be accounted for. Minor tides are interpolated by admittance theory, assuming that the ratio of tidal heights and tidal potential is a slowly varying function of frequency (Munk & Cartwright, 1966). The admittance approach is explained in more detail in Section 5.1.

The current velocities of an ocean tide model are given as periodic variations in eastward and northward direction u_n and v_n , similarly to the variation of the tidal height (Equation 3.22). Instead of current velocities, volume transport, i.e., velocity multiplied by ocean depth D can be

used to represent the flow of the ocean,

$$\begin{aligned}U_n &= u_n \cdot D \\V_n &= v_n \cdot D.\end{aligned}\tag{3.24}$$

Current ocean tide models

The following gives a brief overview about global ocean tide models being related to this work either because they are used as input or for comparison or because they have been derived similarly. All models but EOT11a contain barotropic oceanic currents. Most information of this section are taken from Stammer *et al.* (2014).

GOT4.8

The Goddard Ocean Tide model should be mentioned here because the volume transports of GOT are derived similarly as in the present work. The tidal heights result from an empirical tidal analysis of several altimeter missions adopted to a prior FES model (Ray, 1999). Barotropic current velocities were derived from a least-squares solution of the momentum and continuity equations as mentioned in Ray (2001). The resolution of the model is 0.5° .

EOT11a

The empirical solution being closely related to this work is the global ocean tide model developed at Deutsches Geodätisches Forschungsinstitut (DGFI). It is based on altimetry observations from Topex, Jason-1, Jason-2, ERS-2 and Envisat. This model also uses the FES solution as reference model. Outside the latitude range $\pm 81.5^\circ$ EOT11a falls back to tidal heights from FES2004. The model applies relative weighting and specific offsets for different missions in order to consider differences in hardware and accuracies. In addition to the eight major tides, EOT11a consists of $2N_2$, S_1 , M_4 and the long-term constituents M_m and M_f . The spatial resolution is 0.125° or 7.5 arc-minutes (Savcenko & Bosch, 2012).

HAMTIDE11a

The assimilation model from the University of Hamburg is the predecessor of HAMTIDE12 and based on hydrodynamic equations and data assimilation (Taguchi *et al.*, 2014). The grid is equal to the FES2004 grid, tidal heights from EOT11a were assimilated between latitudes $+74^\circ$ and -84° .

FES2012

Another assimilation model being related to this work is the 2012 version of the finite element tidal solution (FES) model (Carrère *et al.*, 2012). Being the successor of the FES2004

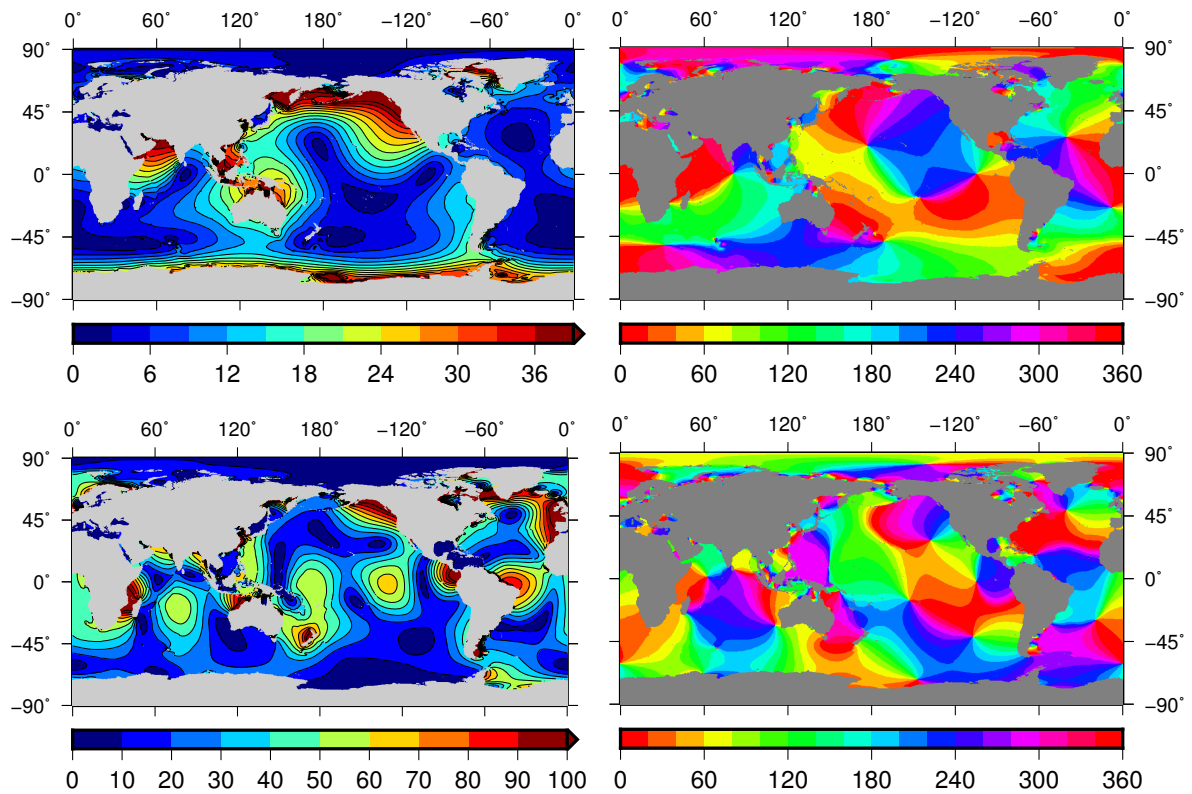


Figure 3.4: Tidal height variations from the hydrodynamic ocean tide model HAMTIDE11a for partial tides K_1 (upper plots) and M_2 (lower plots). Amplitudes (left) are given in centimeters, phases (right) are given in degrees.

(Lyard *et al.*, 2006), FES2012 is derived from shallow water equations assimilated mainly by data from Topex/Poseidon, Jason-1, and Jason-2 missions. Further data sources were used in regions showing small scale patterns and the Arctic. The resolution of the unstructured grid is 0.0625° or 3.75 arc-minutes.

3.7 Ocean tidal effects on Earth rotation

The angular momentum approach is based on the balance of the angular momentum of the Earth and the angular momentum of the oceans (and other fluids; Wahr, 1982). Thus, the total OTAM is of the same magnitude as the angular momentum of the solid Earth but of opposite sign to conserve the angular momentum of the system (McCarthy & Seidelmann, 2009, p. 276).

Under angular momentum conservation, any mass redistribution on the Earth excites Earth rotation variations (Chao & Ray, 1997). Changes in polar motion and LOD are excited by two mechanisms (cf. Equations 2.31 and 2.32): (1) Mass redistribution, changing the inertia tensor $\Delta \mathbf{I}$, usually referred to as mass term; (2) motion relative to the rotating reference frame changing the relative angular momentum \mathbf{h} , usually referred to as motion term (Gross, 2007; Munk & MacDonald, 1960). The mass term is represented by the tidal heights of the ocean surface, the motion

term arises from oceanic currents. The OTAM for each frequency are computed by integration using (Chao & Ray, 1997)

$$\begin{aligned}
 H_1(\omega) = & -R_E^4 \rho \Omega \iint \zeta(\omega) \cos^2 \varphi \sin \varphi \cos \lambda \, d\lambda \, d\varphi \\
 & + R_E^3 \rho \iint (V(\omega) \sin \lambda - U(\omega) \sin \varphi \cos \lambda) \cos \varphi \, d\lambda \, d\varphi
 \end{aligned} \tag{3.25}$$

$$\begin{aligned}
 H_2(\omega) = & -R_E^4 \rho \Omega \iint \zeta(\omega) \cos^2 \varphi \sin \varphi \sin \lambda \, d\lambda \, d\varphi \\
 & - R_E^3 \rho \iint (V(\omega) \cos \lambda + U(\omega) \sin \varphi \sin \lambda) \cos \varphi \, d\lambda \, d\varphi
 \end{aligned} \tag{3.26}$$

$$\begin{aligned}
 H_3(\omega) = & R_E^4 \rho \Omega \iint \zeta(\omega) \cos^3 \varphi \, d\lambda \, d\varphi \\
 & + R_E^3 \rho \iint U(\omega) \cos^2 \varphi \, d\lambda \, d\varphi.
 \end{aligned} \tag{3.27}$$

where R_E is the mean radius of the Earth, ρ is the mean density of sea water, Ω is the mean rotational speed of the Earth, λ and φ are longitude and latitude, $U(\omega)$ and $V(\omega)$ are (barotropic) volume transport in λ and φ direction, respectively (cf. Equation 3.24). The first rows in Equations (3.25)–(3.27) denote the mass term, the second rows describe the motion term. $\zeta(\omega)$ is the harmonically varying ocean height. All harmonic constituents— $\zeta(\omega)$, $U(\omega)$, and $V(\omega)$ —are complex amplitudes of the form

$$\hat{\zeta} = A e^{-i\varphi} \tag{3.28}$$

where A is the amplitude and φ is the phase lag, allowing for straightforward numerical integration.

The numerical integration over global grids is done applying the Simpson cubature (Engeln-Müllges *et al.*, 2011) for all subsequent calculations.

The polar motion and LOD variations excited by OTAM can be calculated using a proper linear combination of $\Delta \mathbf{I}$ and \mathbf{h} . This transfer needs to take into account various geophysical effects and—for polar motion—the resonance frequencies of the free modes of the Earth, namely CW and FCN (Chao & Ray, 1997). The FCN frequency is given by $\omega_{\text{FCN}} = -1.0023203$ cpsd (Mathews *et al.*, 1991, as cited in Gross, 1993). The CW frequency is $\omega_{\text{CW}} = 2\pi(1 + i/(2Q))/T$ where $T = 434.45$ sidereal days is the observed Chandler period and $Q = 170$ is the quality factor due to energy dissipation (Wilson & Vicente, 1980, as cited in Gross, 1993).

Gross (1993) summarizes the transfer function for polar motion as follows

$$\begin{aligned} \mathbf{p}(\omega) = & \left(2.554 \cdot 10^{-4} \frac{\Omega}{\omega_{\text{FCN}} - \omega} + 2.686 \cdot 10^{-3} \frac{\Omega}{\omega_{\text{CW}} - \omega} \right) \frac{\Omega \Delta \mathbf{I}(\omega)}{A \Omega \tau} \\ & + \left(6.170 \cdot 10^{-4} \frac{\Omega}{\omega_{\text{FCN}} - \omega} + 1.124 \frac{\Omega}{\omega_{\text{CW}} - \omega} \right) \frac{\mathbf{h}(\omega)}{A \Omega} \end{aligned} \quad (3.29)$$

where $\tau = \Omega^2 R_E^5 / (3GA)$, R_E is the mean radius of the Earth, G is the universal gravitational constant, ω_{FCN} and ω_{CW} are the frequencies of FCN and CW, respectively, and A is the least principal moment of inertia.

When OTAM values are derived for the mass and motion terms, they need to be converted to prograde and retrograde components, because of the CIP frequency conventions (cf. Section 2.1 and Figure 2.1) prior to calculating ERP corrections using Equations (3.29) and (3.33).

If cosine- and sine-amplitudes (in-phase and quadrature components, see Equation 4.14) for OTAM are used instead of amplitudes and phases, the prograde and retrograde components can be calculated as well. The cosine- and sine-amplitudes are commonly used when tidal terms are fitted to time series, since they give linear equations in a least-squares adjustment. The conversion from cosine- and sine-amplitudes, px_c and py_s for the case of x-pole, to pro- and retrograde components is given as

$$\begin{aligned} A_p &= -\frac{1}{2}(px_c + py_s) \\ B_p &= +\frac{1}{2}(px_s - py_c) \\ A_r &= -\frac{1}{2}(px_c - py_s) \\ B_r &= -\frac{1}{2}(px_s + py_c). \end{aligned} \quad (3.30)$$

After considering the CIP frequency convention, A_p , B_p , A_r , and B_r are converted to polar motion variations using Equation (3.29). Pro- and retrograde amplitudes A and phases φ are derived analogously to classical harmonic motions,

$$\begin{aligned} A_{p,r} &= \sqrt{A_{p,r}^2 + B_{p,r}^2} \\ \varphi_{p,r} &= \arctan\left(\frac{B_{p,r}}{A_{p,r}}\right). \end{aligned} \quad (3.31)$$

Final polar motion corrections are usually given as amplitudes and phases of x - and y -

components. Cosine and sine-amplitudes are derived using

$$\begin{aligned}
 px_c &= -A_p - A_r \\
 px_s &= +B_p - B_r \\
 py_c &= +B_p + B_r \\
 py_s &= +A_p - A_r.
 \end{aligned}
 \tag{3.32}$$

The LOD transfer function reads

$$\Delta\text{LOD}(t) = \frac{\text{LOD}_0}{C_m \Omega} (h_3(t) + 0.756 \Omega \Delta I_{33}(t))
 \tag{3.33}$$

where $\text{LOD}_0 = 86400$ s is the nominal length of day and C_m is the greatest principal moment of inertia of the crust and mantle of the Earth (cf. Equation 2.11; Gross, 1993). Because of the ΔLOD to UT1 correlation (Equation 2.5), the resultant UT1 variation is given by

$$\begin{aligned}
 \Delta\text{UT1}_c &= \frac{\Delta\text{LOD}_s}{\omega \cdot \text{LOD}_0} \\
 \Delta\text{UT1}_s &= -\frac{\Delta\text{LOD}_c}{\omega \cdot \text{LOD}_0}
 \end{aligned}
 \tag{3.34}$$

where subscripts c and s denote cosine- and sine-amplitudes, respectively, and ω is the tidal frequency.

Chapter 4

Estimation of oceanic currents from measured elevations

When using the angular momentum approach (see Section 3.7), tidal corrections for ERP, namely polar motion and ΔLOD , require knowledge of (1) changes of the inertia tensor (mass term of OTAM) and (2) changes in relative angular momentum (motion term of OTAM). If applied to ocean tides, the former is given by the tidal elevation field, the latter by tide-induced oceanic currents. The tidal heights can be derived from satellite altimetry (see Section 3.1), the derivation of global tidal currents requires a modeling approach due to lack of widely distributed and accurate in situ measurements. In principle, there are two ways of deriving tidal currents using measurements of the ocean surface: the gradient approach and full hydrodynamic modeling. Both are briefly described below. In addition, there has been published an intermediate technique which is used in the present work and described in the following sections.

A commonly used strategy to determine oceanic currents is to use depth-averaged momentum equations which relate the flow to the elevation gradient (Cartwright *et al.*, 1992). However, Ray (2001) states three main shortcomings of this procedure. (1) The estimated flow is very sensitive to elevation errors due to the gradient formulation; (2) mass conservation might not be satisfied; and (3) there are singularities at “critical” latitudes where inertial currents exist without elevation gradient (Cartwright *et al.*, 1992; Ray, 2001).

The “full” modeling approach, on the other hand, determines the flow based on hydrodynamic equations including observation constraints. Observations are “assimilated” into the model while it is forward integrated in time, and their errors are accounted for through covariance information. There are several approaches of assimilation schemes which have been reviewed by Egbert & Bennett (1996). Two of the ocean tide models described in Section 3.6, namely FES2012 and HAMTIDE11a, fall in the category of hydrodynamic assimilation models.

This work uses an intermediate method, suggested by Ray (2001). A similar technique has been published by Zahel (1991, 1995). The former uses (known) tidal heights as input and keeps them fixed throughout the estimation process. The three problems of the Cartwright *et al.* (1992) procedure are dealt with by applying a continuity equation ensuring mass conservation. Due to

the continuity constraint the usually locally solved equations turn into a global inversion, which, however, can be solved much faster than full data assimilation (Ray, 2001). This method of deriving horizontal tidal velocities is used in the present work and, thus, is described in more detail in the following section.

4.1 Dynamic equations

The barotropic equations of horizontal motion are depth-averaged, linearized and simplified Navier-Stokes equations for a shallow and incompressible fluid on a rotating and spherical Earth. They are given by (Ray, 2001)

$$\mathbf{u}_t - f \mathbf{k} \times \mathbf{u} + \frac{\mathbf{F}}{\rho D} = -g \nabla (\zeta - \zeta_E - \zeta_{\text{SAL}}) \quad (4.1)$$

$$\zeta_t = -\nabla(D\mathbf{u}) \quad (4.2)$$

where subscripts denote partial derivatives, e.g., $\mathbf{u}_t = \frac{\partial \mathbf{u}}{\partial t}$, $\mathbf{u} = (u, v)$ where u and v are horizontal velocity components in eastward and northward direction, respectively. The second term in Equation (4.1) is a Coriolis term with $f = 2\Omega \sin \varphi$ being the Coriolis parameter and \mathbf{k} being a unit vector in local vertical direction. The Earth rotation vector in the local coordinate system (east, north, up) is $\boldsymbol{\Omega}_{(\text{uvz})} = (0, \Omega \cos \varphi, \Omega \sin \varphi)$. The Coriolis term, $\mathbf{f}_{\text{Cor}} = 2\boldsymbol{\Omega}_{(\text{uvz})} \times \mathbf{u}$, equals $f \mathbf{k} \times \mathbf{u}$ if the z coordinate of \mathbf{u} and \mathbf{f}_{Cor} is set to zero. The mean density of sea water is $\rho = 1027 \text{ kg/m}^3$ (Kämpf, 2010, p. 107). ∇ is the Nabla operator and denotes horizontal partial derivatives. The stress term \mathbf{F} could represent different physical mechanisms, such as bottom friction or turbulent eddy viscosity (Mirabito *et al.*, 2011; Ray, 2001). ζ denotes the (measured) tidal heights of the ocean surface which have to be corrected for the equilibrium tide ζ_E and the self-attraction and loading tide ζ_{SAL} , both of which constitute forcing terms for the tidal flow. D is the undisturbed water depth. Equation (4.2) is the continuity equation for proper mass conservation.

Bottom friction removes energy from the flow and, thus, opposes the motion of water particles (Pugh & Woodworth, 2014). A physically reasonable dissipation term due to bottom friction is typically quadratic in velocity, $\mathbf{F} = c_D |\mathbf{v}| \mathbf{v}$, where \mathbf{v} is the total velocity vector and the parameter c_D is typically 0.003 (Egbert & Erofeeva, 2002). However, the inversion strategy adopted in the following requires a linear parameterization. Egbert *et al.* (1994) use a linear drag coefficient κ so that the frictional drag terms become

$$\begin{aligned} F_\lambda &= \kappa \rho u \\ F_\varphi &= \kappa \rho v \end{aligned} \quad (4.3)$$

where κ is in the range between 0 and 0.1 ms^{-1} (Ray, 2001).

The tidal constituents in Equations (4.5)–(4.7)— ζ , ζ_E , ζ_{SAL} , u , and v —are expressed in the

form

$$\zeta = \hat{\zeta} e^{i\omega t}, \quad (4.4)$$

where hat ($\hat{}$) variables are complex amplitudes as defined in Equation (3.28) and ω is the angular frequency of the particular partial tide. Then, Equations (4.1) and (4.2) can be rewritten as (Logotov & Lermusiaux, 2008; Ray, 2001)

$$i\omega \hat{U} - f \hat{V} + \frac{\kappa \hat{U}}{D} = -\frac{gD}{R_E \cos \varphi} \frac{\partial}{\partial \lambda} (\hat{\zeta} - \hat{\zeta}_E - \hat{\zeta}_{\text{SAL}}) \quad (4.5)$$

$$i\omega \hat{V} + f \hat{U} + \frac{\kappa \hat{V}}{D} = -\frac{gD}{R_E} \frac{\partial}{\partial \varphi} (\hat{\zeta} - \hat{\zeta}_E - \hat{\zeta}_{\text{SAL}}) \quad (4.6)$$

$$\frac{1}{R_E \cos \varphi} \left[\frac{\partial \hat{U}}{\partial \lambda} + \frac{\partial (\hat{V} \cos \varphi)}{\partial \varphi} \right] = -i\omega \hat{\zeta}. \quad (4.7)$$

The spherical coordinates are longitude λ and latitude φ , $f = 2\Omega \sin \varphi$ is the Coriolis parameter, and R_E is the radius of the Earth. \hat{U} and \hat{V} denote the unknown volume transport parameters (cf. Equation 3.24).

4.1.1 Equilibrium tide

The astronomically forced equilibrium tide was introduced in Section 3.4. However, due to the elastic response of the solid Earth and the altered gravitational potential, ζ_E needs to be modified by a factor $\gamma_2 = 1 + k_2 - h_2$ accounting also for the FCN (Wahr, 1981; Wahr & Sasao, 1981), so that (Hendershott, 1972; Pugh & Woodworth, 2014; Ray, 2001)

$$\zeta_E = \gamma_2 \frac{V_{\text{tid}}}{g}. \quad (4.8)$$

The degree-2 Love numbers k_2 and h_2 describe (1) the potential perturbation due to solid Earth deformation; and (2) the deformation of the solid Earth due to tidal loading (Hendershott, 1972). The presented algorithm uses astronomical amplitudes and Love number factors from Arbic *et al.* (2004) which are listed in Table 4.1. The equilibrium tide of diurnal (index d) and semi-diurnal (index s) tides can be computed using

$$\begin{aligned} \zeta_{E,d}(\varphi, \lambda, t) &= A\gamma_2 \sin(2\varphi) \cos(\omega t + \lambda) \\ \zeta_{E,s}(\varphi, \lambda, t) &= A\gamma_2 \cos^2 \varphi \cos(\omega t + 2\lambda). \end{aligned} \quad (4.9)$$

Equilibrium amplitudes of partial tides not being mentioned in Table 4.1, e.g., $2N_2$ for EOT11a, are calculated proportionally from the normalized tidal potential amplitudes (see Table 3.3). The

Table 4.1: Astronomical amplitudes and Love number factors used for the calculation of the equilibrium tide. Taken from Arbic *et al.* (2004).

Partial tide	ω ($10^{-4}s^{-1}$)	A (cm)	$1 + k_2 - h_2$
Q_1	0.6495854	1.9273	0.695
O_1	0.6759774	10.0661	0.695
P_1	0.7252295	4.6848	0.706
K_1	0.7292117	14.1565	0.736
N_2	1.378797	4.6397	0.693
M_2	1.405189	24.2334	0.693
S_2	1.454441	11.2743	0.693
K_2	1.458423	3.0684	0.693

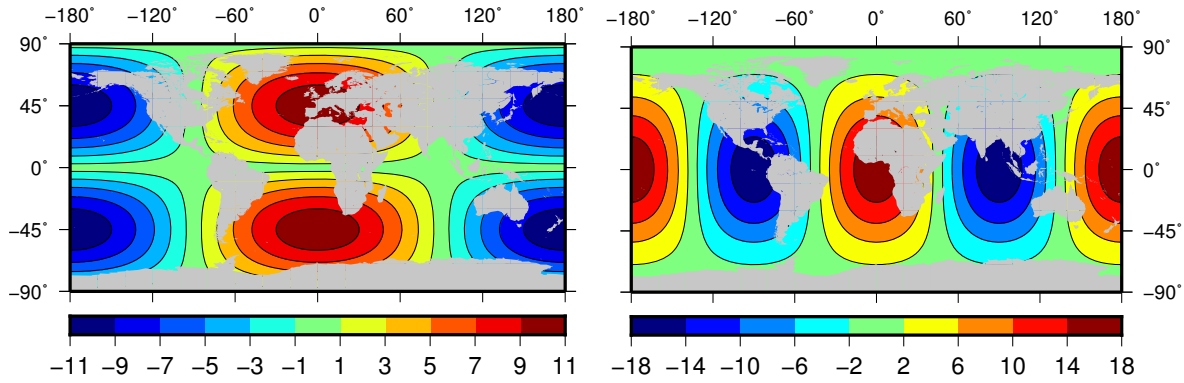


Figure 4.1: Equilibrium tides at $t = 0$ for partial tides K_1 (left) and M_2 (right) in centimeters. Amplitudes and values for γ_2 , being a combination of Love numbers, are taken from Arbic *et al.* (2004).

amplitudes A in Equation (4.9) can also be calculated from the HW95 tidal potential catalog using

$$A = \begin{cases} 3\sqrt{\frac{10}{24}} \cdot S/g & \text{for diurnal tides} \\ 3\sqrt{\frac{10}{24}} \cdot C/g & \text{for semi-diurnal tides} \end{cases} \quad (4.10)$$

where S and C are the sine- and cosine wave amplitudes in the HW95 catalog and g is the gravitational acceleration. The equilibrium tides for a diurnal (K_1) and a semi-diurnal tide (M_2) are shown in Figure 4.1. The latitude dependence and the longitude variation due to different frequencies of diurnal and semi-diurnal tides can be clearly seen.

As all calculations are performed in frequency domain and the equilibrium tide is subtracted from the measured tidal height (Equations 4.5 and 4.6), their phase reference needs to be in accordance with those of the tidal heights. Therefore an initial phase lag is introduced with respect to $t = 0$ according to the fundamental arguments from Simon *et al.* (1994), as cited in

Hartmann & Wenzel (1995).

4.1.2 Loading and self-attraction

The loading and self-attraction denotes a feedback effect on tidal dynamics. Tidal heights need to be corrected for elastic yielding of the solid Earth and for self-attraction. The solid Earth deforms due to the change of the astronomical potential, which is accounted for by the equilibrium tide. In addition the tidal elevation is affected by the depression of the ocean bottom under the weight of the water column above. This rearrangement of the solid Earth changes the gravitational field giving a second feedback effect to the system. The additional water masses, furthermore, apply a gravitational self-attracting force on the nearby water particles (Müller & von Storch, 2004; Stepanov & Hughes, 2004).

These effects, yielding of the solid Earth affecting tidal heights and additional attractions, are corrected for by the self-attraction and loading (SAL) tide and have the same form as atmospheric pressure forcing if a barotropic model is considered. It introduces a correction of about 10% of the tidal height in the gradient term (Accad & Pekeris, 1978). A rigorous computation of the SAL tide requires either a convolution of the tidal height with a proper kernel (Green's function; Hendershott, 1972) or, equivalently, a spherical harmonic expansion using Love numbers (Stepanov & Hughes, 2004). Both of the rigorous calculation methods are computationally expensive as, for example, the convolution requires a global integral over the whole ocean for every grid point.

Accad & Pekeris (1978) use a simple proportionality factor to calculate the SAL tide ζ_{SAL} from the tidal elevation ζ : $\zeta_{\text{SAL}} = \beta \zeta$ with $\beta = 0.085$. However, Ray (1998) showed that a global value for the scalar approximation generates considerable errors, mostly in shallow water areas, and should, thus, be replaced by an integral calculation. For few applications, the approximative SAL tide might still be eligible. As Earth rotations variations are sensitive only to the integrated oceanic currents, a simple form might, thus, be justified. The present study, however, computes the SAL tide from the full computation using convolution with Green's functions.

The calculation of ζ_{SAL} using convolution with a weighting function is given by (Ray, 1998)

$$\zeta_{\text{SAL}}(\varphi, \lambda) = \rho_w R_E^2 \iint \zeta(\varphi', \lambda') G(\psi) \cos \varphi' d\varphi' d\lambda' \quad (4.11)$$

where ρ_w is a mean value for the density of ocean water and $G(\psi)$ are kernel functions depending only on the angular distance ψ from the load. As $(\rho_w \cdot R_E^2 \cdot \zeta)$ gives units of kg, proper Kernel functions G must relate a 1 kg mass at an angular separation of ψ to ζ_{SAL} . Green's Kernel functions can be calculated by (Farrell, 1973)

$$G(\psi) = \frac{R_E}{M_E} \sum_{n=0}^{\infty} (1 + k'_n - h'_n) P_n(\cos \psi) \quad (4.12)$$

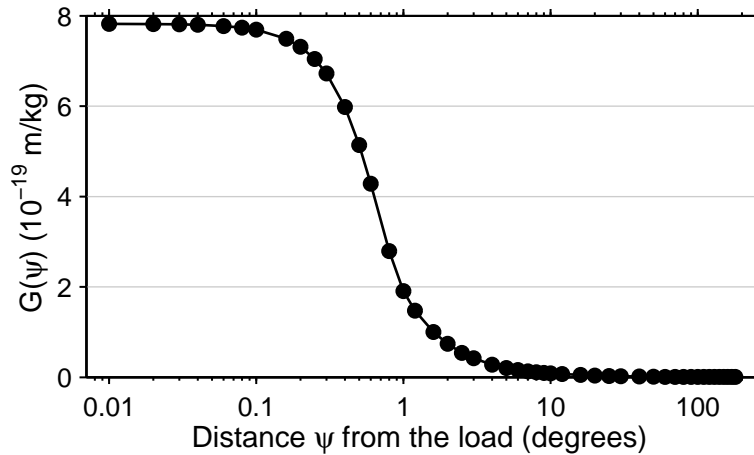


Figure 4.2: Green's function values for vertical displacement (geoid minus seafloor) due to a load, distributed as cosine function, at distance ψ . The radius of the Earth $R_E = 6371$ km. Modified from Stepanov & Hughes (2004).

where $M_E = 5.9736 \cdot 10^{24}$ kg is the mass of the Earth. The radius of the Earth $R_E = 6371$ km. The Love number k'_n accounts for the additional gravitational effect due to the yielding of the solid Earth, and h'_n describes the Earth loading. When a proper combination of these load Love numbers is used, $G(\psi)$ relates the vertical uplift of the geoid relative to the ocean bottom to a mass load at distance ψ . To cope with the singularity at the point itself, an extrapolation to $\psi = 0$ and the mass distributed as a cosine function with radius 1 degree has been used (Stepanov & Hughes, 2004). The Green's function values as tabulated in the paper are shown in Figure 4.2. All subsequent calculations of the SAL tide use those values for $G(\psi)$. Figure 4.3 shows amplitudes and phases for two partial tides (K_1 and M_2) for tidal height variations from the assimilation model HAMTIDE11a.

4.2 Algorithm and numerics

The linear system of Equations (4.5)–(4.7), supplemented by no-flow boundary conditions, is of form $\mathbf{Ax} = \mathbf{b}$, where \mathbf{A} is the design or coefficient matrix, \mathbf{x} is the vector of unknown volume transports and \mathbf{b} is the right-hand side vector containing observed (tidal elevations), computed (ζ_S) or known (ζ_E) quantities.

A staggered C-grid is used for the discretization on a global grid. Arakawa & Lamb (1977) studied the space discretization error for geostrophic currents on different grid schemes. They find best results for the staggered scheme C, subsequently called C-grid. The grid positions of the variables—i.e., tidal heights ζ and eastward and northward velocity components u and v —are shown in Figure 4.4. The spatial resolution of the global grid is 0.5° both for ζ and for the unknown volume transports. The \mathbf{A} matrix then has roughly 500 000 rows and 300 000 columns (more equations than unknowns). The system is, thus, over-determined and can be solved in a least-squares manner (Ray, 2001).

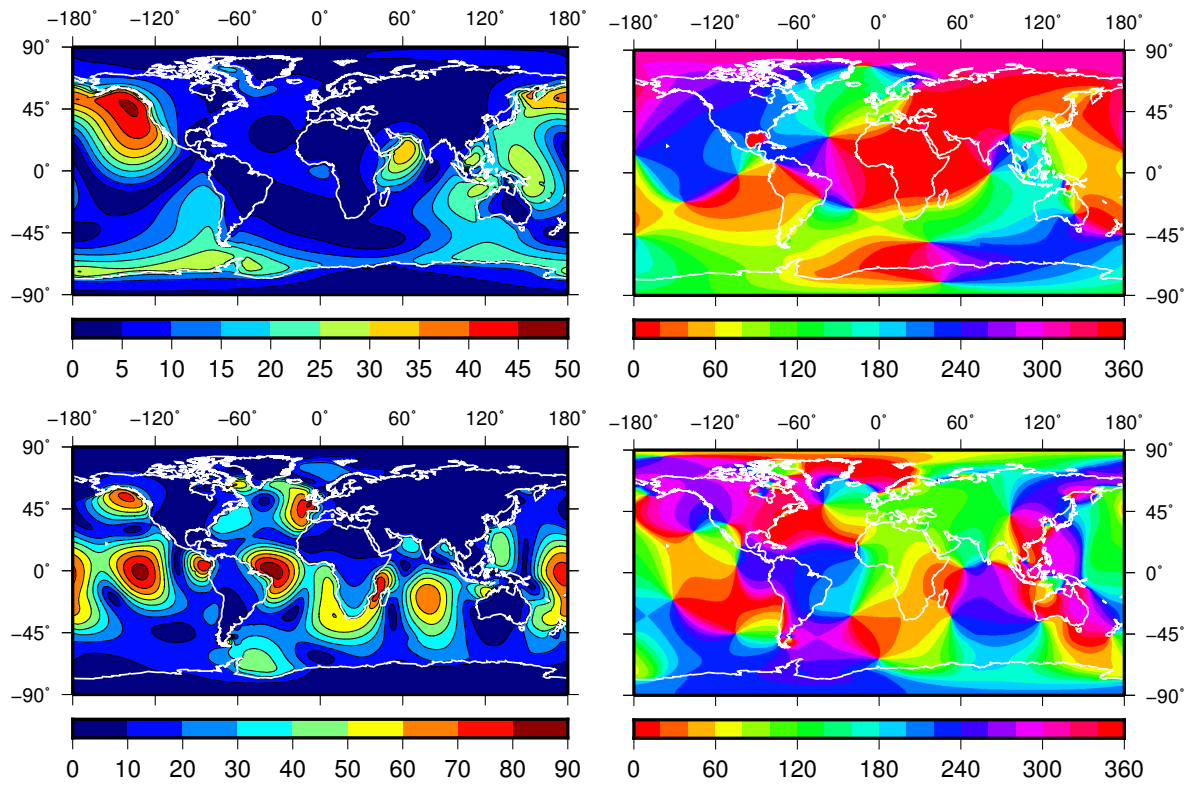


Figure 4.3: Self-attraction and loading (SAL) tides for partial tides K_1 (upper) and M_2 (lower). Amplitudes (left) are given in millimeters, phases (right) in degrees. Surface elevation data are taken from the assimilation model HAMTIDE11a.

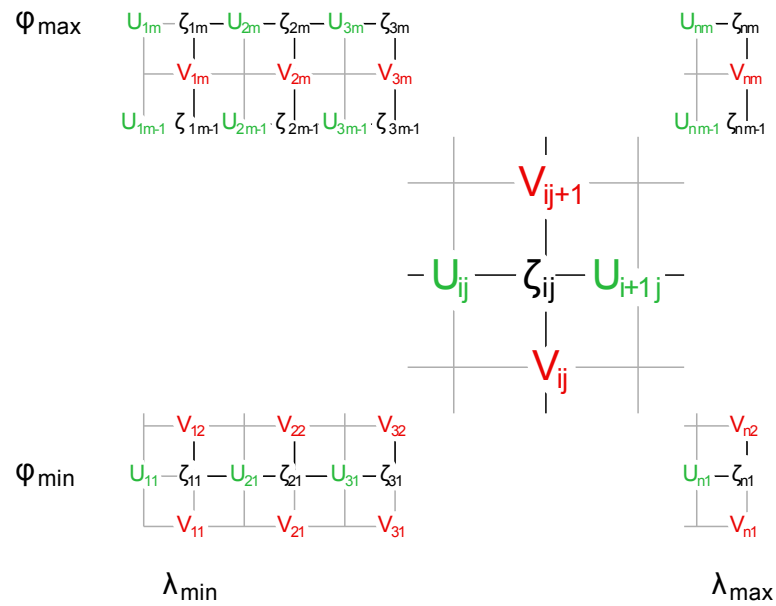


Figure 4.4: Finite difference grid layout (C-grid, after Egbert & Erofeeva, 2002, Fig. 1).

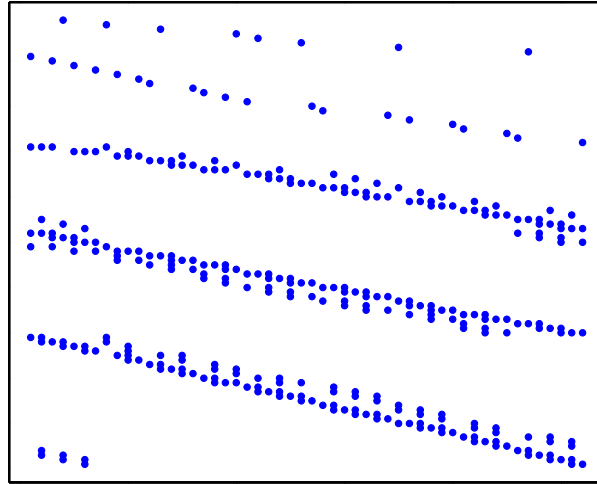


Figure 4.5: Pattern of non-zero elements in the A matrix when using a C-grid. This illustration corresponds to a spatial resolution of 40° .

No-flow boundaries set the flux in the direction (East-West or North-South) normal to the land-ocean boundary (meridional or parallel) to zero. This constraint is applied to grid points at closed boundaries, i.e., points where one of the two neighboring tidal height points is an ocean point and the second is a land point. More precisely, the grid point $U_{i,j}$ is a border point, and, thus, gets a no-flow condition, if $\zeta_{i-1,j}$ or (exclusive or) $\zeta_{i,j}$ is an ocean point. Similarly, $V_{i,j}$ gets a no-flow constraint, if $\zeta_{i,j-1}$ or (exclusive or) $\zeta_{i,j}$ is an ocean point. As will be shown in a later section, relaxing the no-flow boundary condition by a factor of 0.1 slightly improves the estimated oceanic currents. Each grid point in the open ocean generates four non-zero elements for the continuity equation (4.7), and five elements for the momentum equations (4.5–4.6) as the Coriolis term is averaged over the four surrounding C-grid elements. Thus, the system is sparse and has 2350578 non-zero elements for the case of a 0.5° resolution grid. This corresponds to a relative number of 99.9987% zero elements. The sparsity pattern of the coefficient matrix is shown in Figure 4.5. The first two inclined “lines” show the coefficients for the no-flow boundaries at coastal borders. The third line corresponds to the continuity equation, the fourth and fifth line to the momentum equations. The six dots at the lower left also arise from the momentum equations.

Due to the large number of equations and unknowns, an iterative algorithm is used for solving the system in a least squares manner. The algorithm *LSQR*, described by Paige & Saunders (1982), minimizes $\|\mathbf{Ax} - \mathbf{b}\|_2$ and is similar to the conjugate gradients method. It is also used by Ray (2001) and Zahel (1995). An iterative method for solving least-squares problems might require a preconditioner to achieve faster convergence. The system of equations including a preconditioner reads

$$\mathbf{AM}^{-1}\mathbf{Mx} = \mathbf{b} \quad (4.13)$$

with \mathbf{M} being the preconditioning matrix. The iterative method then solves $\mathbf{AM}^{-1}\mathbf{y} = \mathbf{b}$ and the

unknowns can eventually be calculated using $\mathbf{x} = \mathbf{M}^{-1}\mathbf{y}$. Similar to Ray (2001), a preconditioner for matrix \mathbf{A} is used to set all columns to unit \mathbf{L}^2 norm. This makes \mathbf{M}^{-1} a diagonal matrix. The iterative solver converges approximately twice as fast when a preconditioner as described is used.

4.3 Inversion Results

The results in this chapter describe a “calibration” of the inversion algorithm using tidal heights from HAMTIDE11a as input. The estimated volume transports can be consistently compared to HAMTIDE11a volume transports. However, as will be shown in the following sections, the inversion process depends on a variety of other input parameters and settings and, thus, requires several adjusting steps. This chapter also quantifies different inputs and configurations and gives an overview of expected accuracies. The “optimal” parameters found in this chapter eventually serve as starting point for the final inversion using the empirical tidal heights from EOT11a. Furthermore, the following Chapter 5 slightly refines the parameterization to achieve the best results using empirical tidal heights. In addition, several other hydrodynamic solutions are used for the comparison of volume transports in order to avoid a bias towards HAMTIDE11a.

An algorithm as described in Section 4.2 was implemented in Matlab. As a first validation step, tidal heights from a hydrodynamic assimilation model (HAMTIDE11a) are used to derive barotropic tidal currents. The estimated volume transports are then compared to the volume transports from the assimilation model in order to assess their quality. Figures 4.6 and 4.7 show these comparisons for the K_1 and M_2 tide, respectively. The general pattern of both the amplitudes and the phases agree reasonably well for all tides, the diurnal tides however, slightly worse than semi-diurnal tides. The phases show a better agreement for areas with high amplitudes. Also the amplitudes are better represented when volume transports are higher. The different pattern for diurnal and semi-diurnal tides—diurnal tides have their maxima at higher latitudes—is due to the corresponding equilibrium tide: The largest (degree $n = 2$) diurnal (order $m = 1$) tides have their potential maxima at $\pm 45^\circ$ latitude (cf. Equation 3.11). The M_2 tide, on the other hand, has its maximum of the tidal potential at the equator. This effect can also be seen in the tidal height variation of K_1 and M_2 in Figure 3.4.

There are singularities at latitudes where the inertial frequency equals the tidal frequency (Robertson, 2001). For diurnal tides this critical latitude $\varphi_{\text{crit}} = \arcsin(\omega_{\text{tide}}/(2\Omega)) \approx \pm 30^\circ$, and for semi-diurnal tides $\varphi_{\text{crit}} \approx \pm 75^\circ$. For these latitudes the right hand side of the momentum equations (4.5–4.6) might not vanish and bridging over those areas is necessary (Kantha & Clayson, 2000; Ray *et al.*, 1994). The bridging over critical latitudes is achieved by introducing the continuity equation and a proper weight on it in the inversion algorithm.

High frequency artifacts of HAMTIDE

Although the high weight on the continuity equation largely overcomes the singularities, volume transport bulges occur in open ocean, indicated by small closed contour lines. These arti-

4.3 Inversion Results

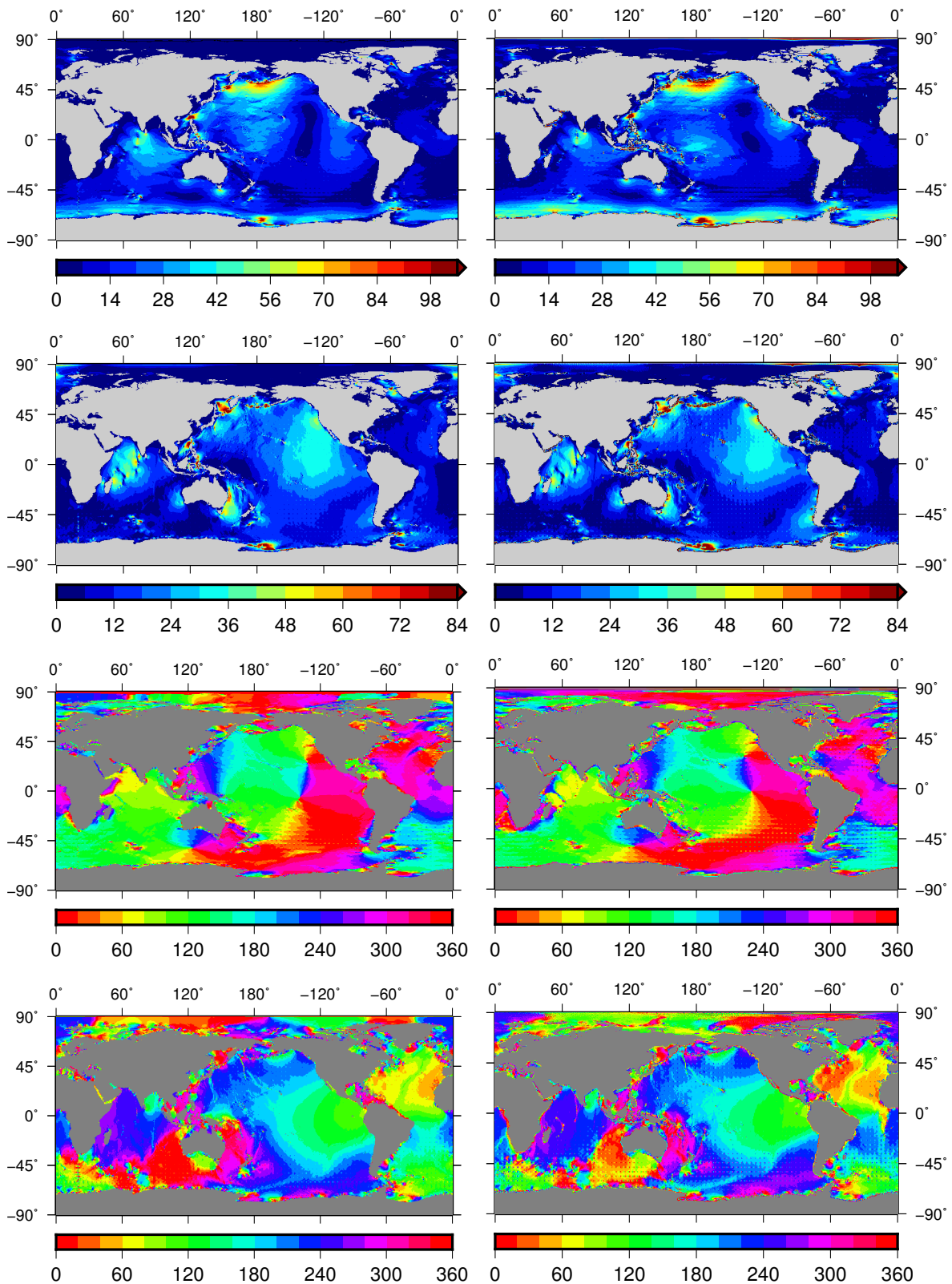


Figure 4.6: Algorithm validation for partial tide K_1 . Right column shows estimated volume transports, left column shows volume transports from the hydrodynamic assimilation model HAMTIDE11a. First and third row show eastward components (U); second and fourth row show northward components (V). Units: m^2/s (amplitudes), degree (phases).

4. Estimation of oceanic currents from measured elevations

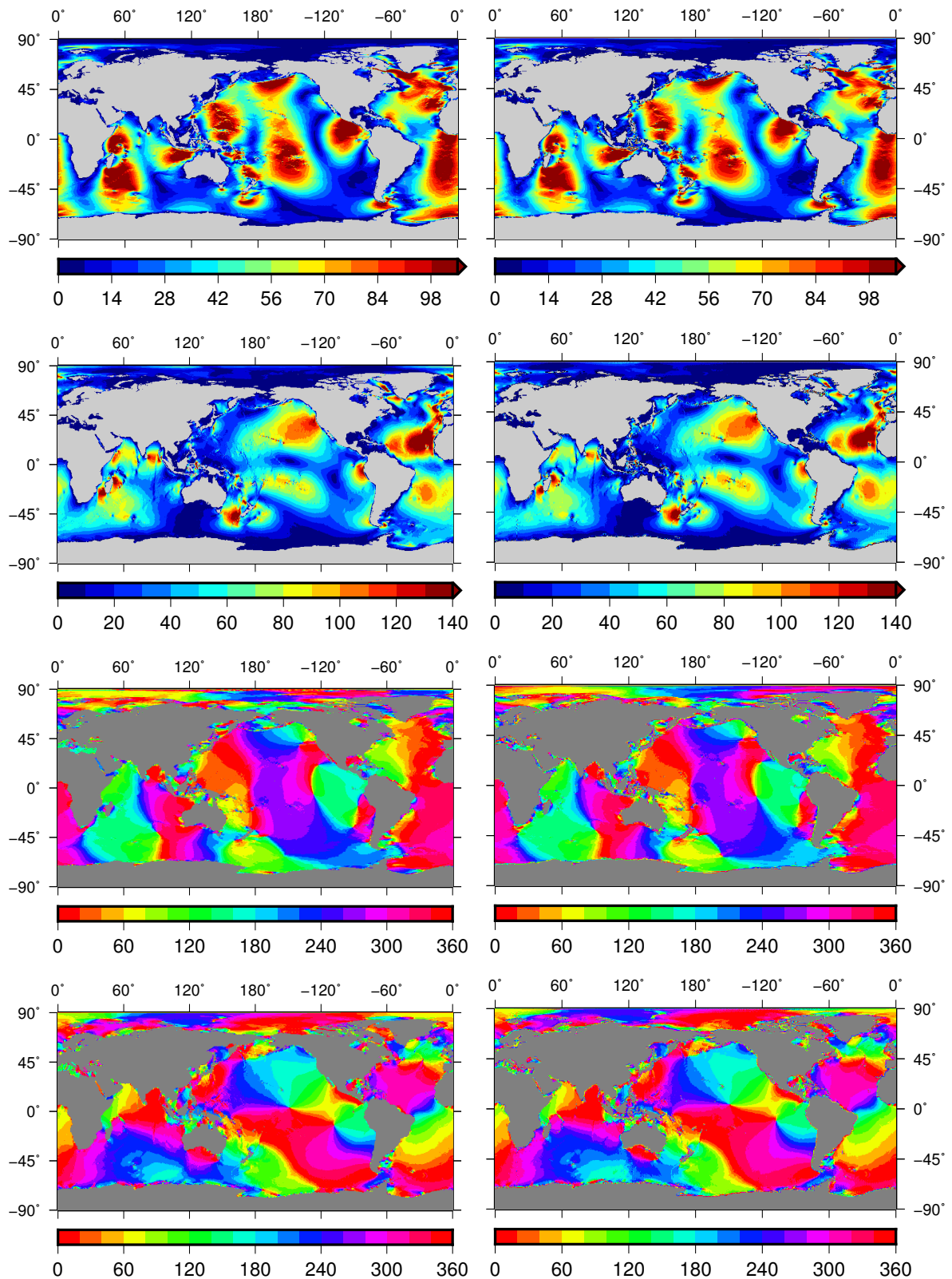


Figure 4.7: Algorithm validation for partial tide M_2 . Right column shows estimated volume transports, left column shows volume transports from the hydrodynamic assimilation model HAMTIDE11a. First and third row show eastward components (U); second and fourth row show northward components (V). Units: m^2/s (amplitudes), degree (phases).

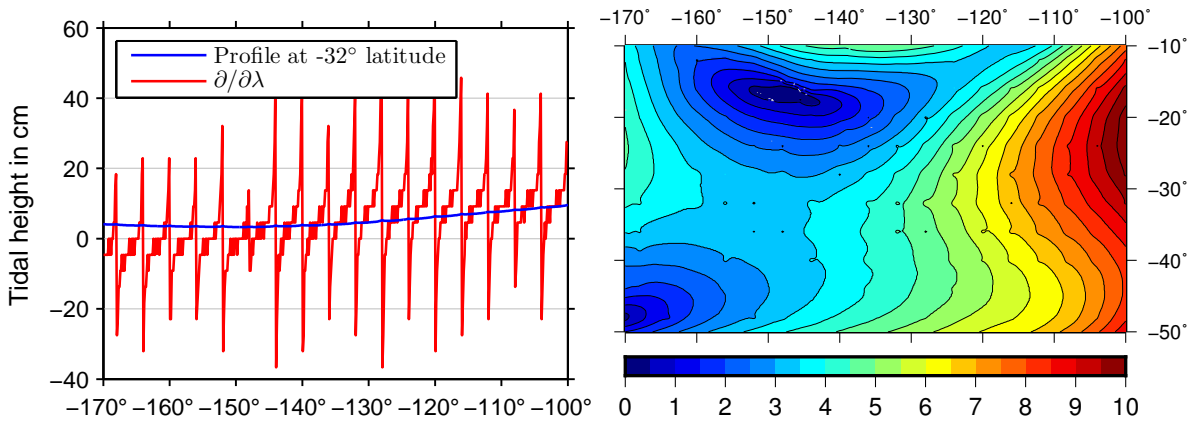


Figure 4.8: Tidal height amplitudes of partial tide K_1 from the hydrodynamic assimilation model HAMTIDE11a in the South Pacific (right). The jittering contour lines are particularly pronounced in those areas. The left image shows an amplitude profile at latitude $\varphi = -32^\circ$ and its derivative with respect to longitude λ .

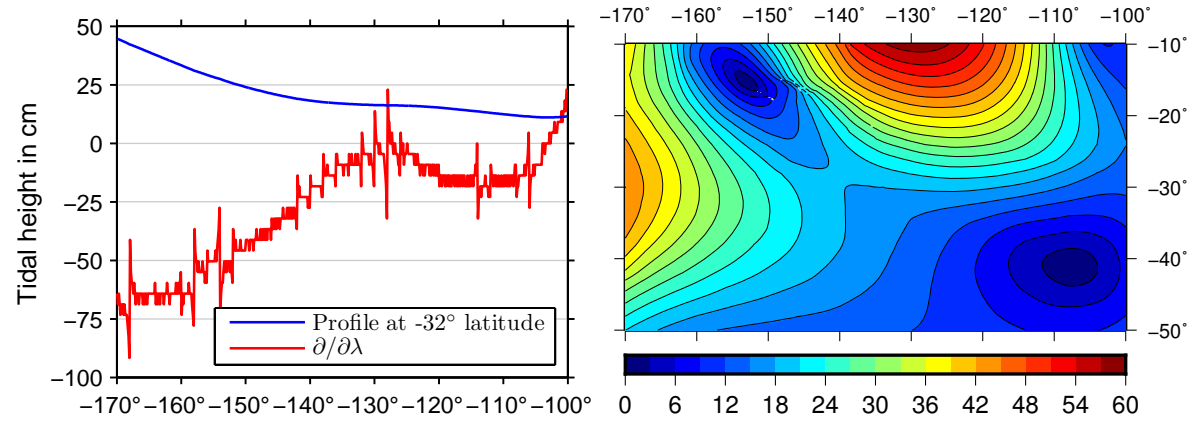


Figure 4.9: Tidal height amplitudes of partial tide M_2 from the hydrodynamic assimilation model HAMTIDE11a in the South Pacific (right). The left image shows an amplitude profile at latitude $\varphi = -32^\circ$ and its derivative with respect to longitude λ .

facts are especially pronounced in the Pacific at higher latitudes for the case of K_1 (cf. Figure 4.6). Moreover, the larger volume transport areas show a noisy behavior, indicated by closed and jittering contour lines. However, both features are apparent in the HAMTIDE volume transports as well and even the tidal heights show an unexpected variation. Since the pattern is regular, the problems might stem from the grid. Figure 4.8 shows amplitudes of the tidal height variation in the south Pacific and a profile at latitude $\varphi = -32^\circ$. The amplitudes slightly decrease between $\lambda = -170^\circ$ and approximately $\lambda = -150^\circ$ and increase again around $\lambda = -140^\circ$. The profile in Figure 4.8 (left) seems to be smooth. The λ -derivative of the profile clearly shows the rapid point alternation which can hardly be explained by physical processes. The latitude profile at $\varphi = -32^\circ$ is close to the “critical” latitude of diurnal tides. Therefore, the same profile was analyzed for partial tide M_2 . It is shown in Figure 4.9. The alternating λ -derivative shows again the non-smoothness of the tidal heights along the profile, the effect, however, seems to be smaller for

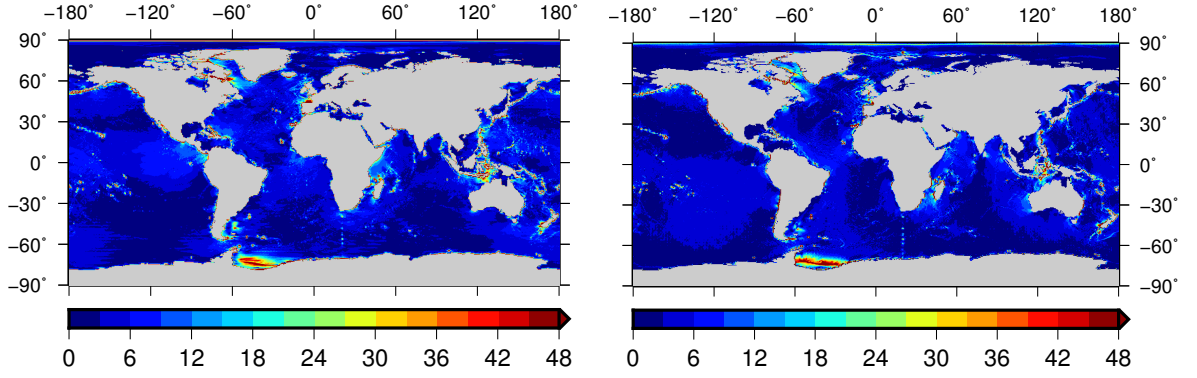


Figure 4.10: RMS of estimated M_2 volume transports (tidal heights for the inversion taken from HAMTIDE11a) and the hydrodynamic HAMTIDE11a solution. Left: Eastward component U , right: Northward component V . Units are m^2/s .

M_2 than for K_1 . That is, the singularity due to the “critical” latitude is not uniquely responsible for the gridding issues.

In any case, these tidal height bulges seem to map into volume transports using the inversion algorithm. However, as already mentioned, also the published version of the hydrodynamic solution suffers from the apparent artifacts.

The Root mean square (RMS) of two harmonic functions with equal frequency, e.g., an estimated sinusoid (superscript t) and a reference model sinusoid (superscript r) for a partial tide j , can be calculated using

$$\text{RMS}_j^{rt} = \sqrt{\frac{(C_j^r - C_j^t)^2 + (S_j^r - S_j^t)^2}{2}}, \quad (4.14)$$

where $S = A \sin \varphi$ and $C = A \cos \varphi$ denote sine- and cosine-amplitudes, respectively. The RMS as defined in Equation (4.14) is equal to the standard deviation of the difference of two harmonic signals with equal frequency and equal to the classical RMS $\sqrt{n^{-1} \sum_i x_i^2}$ if both harmonic signals have the same (or zero) mean amplitude. Relative RMS values are obtained through division by the total amplitude, i.e.,

$$\text{Relative RMS}_j^{rt} = \frac{\text{RMS}_j^{rt}}{\sqrt{(C_j^r)^2 + (S_j^r)^2}}. \quad (4.15)$$

Global maps of relative RMS values may be used to assess the quality of the linearized solution when estimated volume transports are compared to hydrodynamic solutions. Figure 4.10 shows RMS values on a global grid of estimated volume transports and the solution from HAMTIDE11a.

Larger RMS values are found in few areas, mostly close to the coast. A pronounced discrepancy can be seen close to the Antarctic at around $\lambda = -45^\circ$ for both U and V component. There

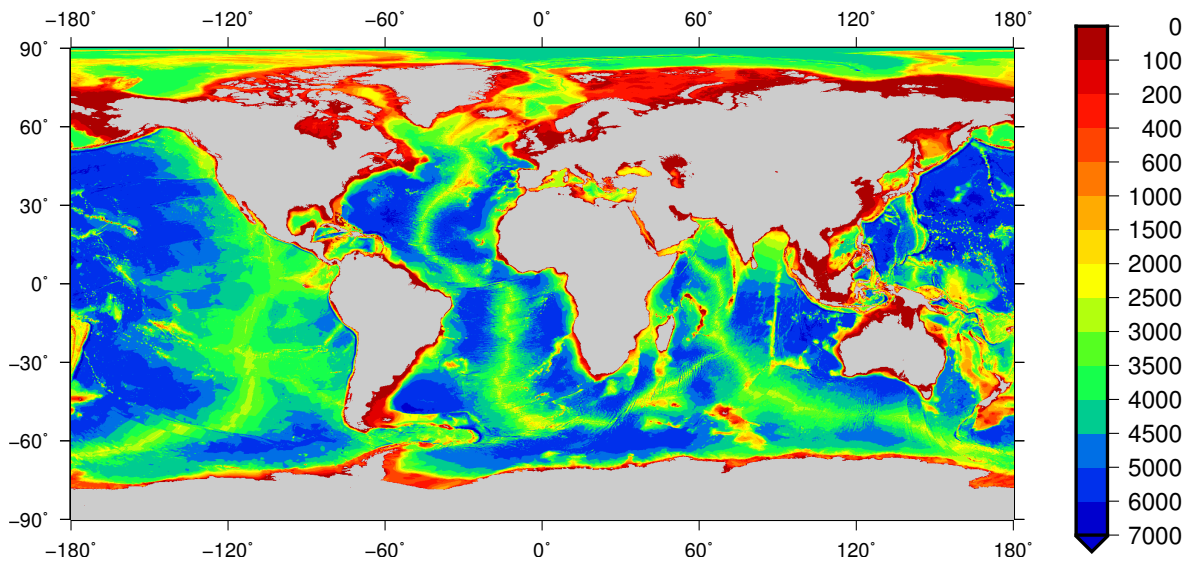


Figure 4.11: Ocean depth in meters from General Bathymetric Chart of the Oceans (GEBCO) data at resolution 0.125° .

is a strong bathymetry gradient and the resampling of the HAMTIDE11a from 0.125° to 0.5° bathymetry might influence estimated currents there as well. Other regions of larger differences can be located within a few grid points off the coast, probably due to the no-flow condition at closed boundaries. The open ocean areas show small RMS values, typically less than $3 \text{ m}^2/\text{s}$. There, the continuity equation “smooths” the volume transports reasonably well to show a good agreement between estimated volume transports and HAMTIDE11a.

Influence of bathymetry

Figure 4.11 shows the General Bathymetric Chart of the Oceans (GEBCO, Gebco gridded global bathymetry data. British Oceanographic Data Centre, Liverpool, United Kingdom, 2009) with a resolution of 0.125° . The original one arc-minute grid was resampled using Gaussian weighting ($\sigma = 0.5$) over a 5×5 arc-minutes area. HAMTIDE11a uses the same bathymetry, although there are significant differences to original GEBCO data, especially around small islands. Figure 4.12 shows differences of three bathymetry datasets, namely HAMTIDE11a (Taguchi, 2014, personal communication), GEBCO, and SRTM (USGS, 2004) data. The latter contains bathymetry data from Smith & Sandwell (1997) between $\pm 81^\circ$, complemented by three higher resolution grids. Higher latitudes data from the International Bathymetric Chart of the Oceans (IBCAO; Jakobsson *et al.*, 2012) were added to get global coverage (Becker *et al.*, 2009).

Bathymetry differences of several hundred meters between GEBCO and SRTM (Figure 4.12, right), even in the open ocean, are apparent. The deviations between the HAMTIDE11a and the GEBCO bathymetries are much smaller in the open ocean, big discrepancies are seen at neighboring grid points of small islands where differences can reach 1000 meters or more. To test the influence of different bathymetries on estimated ocean currents, HAMTIDE11a tidal heights were

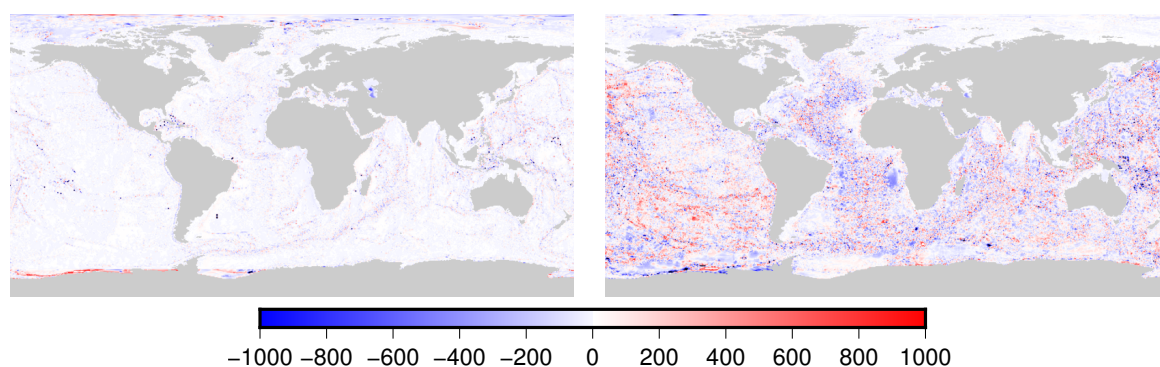


Figure 4.12: Bathymetry differences in meters. Left: HAMTIDE11a–GEBCO, right: GEBCO–SRTM.

inverted to volume transports using (1) HAMTIDE11a bathymetry; (2) GEBCO bathymetry; and (3) SRTM bathymetry. All bathymetries were resampled to 0.5° resolution using Gaussian weighting ($\sigma = 0.5$) over 5×5 nearest points. Figure 4.13 shows RMS values (absolute and relative) of estimated M_2 east volume transports (U) between solutions with use of different bathymetries. North volume transports (V) show similar results with slightly better agreement.

As expected, the GEBCO solution shows a better agreement with HAMTIDE11a as the bathymetry of HAMTIDE11a is based on GEBCO. Still, differences occur mainly at coastal regions or close to small islands. The differences in open ocean are small, probably partly due to the large weight on the continuity equation there. The median RMS for the comparison of HAMTIDE11a and GEBCO is $0.2 \text{ m}^2/\text{s}$, the median relative RMS is 0.7%.

The comparison with SRTM shows larger differences in volume transports, though in similar areas as the GEBCO comparison. However, the differences do extend to the open ocean where relative differences can reach 10% over a wide area, e.g., south of Australia (see Figure 4.13, lower right). This can probably be explained by the non-systematic differences in bathymetry between HAMTIDE11a and SRTM (cf. Figure 4.12). The median RMS when comparing SRTM and HAMTIDE11a is $1.4 \text{ m}^2/\text{s}$, the median relative RMS is 5.0%. An overview of RMS values for all eight tidal constituents is given in Table 4.2. The median RMS values are of similar magnitudes within one species, i.e., diurnal or semi-diurnal. For the comparison of HAMTIDE11a and GEBCO, relative RMS values for diurnals are about two to three times larger than for semi-diurnals. This effect is smaller for the comparison between HAMTIDE11a and SRTM where diurnal tides have around 25% larger values in terms of median relative RMS.

As this study tries to improve tidal ERP predictions, and OTAM is the actual quantity they are derived from, a comparison on the OTAM level is shown in Table 4.3. The components in x , y , and z direction are denoted by h_1 , h_2 , and h_3 . The figures show again clearly the influence of bathymetry on relative momentum variations. The difference in OTAM values reaches up to 20% when SRTM bathymetry is used instead of the HAMTIDE11a bathymetry (which is based

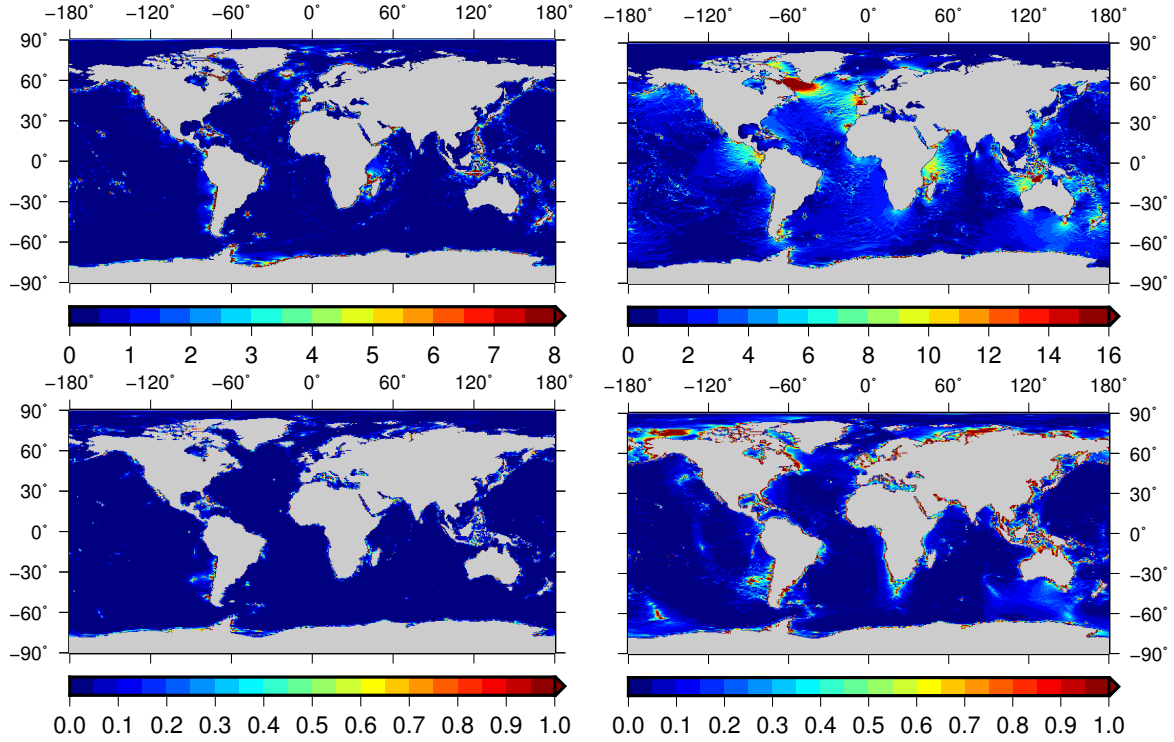


Figure 4.13: RMS values of the comparison of M_2 estimated volume transports using different bathymetry datasets. Upper row: RMS values for eastward volume transport in m^2/s , lower row: relative RMS values for the same component. The reference solution uses the HAMTIDE11a bathymetry, the left column shows the comparison with GEBCO, and the right column shows the comparison with SRTM.

Table 4.2: Median RMS values for the comparison of volume transports using different bathymetry datasets. Absolute values are given in m^2/s , median relative RMS values are given in brackets.

	HAMTIDE11a/GEBCO		HAMTIDE11a/SRTM	
	RMS U	RMS V	RMS U	RMS V
Q_1	0.03 (1.8%)	0.03 (2.3%)	0.08 (6.2%)	0.12 (7.4%)
O_1	0.11 (1.6%)	0.14 (2.1%)	0.39 (5.7%)	0.55 (7.1%)
P_1	0.04 (1.2%)	0.05 (2.0%)	0.17 (5.5%)	0.22 (7.2%)
K_1	0.13 (1.2%)	0.17 (1.9%)	0.55 (5.7%)	0.66 (7.3%)
N_2	0.03 (0.7%)	0.04 (0.7%)	0.29 (5.0%)	0.30 (5.0%)
M_2	0.15 (0.7%)	0.17 (0.7%)	1.36 (5.0%)	1.47 (5.4%)
S_2	0.06 (0.6%)	0.07 (0.8%)	0.57 (4.7%)	0.63 (6.0%)
K_2	0.02 (0.6%)	0.02 (0.8%)	0.16 (4.9%)	0.17 (5.9%)

Table 4.3: Relative RMS values of the OTAM comparison between inversion solutions using different bathymetries. Reference is the inversion using the original HAMTIDE11a bathymetry. Values are given in percent.

Bathymetry	O ₁			K ₁			M ₂			S ₂		
	<i>h</i> ₁	<i>h</i> ₂	<i>h</i> ₃	<i>h</i> ₁	<i>h</i> ₂	<i>h</i> ₃	<i>h</i> ₁	<i>h</i> ₂	<i>h</i> ₃	<i>h</i> ₁	<i>h</i> ₂	<i>h</i> ₃
GEBCO	1.9	1.4	0.6	0.9	0.9	0.6	0.3	0.1	0.5	0.1	0.3	0.5
SRTM	20.4	8.3	1.7	10.9	3.4	1.7	11.1	12.8	5.5	9.9	8.7	1.6

on GEBCO). Even though more than half of the numbers give values well below 10%, the effect of ocean bottom topography is a crucial factor for deriving accurate oceanic currents for the determination of relative angular momentum. As one cannot easily judge one bathymetry as the best (cf. Marks & Smith, 2006), and this study strives for consistency, we use (if available) the same dataset as was used for the input data, i.e. tidal heights.

Influence of tolerance parameter

As the chosen algorithm solves the least-squares system iteratively, a stop criterion is required. For LSQR, a tolerance parameter t is specified comparing the relative residual norm $\|\mathbf{b}-\mathbf{A}\mathbf{x}\|/\|\mathbf{b}\|$ of the current solution with the previous iteration. If it is smaller or equal the tolerance parameter the iterative solver stops. This means that if t is chosen too small, the solution might be improved in further iterations. If t is too large, iterations are carried out without improving the estimated parameters, thereby taking a lot of time or even failing to converge. Ray (2001) uses a tolerance parameter $t = 10^{-5}$. To find a reasonable value for this parameter, several test inversions with $t = [10^{-4}, 10^{-5}, 10^{-6}, 10^{-7}, 10^{-8}, 10^{-9}, 10^{-10}]$ are carried out. The resultant oceanic currents are converted to relative OTAM values and compared to OTAM from the hydrodynamic currents from HAMTIDE11a. The RMS values are shown in Table 4.4 for the major semi-diurnal and diurnal solar and lunar tides. HAMTIDE11a tidal heights as well as the HAMTIDE11a bathymetry are used for the inversion. The continuity equation is weighted by a factor $c = 1000$, the spatial resolution is 0.5° . The values for 10^{-10} show equal numbers as the solution using 10^{-9} as tolerance and are therefore omitted in Table 4.4. Using a tolerance $t < 10^{-9}$ has, thus, hardly any effect on OTAM values. A reasonable accuracy requires around 10^{-7} as all components show an improvement compared to 10^{-6} . Only eight of twelve components improve using a tolerance parameter $t = 10^{-8}$ compared to 10^{-7} . However, for some components of diurnal tides the solution seems to deteriorate the OTAM results when going from $t = 10^{-5}$ to $t = 10^{-6}$. For instance, the h_2 component of O₁ as well as the h_1 and h_2 component of K₁ give smallest RMS values for $t = 10^{-5}$ compared to all other tolerance parameters. On the other hand, the h_3 component clearly improves when t is decreased from 10^{-5} to 10^{-6} . It seems that the improvement in the axial component is at the expense of a deterioration in the equatorial components. For the semi-diurnal constituents, smaller tolerance parameters produce more accurate results (until solutions

Table 4.4: RMS values of OTAM differences derived from the inversion algorithm and HAMTIDE11a. Several tolerance parameters t were used to study the convergence of the algorithm. A weighting factor of $c = 1000$ was used for this comparison. Unit: 10^{24} kg m²/s (please note that this unit is one order of magnitude smaller than for typically published values, it has been chosen for better readability).

t	O ₁			K ₁			M ₂			S ₂		
	h_1	h_2	h_3	h_1	h_2	h_3	h_1	h_2	h_3	h_1	h_2	h_3
10^{-4}	1.32	1.91	3.11	3.70	4.90	4.78	7.63	7.60	10.1	4.11	4.56	4.18
10^{-5}	0.66	0.88	0.30	1.46	1.69	1.00	6.29	4.79	4.13	3.64	2.57	2.50
10^{-6}	0.93	1.45	0.07	2.22	2.22	0.14	1.59	3.33	0.88	1.11	1.51	0.24
10^{-7}	0.78	1.33	0.03	2.11	2.01	0.09	1.46	2.66	0.71	0.97	1.11	0.23
10^{-8}	0.62	1.28	0.04	1.93	1.96	0.12	1.49	2.65	0.67	0.95	1.05	0.23
10^{-9}	0.59	1.26	0.05	1.89	1.94	0.13	1.50	2.64	0.67	0.95	1.05	0.23

converge) throughout all components. For most-accurate inversions, a tolerance parameter of 10^{-9} is required and, thus, used in subsequent calculations.

Relaxing the boundary condition

The largest residuals of estimated volume transports with respect to the hydrodynamic solution (see Figure 4.10) occur, except for the area close to Antarctica, at coastal regions where no-flow boundary conditions are applied. Due to bathymetry inaccuracies (also, a high-resolution bathymetry more accurately describes the true ocean topography) and other modeling errors, the large weight on the continuity equation might lead to unrealistically large volume transports at the coast. McIntosh & Bennett (1984) found that relaxing the rigid boundary condition significantly affects their solution. Hence, for test calculations the continuity equation is experimentally down-weighted at boundary grid points by a factor of 0.1 and 0.01, respectively. The volume transports show hardly any change in open ocean due to relaxed boundary conditions. Significant relative RMS changes above a few percent are mostly within the first two grid points from the coast where the no-flow condition is applied. The resultant effect on OTAM is shown in Table 4.5, which gives relative RMS values compared to the hydrodynamic solution of HAMTIDE11a. When a relax factor of 0.1 is applied on the continuity equation at the coast, the OTAM values are up to 1% closer to the reference (HAMTIDE11a). This improvement is found to be true for basically all tides and components. Decreasing the relax factor further to 0.01 results in an increase in RMS values and, thus, does not lead to more accurate estimates. Differences in components (h_1 , h_2 , h_3) and in species (diurnal, semi-diurnal) are obvious in Table 4.5. The axial component of angular momentum is far more accurately determined: Six of eight tides agree within 5%, only the smaller constituents N₂ (maximum 11.9%) and K₂ (maximum 6.2%) have larger differences. Diurnal tides in the equatorial components show OTAM values which are 10 to 20 percentage

Table 4.5: Comparison of relaxing factors for the no-flow condition at closed boundaries. Shown are relative RMS values of OTAM as computed from different inversion solutions. Reference OTAM is HAMTIDE11a. Values are given in percent.

Relax factor	O ₁			K ₁			M ₂			S ₂		
	<i>h</i> ₁	<i>h</i> ₂	<i>h</i> ₃	<i>h</i> ₁	<i>h</i> ₂	<i>h</i> ₃	<i>h</i> ₁	<i>h</i> ₂	<i>h</i> ₃	<i>h</i> ₁	<i>h</i> ₂	<i>h</i> ₃
No relax	21.7	29.8	0.9	33.5	24.9	1.8	14.0	15.3	4.5	17.7	11.2	3.1
0.1	20.6	29.2	0.9	32.9	24.8	1.8	13.0	14.3	4.0	16.7	10.6	2.9
0.01	21.7	29.8	0.9	33.5	24.9	1.8	13.9	15.2	4.5	17.5	11.2	3.1

points worse compared to semi-diurnals.

Weighting

As the unknown parameters in Equations (4.5)–(4.7) are volume transports instead of currents, the only dynamical errors in the continuity equation (4.7) stem from neglecting non-linear terms and from the measurement errors of the tidal heights ζ . Elevation errors in recent ocean tide models are well below the centimeter level in the open ocean (Stammer *et al.*, 2014) and the residuals should be of the same magnitude. The momentum equations (4.5–4.6), on the other hand, contain most of the errors of the dynamic system. Those errors stem from the mismodeling of dissipative terms (Equation 4.3) and errors in the bathymetry (Ray, 2001).

Therefore, the continuity equation must be weighted far more heavily than the momentum equations. Ray (2001) finds a proper scaling factor $c = 1000$ m/s. Several weighting factors are tested and the effect on relative OTAM for several ocean current solutions is calculated. The reference is again OTAM from the hydrodynamic solution HAMTIDE11a. The RMS values of the respective solution and the reference solution is shown in Table 4.6. The weights showing the smallest RMS values depend both on the harmonic constituent and on the OTAM component. The differences in weights giving the best agreement are large, as will be shown in the following. It, thus, stands to reason to adapt the weight per constituent and component to derive accurate oceanic currents for the motion term contributions to ERP variations.

For the case of purely lunar semi-diurnal tides (N₂ and M₂) a weight of around 600 gives reasonably small RMS values for all components (*h*₁, *h*₂, and *h*₃). The *h*₂ component for M₂ shows a better agreement with the hydrodynamic solution HAMTIDE11a using a weight of 200. However, the resultant RMS differs only by a few percent when changing weights from 600 to 200. Figures are different for the purely solar semi-diurnal tide S₂. The equatorial components *h*₁ and *h*₂ show the best agreement with HAMTIDE11a for weight 200. The *h*₃ component can be significantly improved when weights are larger: we find the smallest RMS of $0.05 \cdot 10^{24}$ kg m²/s for weight 1500. The corresponding OTAM value differs from the HAMTIDE11a OTAM value by 0.6% (relative RMS). A similar behavior is found for the semi-diurnal luni-solar tide K₂ (not shown), however with larger weights in both the equatorial (400) and the axial (2000) components.

Table 4.6: Influence of weighting of the continuity equation on inverted barotropic currents. Values denote RMS of relative OTAM with respect to the hydrodynamic solution of HAMTIDE11a. The smallest RMS value for each component is highlighted.

Weight	O ₁			K ₁			M ₂			S ₂		
	<i>h</i> ₁	<i>h</i> ₂	<i>h</i> ₃	<i>h</i> ₁	<i>h</i> ₂	<i>h</i> ₃	<i>h</i> ₁	<i>h</i> ₂	<i>h</i> ₃	<i>h</i> ₁	<i>h</i> ₂	<i>h</i> ₃
1	8.39	5.13	0.69	19.0	20.3	2.62	3.47	4.93	5.36	0.72	1.09	1.17
100	3.45	3.69	0.41	9.84	12.52	0.64	2.06	2.19	3.30	0.34	0.64	0.89
200	2.01	2.65	0.20	6.43	8.26	0.57	1.79	1.73	2.38	0.34	0.61	0.78
400	1.10	1.86	0.09	3.80	4.66	0.26	1.53	2.01	1.11	0.46	0.68	0.64
600	0.81	1.56	0.07	2.77	3.19	0.08	1.39	2.24	0.33	0.63	0.81	0.50
800	0.67	1.38	0.05	2.22	2.42	0.06	1.39	2.44	0.26	0.81	0.93	0.36
1000	0.62	1.28	0.04	1.93	1.96	0.12	1.49	2.65	0.67	0.95	1.05	0.23
1200	0.53	1.15	0.08	1.66	1.61	0.19	1.66	2.85	1.01	1.08	1.15	0.12
1500	0.48	1.04	0.14	1.45	1.27	0.28	1.88	3.14	1.40	1.22	1.29	0.05
2000	0.42	0.92	0.22	1.23	0.95	0.39	2.18	3.56	1.87	1.39	1.47	0.21
2500	0.38	0.84	0.28	1.12	0.77	0.48	2.36	3.88	2.19	1.49	1.60	0.33
3000	0.36	0.79	0.31	1.05	0.67	0.53	2.46	4.12	2.41	1.55	1.70	0.42
4000	0.34	0.74	0.35	0.97	0.58	0.60	2.60	4.43	2.68	1.62	1.83	0.54
5000	0.33	0.71	0.38	0.94	0.54	0.63	2.66	4.61	2.83	1.65	1.91	0.59
6000	0.33	0.70	0.39	0.92	0.51	0.65	2.69	4.72	2.92	1.67	1.96	0.64
7000	0.31	0.68	0.39	0.90	0.50	0.67	2.72	4.79	2.98	1.69	1.98	0.66
8000	0.32	0.68	0.40	0.89	0.49	0.67	2.73	4.83	3.01	1.69	2.01	0.68
9000	0.31	0.67	0.40	0.89	0.48	0.68	2.75	4.87	3.04	1.70	2.02	0.68
10000	0.31	0.67	0.41	0.87	0.48	0.68	2.75	4.89	3.06	1.70	2.03	0.70

Table 4.7: Proper weights for the continuity equation in the least-squares adjustment from the “calibration” experiments when deriving oceanic currents from HAMTIDE11a tidal elevations using shallow water equations.

Type	Example	Weight for h_1, h_2	Weight for h_3
Diurnal lunar	O_1, Q_1	10000	1000
Diurnal solar	P_1	10000	600
Diurnal luni-solar	K_1	10000	800
Semi-diurnal lunar	M_2, N_2	600	600
Semi-diurnal solar	S_2	200	1500
Semi-diurnal luni-solar	K_2	400	2000

The values for the diurnal tides show a clearly different behavior. In particular for equatorial components, the continuity equation requires a much larger weight to obtain the best agreement with the hydrodynamic solution of HAMTIDE11a. For all diurnal constituents available in HAMTIDE11a (O_1 , Q_1 , P_1 , and K_1) weights above 7000 yield similar results for the equatorial components h_1 and h_2 . The values show hardly any change when increasing the weight from 9000 to 10000. However, the apparently optimal weight is 10000 for the equatorial components of diurnal tides. For the axial OTAM, similar weights are found as for semi-diurnal tides: Diurnal lunar tides (O_1 and Q_1) show smallest RMS values for a weight of 1000, the diurnal solar tide P_1 requires a smaller weight of 600 to yield the best agreement to OTAM from HAMTIDE11a. The luni-solar tide K_1 lies in between with a recommended weight of 800. The recommended weights for the tidal constituents per component are summarized in Table 4.7. There should be noted, however, that the use of different weights per tide and component introduces an inconsistency. The relative OTAM values are derived from different volume transport solutions and combined “arbitrarily”. That means that two solutions of oceanic flows are used to derive the OTAM components of one tide.

Chapter 5

New Earth rotation corrections based on empirical ocean tide models

In this chapter we apply the findings from the previous section in order to estimate new Earth rotation corrections. As this work seeks to use empirical ocean tide models for ERP corrections, oceanic currents from the tidal model EOT11a (Savcenko & Bosch, 2012) are derived using the algorithm described in Chapter 4. This empirical ocean tide model is developed at DGFI in Munich and used for reprocessing gravity data from the satellite mission GRACE (Bosch *et al.*, 2009). To estimate ocean currents from EOT11a, the first algorithm parameters are taken according to the findings in Section 4.3. Solutions with weights mentioned in Table 4.7 are calculated to examine if the weights have a similar impact when using EOT11a instead of HAMTIDE11a. Figure 5.1 shows a comparison of OTAM differences. Data points show relative RMS values of OTAM (motion term) with respect to the reference model TPXO7.2, another recent assimilation model mentioned in Stammer *et al.* (2014). Some solutions are omitted for better readability. In this validation section additional hydrodynamic models are employed for comparing estimated volume transports. This allows a more generalized view on the results and avoids a bias towards HAMTIDE11a.

As expected, the weights have a similar effect on the solution as for the ocean tide model HAMTIDE11a (see Section 4.3). For example, the algorithm requires a large weight for the equatorial components (h_1 and h_2) of diurnal tides. However, this constraint seems to be too tight for semi-diurnal tides and for the polar component in both tidal frequency bands. The diurnal h_3 component shows smallest RMS values for weights between 400 and 1000 in the comparison with hydrodynamic assimilation tidal models. Also the semi-diurnal tides show similar characteristics as in the HAMTIDE11a calibration, whose values are shown in Table 4.7. The equatorial components require a weight of around 200 for all semi-diurnal tides, which is even smaller than for the calibration. The polar component h_3 again shows the best agreement to hydrodynamic solutions with weights between 400 and 1500.

The assimilation solutions TPXO7.2, HAMTIDE11a, and FES2012 mutually agree in general better than the inversion algorithm at a level of about $< 10\%$. However, this was expected as “full” modeling includes a more realistic hydrodynamic behavior of a flow. Nevertheless, the

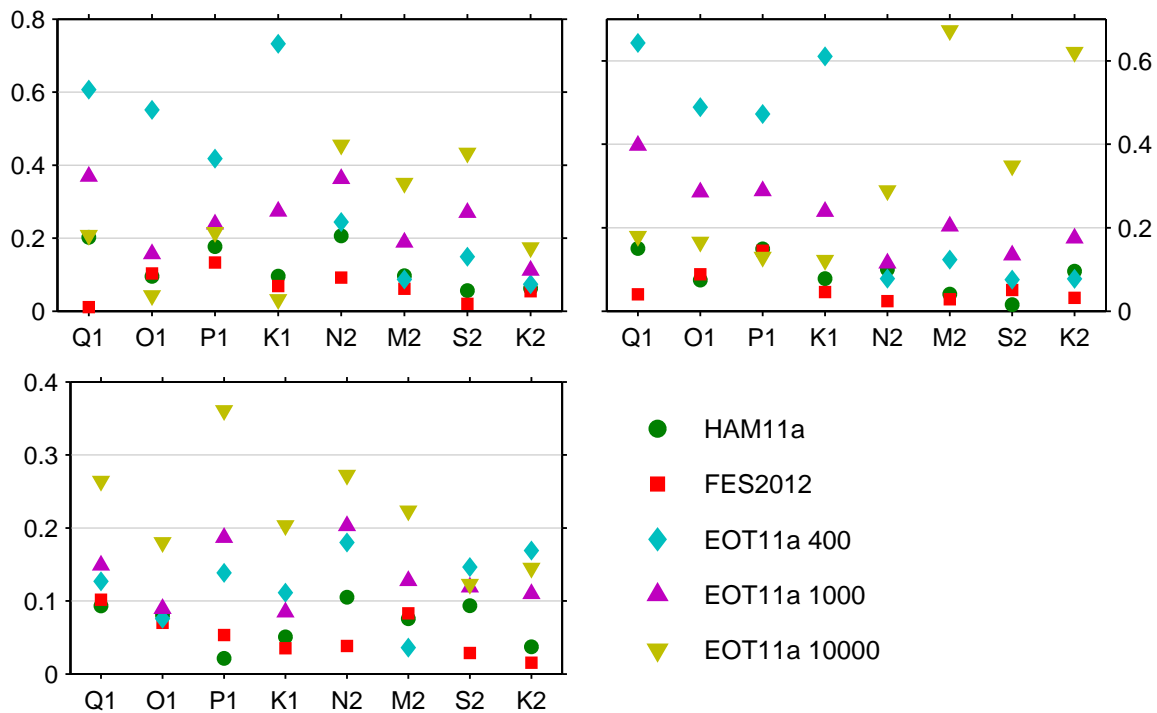


Figure 5.1: Relative RMS values of OTAM (motion term only, dimensionless) from oceanic currents. Reference model is TPXO7.2. The weights for the inversion of EOT11a tidal heights are given in the legend. HAM11a is HAMTIDE11a. The three figures denote (clockwise) x -, y -, and z -components.

intermediate approach used in this work gives reasonable results and the relative OTAM agrees to at least one hydrodynamic solution within a few percentage points.

The best agreement for EOT11a with OTAM from hydrodynamic solutions are given at slightly different weights than for the “calibration” results from Section 4.3. These recommended weights are given in Table 5.1. The weights appear to be smaller and more homogeneous than those from HAMTIDE11a. For example, three of the four major semi-diurnal tides show the smallest OTAM RMS in the equatorial components for a weight of 200. The S_2 equatorial component shows slightly smaller RMS values using an even smaller weight of 100. The comparison for HAMTIDE11a (see Table 4.7) showed the best agreement for weights between 200 and 600. The smaller weight could be due to the apparent gridding feature, which was shown in Figure 4.8. The gridpoints close to those features might require a larger weight on the continuity equation to derive smoother volume transports.

Oceanic currents from the empirical ocean tide model EOT11a were calculated using the algorithm described in Chapter 4 with the weights from Table 5.1. As the empirically derived EOT11a does not use any bathymetry data, the GEBCO bathymetry (1-minute grid downsampled using Gaussian weighting) was used in the inversion process. The tolerance parameter was set

Table 5.1: Applied weights for the continuity equation in the least-squares adjustment when deriving relative OTAM from oceanic currents from the empirical ocean tide model EOT11a using shallow water equations.

Type	Example	Weight for h_1, h_2	Weight for h_3
Diurnal lunar	O_1, Q_1	10000	600
Diurnal solar	P_1	10000	400
Diurnal luni-solar	K_1	10000	800
Semi-diurnal lunar	M_2, N_2	200	400
Semi-diurnal solar	S_2	100	2000
Semi-diurnal luni-solar	K_2	200	1000

to $t = 10^{-9}$. The no-flow condition at closed boundaries was relaxed by a factor of 0.1. Global maps showing estimated volume transports are shown in Figures 5.2 and 5.3. The former shows partial tides O_1 and K_1 , the latter shows tides M_2 and S_2 .

The diurnal tides show very noisy volume transports in spite of the large weight on the continuity constraint of 10000. This is, again, likely due to the high-frequency oscillation pattern of the tidal heights as mentioned before and shown in Figures 4.8 and 4.9 for HAMTIDE11a, which occurs, however smaller, also in EOT11a. These artifacts might be one of the reasons why diurnal tides require a much larger weight on the continuity equation to derive accurate volume transports. However, a strong smoothing of tidal heights has not been applied because the mass term of OTAM should be based as much as possible on the original empirical solution of EOT11a and small scale noise in volume transports cancel due to integration when calculating angular momentum. The global patterns can be well recognized in a comparison with the assimilation model FES2012. The main differences occur in small areas of large velocity and topography gradients, such as in the Weddell Sea south-east of Argentina or in the Arctic ocean north of Alaska. The derived volume transports from EOT11a in these areas are smaller than volume transports from FES2012, possibly due to the continuity constraint.

The volume transports of semi-diurnal tides show a very good agreement in comparison with FES2012. Both amplitudes and phases have the same global pattern, the EOT11a solution is (again) slightly noisier than the assimilation model. However, the noise level is clearly smaller for semi-diurnal tides than for diurnal constituents.

The resultant OTAM for the four diurnal tides ($Q_1, O_1, P_1,$ and K_1) and five semi-diurnal tides ($2N_2, N_2, M_2, S_2,$ and K_2) from EOT11a are given in Table 5.2. For comparison on the OTAM level, Tables 5.3 and 5.4 show angular momentum values derived from the assimilation models HAMTIDE11a and FES2012. $H_1, H_2,$ and H_3 denote $x, y,$ and z components of the mass term of ocean tidal angular momentum, lowercase letters those of the motion term. In general, the OTAM motion terms of the assimilation models mutually agree slightly better than with those from EOT11a. However, even between the assimilation models, differences can be well above

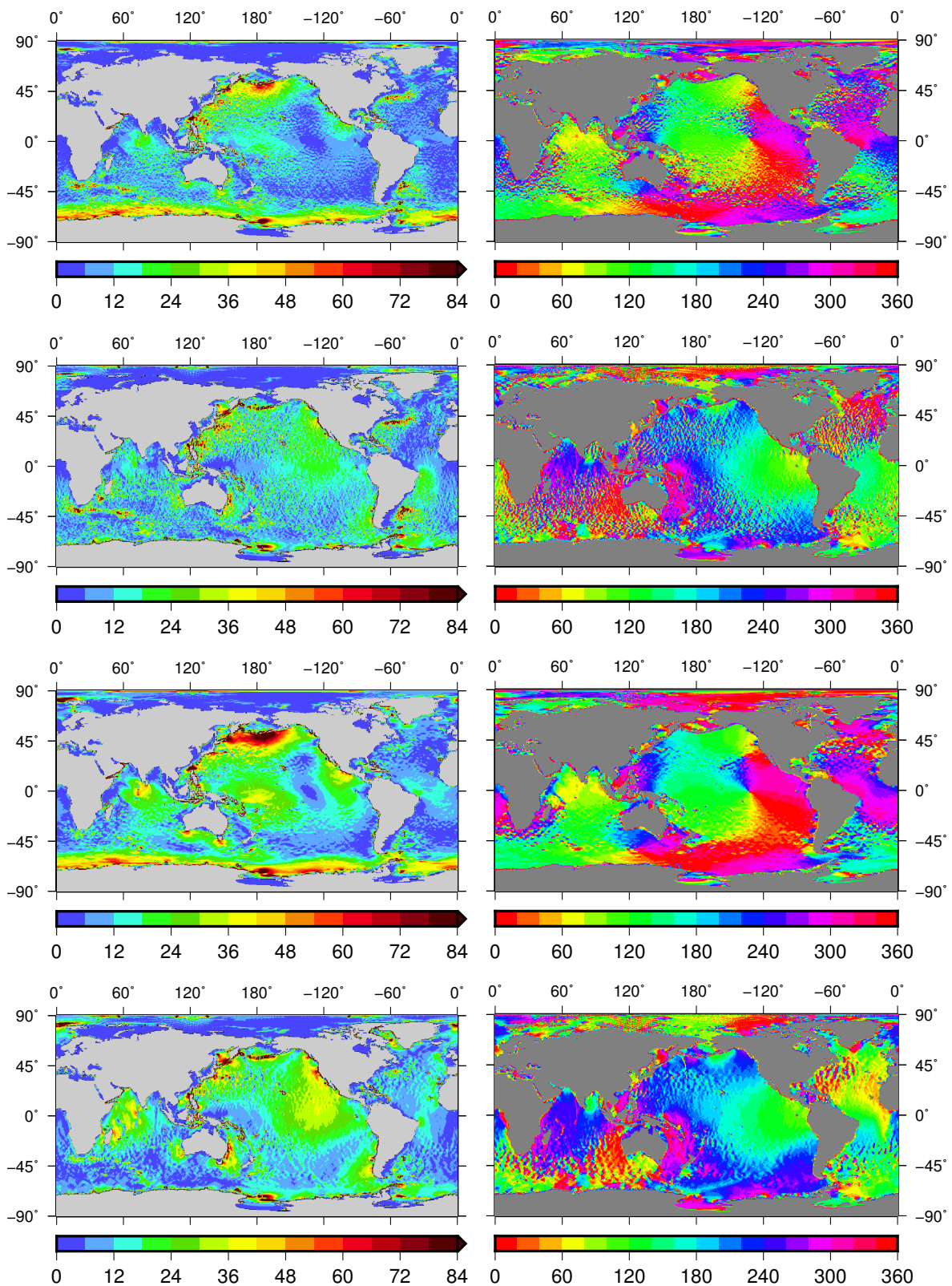


Figure 5.2: Volume transports of diurnal tides O_1 (two upper rows; east/north direction) and K_1 (two lower rows) from the inversion algorithm based on tidal heights from EOT11a. Left column: Amplitudes in m^2/s . Right: Phases in degrees. Weights for the continuity equation were applied according to Table 5.1 (shown are the solutions using the “equatorial” weights).

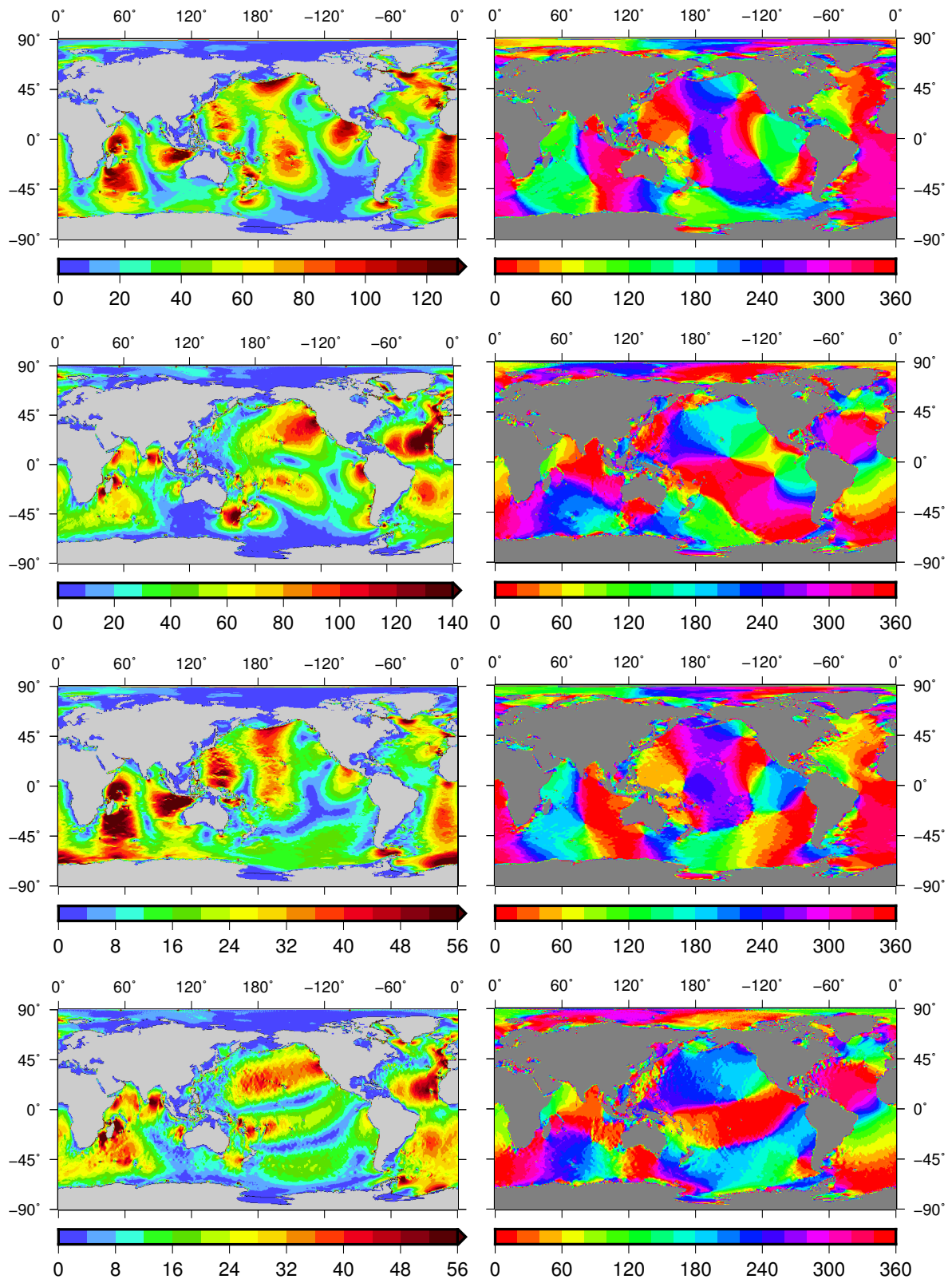


Figure 5.3: Volume transports of semi-diurnal tides M_2 (two upper rows; east/north direction) and S_2 (two lower rows) from the inversion algorithm based on tidal heights from EOT11a. Left column: Amplitudes in m^2/s . Right: Phases in degrees. Weights for the continuity equation were applied according to Table 5.1 (shown are the solutions using the “equatorial” weights).

Table 5.2: OTAM derived from the empirical ocean tide model EOT11a. The oceanic currents for the motion term were calculated using the algorithm described in Chapter 4 with weights according to Table 5.1. The spatial resolution for the mass term is 0.125° and 0.5° for the motion term. Amplitudes in 10^{25} kg m²/s, phases in degrees.

Tide	Type	x		y		z	
		Amp	Pha	Amp	Pha	Amp	Pha
Q ₁	Mass term	0.115	338.7	0.259	215.5	0.066	137.5
	Motion term	0.069	291.4	0.090	206.8	0.118	107.9
	Total	0.170	321.3	0.348	213.3	0.178	118.4
O ₁	Mass term	0.480	329.4	1.173	222.2	0.167	171.2
	Motion term	0.269	304.3	0.494	202.3	0.549	119.4
	Total	0.733	320.4	1.646	216.3	0.665	130.8
P ₁	Mass term	0.154	315.9	0.451	223.0	0.044	20.0
	Motion term	0.212	290.0	0.252	196.6	0.201	131.0
	Total	0.357	300.9	0.686	213.6	0.190	118.5
K ₁	Mass term	0.450	308.4	1.372	223.6	0.186	20.1
	Motion term	0.527	285.7	0.875	195.5	0.701	132.6
	Total	0.958	296.1	2.183	212.7	0.653	117.3
2N ₂	Mass term	0.020	321.0	0.003	125.8	0.012	154.8
	Motion term	0.011	233.2	0.029	174.2	0.054	321.9
	Total	0.023	292.7	0.031	170.1	0.042	318.3
N ₂	Mass term	0.125	347.1	0.034	237.9	0.042	65.4
	Motion term	0.156	240.4	0.229	162.4	0.288	315.1
	Total	0.170	285.3	0.240	170.3	0.276	323.3
M ₂	Mass term	0.506	9.4	0.351	305.7	0.602	84.7
	Motion term	0.901	260.4	1.573	166.7	1.567	319.2
	Total	0.878	293.4	1.328	176.7	1.312	341.1
S ₂	Mass term	0.115	41.9	0.284	9.9	0.214	131.7
	Motion term	0.541	293.8	0.933	198.8	0.832	341.0
	Total	0.517	306.0	0.654	202.7	0.654	350.2
K ₂	Mass term	0.033	49.5	0.084	12.1	0.080	102.2
	Motion term	0.145	295.4	0.267	196.7	0.212	335.7
	Total	0.135	308.3	0.183	198.8	0.177	357.1

Table 5.3: OTAM from the assimilation model HAMTIDE11a. Amplitudes in 10^{25} kg m²/s, phases in degrees.

Tide	Mass terms (heights)						Motion terms (currents)					
	H_1		H_2		H_3		h_1		h_2		h_3	
	Amp	Pha	Amp	Pha	Amp	Pha	Amp	Pha	Amp	Pha	Amp	Pha
Q_1	0.104	336.9	0.246	213.9	0.064	109.1	0.055	292.3	0.066	204.3	0.122	110.5
O_1	0.471	329.5	1.154	221.7	0.225	154.3	0.286	300.0	0.431	205.4	0.546	119.1
P_1	0.185	320.7	0.456	225.9	0.035	35.0	0.185	294.1	0.263	196.2	0.244	128.4
K_1	0.425	306.6	1.339	223.3	0.151	34.8	0.574	284.1	0.783	188.0	0.722	130.9
N_2	0.126	350.3	0.034	232.1	0.047	79.7	0.178	245.6	0.274	156.6	0.331	325.3
M_2	0.511	10.5	0.346	306.0	0.600	84.6	1.151	258.8	1.850	165.8	1.699	318.6
S_2	0.120	39.6	0.289	9.3	0.252	125.1	0.569	295.7	0.988	201.2	0.778	340.7
K_2	0.029	32.5	0.081	10.8	0.065	136.6	0.153	298.5	0.270	204.3	0.216	343.5

10%. The biggest difference is found for the x -component of partial tide N_2 , where the relative RMS is 36.2% between FES2012 and HAMTIDE11a. Also the diurnal Q_1 differs by 18.9%, 17.1%, and 15.9% for x -, y -, and z -component, respectively. Still, the majority of components between FES2012 and HAMTIDE11a agree within 10% relative RMS.

The comparison with OTAM from the empirical ocean tide model EOT11a shows slightly larger deviations from the assimilation models compared to their mutual agreement. Again, the majority of components agree better than 10% (relative RMS) with a maximum of 31.9% (x -component for partial tide N_2) with respect to FES2012. The mean relative RMS values over three components x , y , and z are summarized in Table 5.5.

Figure 5.4 shows phasor diagrams of OTAM values from four ocean tide models. The motion terms for model EOT11a are derived from tidal currents from the inversion algorithm using weights according to Table 5.1. Mass terms typically agree better than motion terms, likely due to the variety of input data sets and estimation parameters in the hydrodynamic solution.

The OTAM values from EOT11a are converted to ERP variations using equations described in Section 3.7. The correction values for polar motion and UT1–UTC are given in Tables 5.6 and 5.7, respectively. A graphical representation of ERP variations from several models is shown in Figure 5.5. Prograde and retrograde polar motion coefficients as well as cosine- and sine-amplitudes for Δ UT1 are plotted for eight major tides.

5.1 Minor tides and admittance

Several modern ocean tide models include more than only the eight major tides. For example, the FES2012 (Carrère *et al.*, 2012), a hydrodynamic assimilation model, includes 32 tidal constituents, six of them being long-term tides. However, empirical solutions and other assimilation models still consist basically of eight major tides. The two empirical models in a recent com-

Table 5.4: OTAM from the assimilation model FES2012 (selected tidal constituents). Amplitudes in 10^{25} kg m²/s, phases in degrees.

Tide	Mass terms (heights)						Motion terms (currents)					
	H_1		H_2		H_3		h_1		h_2		h_3	
	Amp	Pha	Amp	Pha	Amp	Pha	Amp	Pha	Amp	Pha	Amp	Pha
Z_0	0.011		0.006		0.510		0.002		0.001		0.006	
S_{sa}	0.008	63.9	0.004	235.3	0.342	29.2	0.003	271.6	0.002	272.3	0.004	29.8
Q_1	0.116	340.4	0.264	215.4	0.072	129.3	0.058	307.8	0.075	217.1	0.151	103.1
O_1	0.476	330.1	1.178	221.9	0.180	171.1	0.291	299.7	0.442	206.1	0.651	115.1
P_1	0.169	310.6	0.450	223.2	0.069	347.6	0.183	287.4	0.255	192.8	0.257	128.4
K_1	0.462	308.3	1.377	224.2	0.187	1.9	0.557	288.8	0.774	192.1	0.804	128.3
J_1	0.026	294.0	0.076	228.8	0.014	42.5	0.036	292.0	0.055	186.7	0.046	141.3
$2N_2$	0.021	312.9	0.004	120.7	0.004	151.0	0.014	277.6	0.036	168.0	0.057	324.4
μ_2	0.014	316.6	0.007	100.1	0.027	89.6	0.015	263.5	0.039	164.0	0.046	327.5
N_2	0.122	346.9	0.031	229.8	0.049	68.4	0.126	260.2	0.245	160.7	0.276	328.2
ν_2	0.020	347.6	0.007	254.0	0.017	46.7	0.029	250.1	0.051	156.4	0.048	322.5
M_2	0.510	10.1	0.361	305.7	0.602	84.4	0.962	259.7	1.812	166.1	1.523	315.2
S_2	0.106	39.1	0.278	8.5	0.249	129.1	0.560	299.5	0.969	198.2	0.798	347.3
K_2	0.031	35.3	0.082	11.9	0.045	128.9	0.174	292.4	0.275	194.9	0.224	342.5

 Table 5.5: Relative RMS values of OTAM motion terms. Values denote mean values over x , y , and z) with respect to a reference model as given in the table. Model EOT11a denotes motion term values as given in Table 5.2.

	Q_1	O_1	P_1	K_1	N_2	M_2	S_2	K_2
	w.r.t. FES2012							
EOT11a	20.6%	9.8%	10.7%	8.6%	17.9%	6.4%	6.2%	8.1%
HAMTIDE11a	17.3%	5.2%	5.6%	6.4%	20.2%	8.3%	5.7%	8.5%
	w.r.t. EOT11a							
FES2012	19.7%	10.4%	11.6%	8.8%	15.7%	7.0%	6.2%	9.1%
HAMTIDE11a	12.5%	5.8%	9.6%	7.0%	15.1%	12.8%	4.7%	8.3%

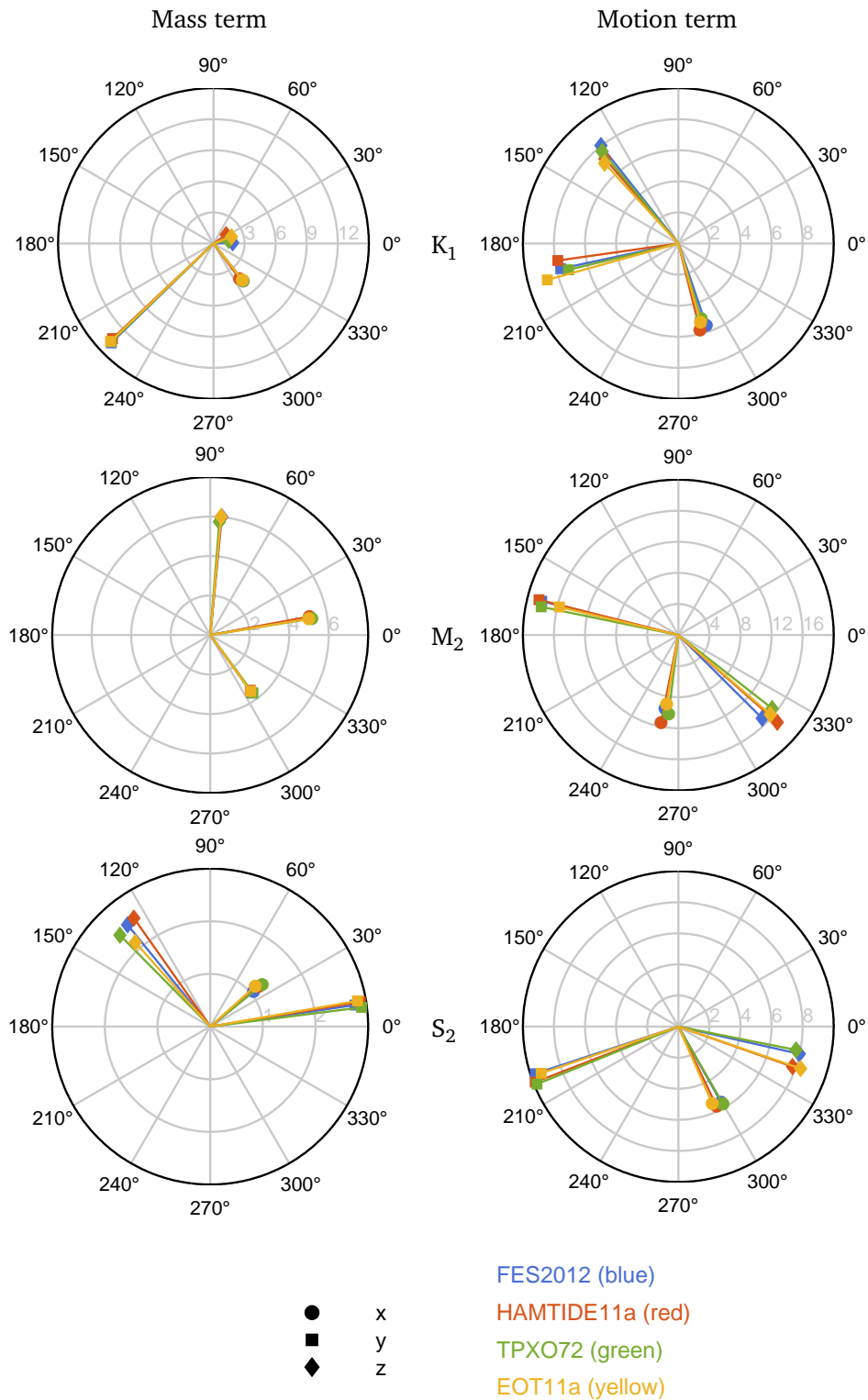


Figure 5.4: Phasor diagrams of OTAM from ocean tide models FES2012 (blue), HAMTIDE11a (red), TPXO7.2 (green), and EOT11a (yellow, weights for the inversion according to Table 5.1). Shown are values of partial tides K_1 (first row), M_2 (second row), and S_2 (third row). Circles denote x-components, squares y-components, and diamonds z-components of OTAM, respectively. Amplitudes in $10^{24} \text{ kg m}^2/\text{s}$, phases in degrees.

Table 5.6: Polar motion variation coefficients for nine major tides based on EOT11a. Oceanic currents for the calculation of relative OTAM are derived from EOT11a surface elevation data using the inversion algorithm described in Chapter 4. The parametrization for the inversion process is specified in Chapter 5.

Tide	Delaunay arguments						Doodson number	Period (hours)	X_s (μas)	X_c (μas)	Y_s (μas)	Y_c (μas)
	γ	l	l'	F	D	Ω						
Q_1	1	-1	0	-2	0	-2	135.655	26.8684	10.3	30.5	-30.5	10.3
O_1	1	0	0	-2	0	-2	145.555	25.8193	65.1	146.1	-146.1	65.1
P_1	1	0	0	-2	2	-2	163.555	24.0659	28.1	40.3	-40.3	28.1
K_1	1	0	0	0	0	0	165.555	23.9345	-113.0	-158.0	158.0	-113.0
$2N_2$	2	-2	0	-2	0	-2	235.755	12.9054	-6.6	-0.9	1.1	4.0
N_2	2	-1	0	-2	0	-2	245.655	12.6583	-49.0	-8.7	3.9	33.2
M_2	2	0	0	-2	0	-2	255.555	12.4206	-282.1	-24.6	51.1	167.8
S_2	2	0	0	-2	2	-2	273.555	12.0000	-132.3	53.1	56.1	84.3
K_2	2	0	0	0	0	0	275.555	11.9672	-38.0	12.7	15.5	21.4

Table 5.7: ΔUT1 and ΔLOD variation coefficients for nine major tides based on EOT11a. Oceanic currents for the calculation of relative OTAM are derived from EOT11a surface elevation data using the inversion algorithm described in Chapter 4. The parametrization for the inversion process is specified in Chapter 5.

Tide	Delaunay arguments						Doodson number	Period (hours)	ΔUT1		ΔLOD	
	γ	l	l'	F	D	Ω			sin (μs)	cos (μs)	sin (μs)	cos (μs)
Q_1	1	-1	0	-2	0	-2	135.655	26.8684	3.8	-1.9	-10.8	-21.5
O_1	1	0	0	-2	0	-2	145.555	25.8193	12.6	-10.0	-58.1	-73.4
P_1	1	0	0	-2	2	-2	163.555	24.0659	3.8	-2.4	-14.8	-24.0
K_1	1	0	0	0	0	0	165.555	23.9345	-13.2	8.0	50.5	83.2
$2N_2$	2	-2	0	-2	0	-2	235.755	12.9054	-0.4	-0.4	-4.3	5.1
N_2	2	-1	0	-2	0	-2	245.655	12.6583	-2.7	-2.2	-25.7	32.0
M_2	2	0	0	-2	0	-2	255.555	12.4206	-14.9	-6.9	-84.1	181.1
S_2	2	0	0	-2	2	-2	273.555	12.0000	-8.0	-1.8	-22.1	100.1
K_2	2	0	0	0	0	0	275.555	11.9672	-2.1	-0.3	-4.1	26.6

Table 5.8: Overview of different ERP models derived from the empirical ocean tide model EOT11a. Type 'H' stands for heights, 'C' for currents.

Nr.	Type	Based on	Tides	Resolution	Parameters
1	H	EOT11a	9 major tides	0.125°	Tolerance $t = 10^{-9}$, relax factor $f_r = 0.1$, weights: Table 5.1
	C	Inversion (based on EOT11a elevations)	9 major tides	0.5°	
2	H	EOT11a, admittance interpolation of OTAM	9+19 ^a	0.125°	Minor tides: Quadratic admittance interpolation of OTAM values
	C	Inversion, admittance interpolation of OTAM	9+19 ^a	0.5°	Minor tides: Quadratic admittance interpolation of OTAM values using weights of tidal current solution from Table 5.13
FF5	H	EOT11a, admittance interpolation of OTAM	9+10 ^b	0.125°	Minor tides: Quadratic admittance interpolation of OTAM values
	C	Inversion, admittance interpolation of OTAM	9+10 ^b	0.5°	Minor tides: Quadratic admittance interpolation of OTAM values using weights of tidal current solution from Table 5.13

^a 165.565, 145.545, 275.565, 255.545, 247.455, 175.455, 155.655, 237.555, 265.455, 272.556, 185.555, 137.455, 135.645, 127.555, 155.455, 165.545, 185.565, 162.556, 125.755; accounted for by admittance interpolation of OTAM values of nine EOT11a tides.

^b 165.565, 255.545, 237.555, 265.455, 185.555, 137.455, 135.645, 155.455, 165.545, 185.565; accounted for by admittance interpolation of OTAM values of nine EOT11a tides.

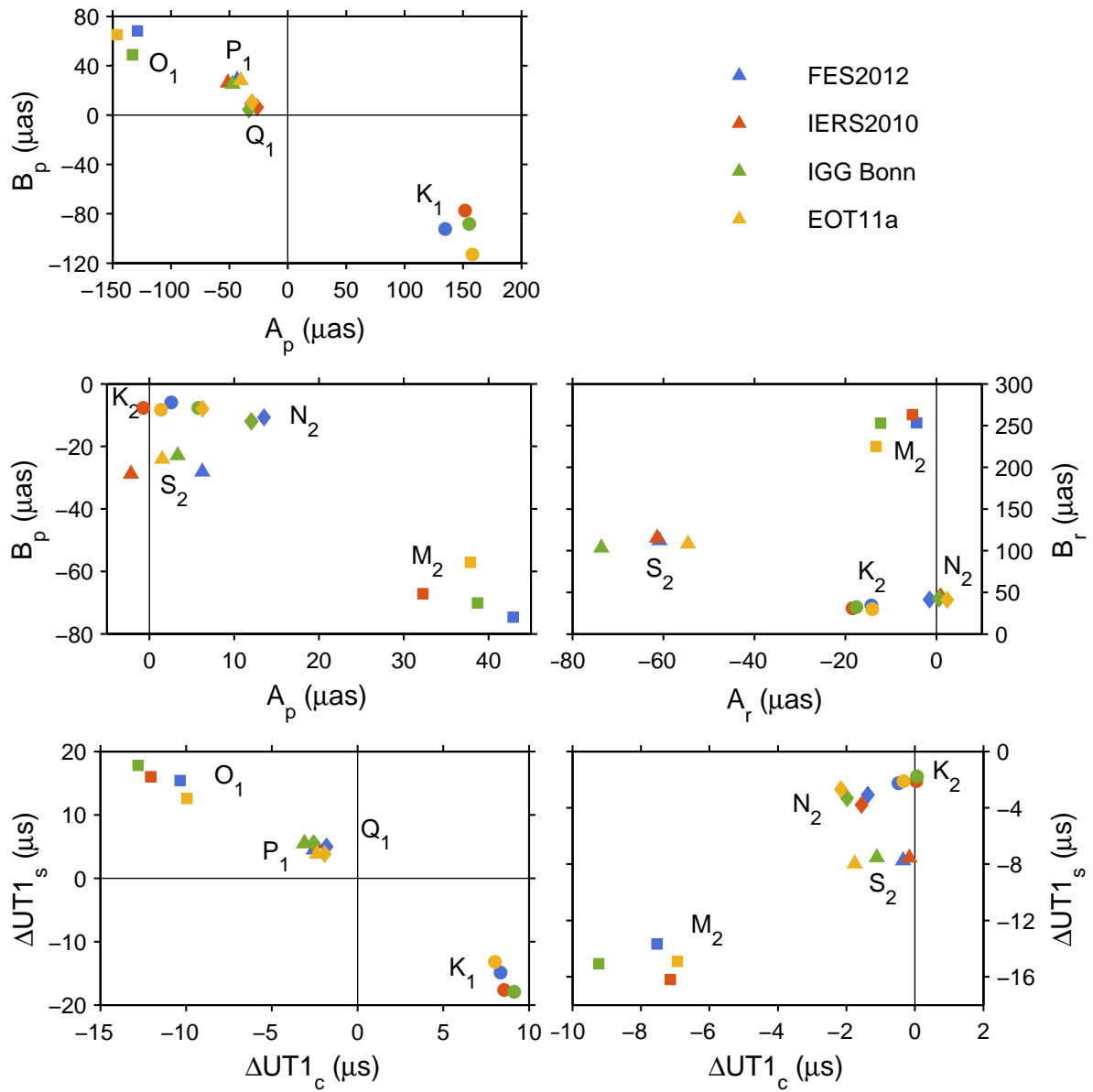


Figure 5.5: Phasor diagrams for ERP variations for eight major tidal constituents. Subscripts p and r for polar motion denote prograde and retrograde components, respectively. Subscripts c and s for ΔUT1 denote cosine- and sine-amplitudes, respectively.

parison (Stammer *et al.*, 2014) are OSU12 (Fok, 2012) and EOT11a (Savcenko & Bosch, 2012). Those consist of 10 and 11 high-frequency tides, respectively. The model recommended by the IERS (Petit & Luzum, 2010) consists of 71 tidal constituents, Artz *et al.* (2011) find that 83 terms for polar motion and 63 terms for UT1–UTC are above the significance level (3σ). Gipson (1996) includes 41 tidal constituents in his empirical tidal ERP model using a 3σ criterion as well but a shorter time span of observations (17 years compared to 30 years for Artz *et al.* (2011)).

As this work seeks to use an empirical ocean tide model for the derivation of a high-frequency ERP model, minor tidal constituents should be taken into account as well. Aside from hydrodynamic modeling, there are two possible ways to estimate tidal heights of those smaller but significant constituents. The minor tides could, just as the major tides, be empirically estimated from satellite altimetry data. However, empirical estimates have not been published so far and the results from Bosch *et al.* (2014) show that further investigations on this topic are required.

The second possibility to include minor constituents in an ocean tide model is using the response analysis method (Munk & Cartwright, 1966). The response—sometimes referred to as black box—relates the input to the output signal. If both signals are known, one can compute the response of the system. The quotient of input and output defines the admittance, therefore the response analysis method is often referred to as admittance approach (Pugh & Woodworth, 2014).

As tidal analysis method, the response relates the equilibrium tidal potential (input) to the tidal height variation (output) by the response function (Munk & Cartwright, 1966),

$$Z(\omega) = \frac{H(\omega)}{G(\omega)}, \quad (5.1)$$

where $H(\omega)$ is the tidal height, and $G(\omega)$ is the equilibrium tidal potential. Munk & Cartwright (1966) found that it is a smooth function of frequency within the same frequency band and can, thus, be used for the determination of minor tides. Using the assumption of smoothness, the admittance—being the ratio of the tidal height and the equilibrium tidal potential—can be linearly interpolated from two known (major) tides with neighboring frequencies. With a known input (potential) and the calculated response function, it is possible to derive the tidal height of a (near-by frequency) minor tide.

It is worth mentioning that different analysis institutions use different interpolation approaches. The IERS Conventions (Petit & Luzum, 2010) suggest linear interpolation for all tidal ranges. The FES prediction software uses linear interpolation for diurnal tides and quadratic spline interpolation for semi-diurnal tides (Le Provost *et al.*, 1991). This work uses quadratic interpolation in the final determination of tidal heights of minor tides. However, it should be noted that different interpolation methods for minor tides can reach tidal differences of 2 cm or more (W. Bosch, personal communication, 2014) and further studies on the smoothness of the admittance is desirable.

The pivot waves, i.e., the major tidal constituents to be used for the linear interpolation of

Table 5.9: Admittance interpolation coefficients for the five largest diurnal tides not included in EOT11a. Tidal frequencies and tide generating potential values are taken from the HW95 catalog.

Minor tide	Q_1	O_1	K_1
145.545	0.003995	0.187924	
M_1 155.655		0.038978	0.028197
K_{1+} 165.565		-0.000383	0.135980
J_1 175.455		-0.038992	0.083676
Oo_1 185.555		-0.043020	0.061199

minor tides, are given in Table 6.7 in Petit & Luzum (2010). For example, to interpolate tide K_{1+} (Doodson number 165.565), pivot waves O_1 (145.555) and K_1 (165.555) are used. If tidal heights of minor tides are calculated as weighted average, linear interpolation coefficients for two pivot waves (per minor tide) can be calculated. Those “height factors” are then multiplied with tidal heights of the pivot waves giving the tidal height of the minor tide. The formulation of those interpolation coefficients is as follows. The weighted average interpolation of the admittance can be written as

$$\frac{H_m}{G_m} = \left(\frac{\omega_2 - \omega_m}{\omega_2 - \omega_1} \right) \frac{H_1}{G_1} + \left(\frac{\omega_m - \omega_1}{\omega_2 - \omega_1} \right) \frac{H_2}{G_2} \quad (5.2)$$

where subscript m denotes the minor tide, and subscripts 1 and 2 denote pivot waves 1 and 2, respectively. The tidal height of the minor tide can be calculated using

$$H_m = \left(\frac{\omega_2 - \omega_m}{\omega_2 - \omega_1} \cdot \frac{G_m}{G_1} \right) H_1 + \left(\frac{\omega_m - \omega_1}{\omega_2 - \omega_1} \cdot \frac{G_m}{G_2} \right) H_2 \quad (5.3)$$

where the two terms in brackets denote the scalar interpolation coefficients. Tables 5.9 and 5.10 summarize these coefficients for the largest minor tides not included in the empirical ocean tide model EOT11a.

5.1.1 Admittance transferred to ocean tidal angular momentum

Due to the linear relationship between tidal heights and mass terms of ocean tidal angular momentum (likewise between tidal currents and motion terms), it is in principle also possible to interpolate OTAM directly using the admittance theory instead of interpolating the tidal heights. As OTAM-interpolation is a new concept, first studies—beyond this thesis—on that topic are desirable. It, however, requires the ratio of OTAM and tidal potential to be a smooth function of frequency, similar to the response function (Equation 5.1). Figure 5.6 shows this ratio for semi-diurnal and diurnal tides for the mass term. OTAM amplitudes (mass term) are taken from the FES2012

Table 5.10: Admittance interpolation coefficients for the six largest semi-diurnal tides not included in EOT11a. Tidal frequencies and tide generating potential values are taken from the HW95 catalog.

Minor tide		$2N_2$	N_2	M_2	K_2
μ_2	237.555	1.045498	0.021376		
ν_2	247.455		0.164549	0.004868	
	255.545		0.000790	0.037163	
L_2	265.455			0.014254	0.110916
T_2	272.556			0.003047	0.190827
K_{2+}	275.565			-0.000076	0.298707

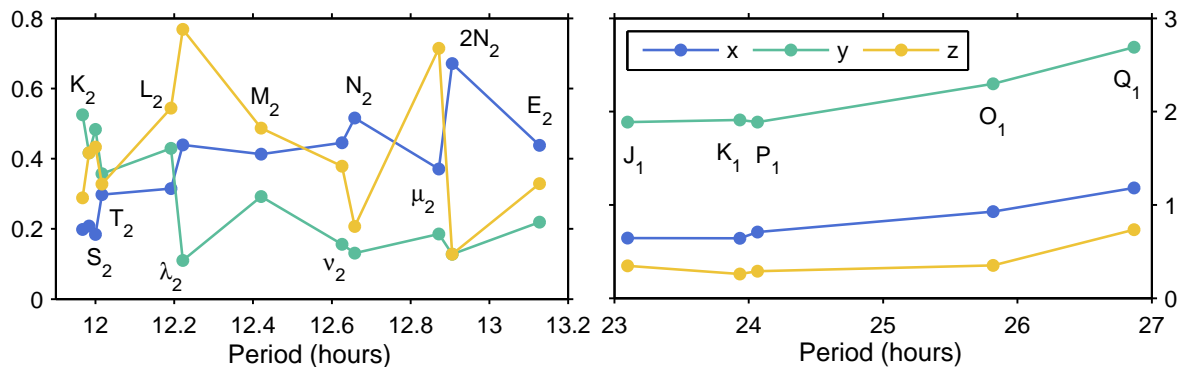


Figure 5.6: Admittance theory for the interpolation of OTAM. Shown are ratio values of OTAM (mass term) and tidal potential amplitudes for diurnal (right) and semi-diurnal (left) partial tides. Angular momentum values are derived from FES2012, tidal potential amplitudes are taken from the HW95 catalog. Diurnal tides show a smooth and linear variation with frequency. OTAM of minor tides in the diurnal band are, thus, suitable for linear interpolation. The non-linear variation of admittance in the semi-diurnal band is not well suited for (linear) interpolation. Units are 10^{25} kg s.

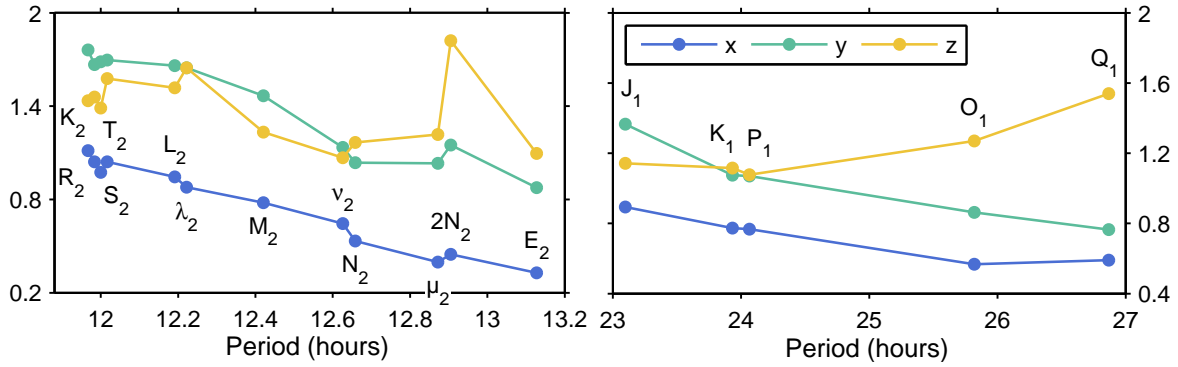


Figure 5.7: Admittance theory for the interpolation of OTAM. Shown are ratio values of OTAM (motion term) and tidal potential amplitudes for diurnal (right) and semi-diurnal (left) partial tides. Angular momentum values are derived from the oceanic currents from FES2012, tidal potential amplitudes are taken from the HW95 catalog. Units are 10^{25} kg s.

hydrodynamic assimilation model, tidal potential amplitudes from the HW95 catalog. All high-frequency tidal constituents included in FES2012, except for S_1 (due to the radiational part) and the non-linear MKS_2 , are used. The admittance function is calculated using $Z(\omega) = H_i(\omega)/G(\omega)$ where H_i stands for an OTAM component ($i = 1 \dots 3$ denotes components x , y , and z) of one partial tide, and $G(\omega)$ is the equilibrium tidal potential. The smooth admittance variation of diurnal tides (Figure 5.6, right) indicates a linear behavior of the response of OTAM to tidal potential. It can therefore be stated that mass terms of angular momentum of diurnal tides can be interpolated using the admittance theory to derive mass terms of OTAM of minor tides. For comparison, the angular momentum components of partial tides K_1 , P_1 and O_1 have been interpolated using the response method as described above. The mean error over all three components and all three partial tides is $3.5 \cdot 10^{23}$ kg m^2/s or 9.3%. The clearly largest difference stems from the H_3 (z) component of O_1 where interpolation of the OTAM component differs by 61.6% from the original FES2012 OTAM value. All other components show a mutual agreement better than 15%. For the admittance of semi-diurnal tides, however, the smooth variation with frequency cannot be seen. This means that linear interpolation of the admittance function might not be suitable for the mass term derivation of OTAM of semi-diurnal minor tides.

The admittance test calculations are also performed for the motion term of angular momentum. The relative OTAM are again derived from FES2012 by numerical integration of oceanic currents, tidal potential amplitudes are taken from HW95. The admittance values, $Z(\omega) = h_i(\omega)/G(\omega)$, are shown in Figure 5.7. $G(\omega)$ denotes potential amplitudes as before, $h_i(\omega)$ are amplitudes of relative angular momentum changes for components $i = 1 \dots 3$. The diurnal tides again show a smooth variation with frequency and, thus, allow linear interpolation of OTAM. Semi-diurnal tides, on the other hand, have a larger variation, especially in the z -component. However, the admittance using motion terms of OTAM are much smoother than the admittance using mass terms. In particular the equatorial (x and y) components show a quite linear dependence with frequency. Furthermore, this comparison includes more than twice

as many semi-diurnal tides than diurnal tides (12 compared to 5), which also might increase the noise level of the admittance in the semi-diurnal range.

To study the difference in estimating tidal heights using admittance interpolation and direct OTAM interpolation, the following comparison is performed: Based on nine major tides from EOT11a, tidal heights of the 25 largest minor tides are calculated using admittance theory. The derived heights are integrated using Equations (3.25)–(3.26) and Simpson’s rule in order to calculate the mass term of angular momentum. On the other hand, ocean tidal angular momentum is directly interpolated from known values at major tides. The RMS and relative RMS values (see Equations 4.14 and 4.15) for the comparison are shown in Table 5.11. Quadratic admittance interpolation is used.

The comparison shows that there are only small differences between the two possibilities of deriving the mass term of OTAM. The mutual agreement is largely within a few percent. The largest difference occur at partial tide μ_2 where the angular momentum values differ by 4.08%. In addition, Table 5.11 contains a comparison with respect to OTAM from the hydrodynamic ocean tide model FES2012. There can be seen large deviations from the EOT11a-derived values, ranging from 27.1% to 97.9%. However, smaller tides are difficult to detect in satellite altimetry and significant differences between ocean tide models can be expected. For example, the smallest tidal constituent available in EOT11a, $2N_2$, differs by 10.8%, 61.3%, and 47.2%, for the x , y , and z OTAM component, respectively.

5.2 Inclusion of minor tides

The comparison between admittance interpolation of OTAM and admittance interpolation of tidal heights indicates that it is, in principle, possible to interpolate OTAM directly. Analogously, OTAM motion terms can be interpolated from motion terms of major tidal constituents, which are deduced from tidal currents using the inversion algorithm. In this way, 19 minor tides down to $0.013 \text{ m}^2/\text{s}^2$ or 1.05% are considered for supplementing the nine tides of EOT11a by using quadratic admittance interpolation of OTAM,

$$H_m = \sum_{i=1}^3 \left(\frac{G_m}{G_i} H_i \prod_{k=1, k \neq i}^3 \frac{\omega_m - \omega_k}{\omega_i - \omega_k} \right). \quad (5.4)$$

In Equation 5.4, H denotes OTAM values (mass term, motion term and x , y , and z components are treated independently) of the minor tide (subscript m) and the major tides (subscript i), respectively; G denotes the tide generating potential amplitudes; and ω denotes tidal frequencies.

13 of the 19 additional tidal constituents—165.565, 145.545, 175.455, 155.655, 185.555, 137.455, 135.645, 127.555, 155.455, 165.545, 185.565, 162.556, and 125.755—are part of the diurnal band; six constituents—275.565, 255.545, 247.455, 237.555, 265.455, and 272.556—are semi-diurnal tides.

The pivot waves, i.e., the known sampling points for the interpolation, are shown in Ta-

Table 5.11: Comparison of OTAM derived from (1) admittance interpolation of tidal heights and integration, and (2) direct admittance interpolation of OTAM values. Mean values over components x , y , and z are shown. The last column gives (if available) corresponding RMS values for the comparison of OTAM from the ocean tide model FES2012. Units: RMS in 10^{20} kg m²/s, relative RMS in percent.

Tide	RMS (relative RMS)	RMS w.r.t FES2012
165.565	9.7 (0.24%)	
145.545	7.7 (0.07%)	
275.565	11.6 (0.65%)	
255.545	16.9 (0.78%)	
247.455 (ν_2)	18.3 (1.65%)	294.4 (27.1%)
175.455 (J_1)	63.4 (1.41%)	1422.4 (34.1%)
155.655 (M_1)	21.9 (1.97%)	
237.555 (μ_2)	28.6 (4.08%)	919.7 (97.9%)
265.455 (L_2)	12.3 (0.77%)	1048.7 (57.9%)
272.556 (T_2)	8.1 (0.77%)	300.7 (31.1%)
185.555 (OO_1)	94.3 (2.05%)	
137.455 (ρ_1)	3.5 (0.20%)	
135.645	4.4 (0.23%)	
127.555 (σ_1)	9.8 (0.37%)	
155.455	7.9 (1.90%)	
165.545	1.4 (0.25%)	
185.565	60.6 (2.05%)	
162.556 (π_1)	3.3 (0.87%)	
125.755 ($2Q_1$)	9.1 (0.39%)	
167.555 (φ_1)	1.8 (0.26%)	
227.655 (ε_2)	18.2 (3.39%)	450.3 (58.1%)
263.655 (λ_2)	3.2 (0.77%)	314.1 (72.8%)
245.645	3.5 (1.80%)	
285.455 (η_2)	7.3 (1.09%)	
265.655	3.1 (0.77%)	

Table 5.12: Pivot waves for quadratic admittance interpolation. The minor tides are ordered by their potential amplitude.

Minor tide	Q ₁	O ₁	P ₁	K ₁	2N ₂	N ₂	M ₂	S ₂	K ₂
K' ₁	165.565		O ₁	P ₁	K ₁				
	145.545	Q ₁	O ₁	P ₁					
K' ₂	275.565						M ₂	S ₂	K ₂
	255.545					N ₂	M ₂	S ₂	
ν ₂	247.455				2N ₂	N ₂	M ₂		
J ₁	175.455		O ₁	P ₁	K ₁				
M ₁	155.655		O ₁	P ₁	K ₁				
μ ₂	237.555				2N ₂	N ₂	M ₂		
L ₂	265.455						M ₂	S ₂	K ₂
T ₂	272.556						M ₂	S ₂	K ₂
OO ₁	185.555		O ₁	P ₁	K ₁				
ρ ₁	137.455	Q ₁	O ₁	P ₁					
	135.645	Q ₁	O ₁	P ₁					
σ ₁	127.555	Q ₁	O ₁	P ₁					
	155.455		O ₁	P ₁	K ₁				
	165.545		O ₁	P ₁	K ₁				
	185.565		O ₁	P ₁	K ₁				
π ₁	162.556		O ₁	P ₁	K ₁				
2Q ₁	125.755	Q ₁	O ₁	P ₁					

ble 5.12. Two of the three pivot waves are taken to be the same as for the linear admittance interpolation, i.e., as they are recommended by the IERS Conventions 2010 and shown in Table 6.7 in Petit & Luzum (2010). The third major tide is selected to be the closest of the remaining constituents. Eight minor tides are interpolated from pivot waves O₁, P₁, and K₁, the remaining five tides use the lower-frequency Q₁ instead of K₁. Half of the semi-diurnal minor tides are interpolated using the high-frequency pivot tides K₂, S₂, and M₂. Only one (255.545) is based on N₂ instead of K₂ and the two remaining partial tides—ν₂ and μ₂—use 2N₂ instead of S₂.

OTAM values are interpolated quadratically from OTAM values of major tides. For the motion term, major OTAM values from different continuity weight-solutions are used in the interpolation scheme. These are taken to be consistent, i.e., similar weight values for the minor tides as for the corresponding pivot waves (mentioned in Table 5.1) are used. The equatorial weight for diurnal tides is, thus, taken to be 10000, the polar weight 1000. For semi-diurnal components, the equatorial weight is 600, the polar weight is 600 or 1000. The values are summarized in Table 5.13. The resultant OTAM for the 19 minor tides are shown in Table 5.14.

ERP variations are derived again using the equations from Section 3.7. These contain both the

Table 5.13: Weights on the continuity equation used for the OTAM (motion term) interpolation of minor tides.

Minor tide	Weight for h_1, h_2	Weight for h_3
255.545	600	600
ν_2 247.455	600	600
μ_2 237.555	600	600
other semi-diurnals	600	1000
all diurnals	10000	1000

nine partial tides included in the empirical ocean tide model EOT11a and the 19 minor tides derived from quadratic admittance interpolation of OTAM. The polar motion coefficients are found in Table 5.15, those for UT1 and LOD in Table 5.16.

Table 5.14: OTAM of minor tides from the empirical ocean tide model EOT11a. Shown are tidal constituents not included in EOT11a with the largest tide generating potential. OTAM values are derived using quadratic admittance interpolation. Tidal currents of major tides are estimated using the algorithm described in Chapter 4. The weights for the continuity equation for the respective components of major tides are written in Table 5.13. Amplitudes in 10^{25} kg m²/s, phases in degrees.

Tide	Mass terms (heights)						Motion terms (currents)					
	H_1		H_2		H_3		h_1		h_2		h_3	
	Amp	Pha	Amp	Pha	Amp	Pha	Amp	Pha	Amp	Pha	Amp	Pha
165.565	0.061	308.2	0.186	223.6	0.025	20.1	0.071	74.5	0.119	164.5	0.095	226.8
145.545	0.091	329.4	0.221	222.2	0.032	171.0	0.051	55.7	0.093	157.7	0.102	240.2
275.565	0.010	49.7	0.025	12.2	0.024	101.6	0.045	69.7	0.072	161.9	0.063	24.4
255.545	0.019	9.3	0.013	305.6	0.022	84.7	0.036	105.5	0.056	192.3	0.063	42.3
247.455	0.023	350.2	0.007	247.3	0.009	62.7	0.035	125.9	0.044	201.2	0.058	45.4
175.455	0.039	252.0	0.087	228.8	0.036	23.5	0.048	220.8	0.114	168.2	0.104	237.7
155.655	0.033	335.7	0.078	221.1	0.005	185.3	0.051	61.6	0.024	154.9	0.019	216.2
237.555	0.023	324.7	0.003	148.3	0.011	151.4	0.018	143.1	0.030	191.9	0.062	39.3
265.455	0.009	9.6	0.011	347.2	0.023	208.1	0.034	96.9	0.050	171.5	0.045	16.1
272.556	0.007	38.0	0.016	8.6	0.012	149.7	0.033	78.1	0.052	163.4	0.044	19.3
185.555	0.046	231.1	0.061	234.1	0.039	26.4	0.097	231.0	0.121	169.2	0.119	241.8
137.455	0.021	337.5	0.048	216.5	0.011	141.2	0.012	66.6	0.017	153.9	0.021	248.8
135.645	0.022	338.7	0.049	215.5	0.012	137.4	0.013	68.7	0.017	153.2	0.022	250.2
127.555	0.023	346.1	0.048	208.2	0.019	119.8	0.017	79.5	0.014	148.4	0.020	259.5
155.455	0.012	335.8	0.028	221.1	0.002	185.3	0.018	61.5	0.009	154.8	0.007	216.4
165.545	0.009	308.6	0.027	223.6	0.004	20.1	0.011	74.2	0.017	164.5	0.014	226.6
185.565	0.030	231.0	0.039	234.2	0.025	26.4	0.062	231.0	0.078	169.2	0.077	241.8
162.556	0.009	319.1	0.026	222.7	0.002	20.2	0.013	68.5	0.014	162.8	0.011	222.6
125.755	0.019	347.2	0.041	207.1	0.017	117.9	0.016	80.7	0.011	147.5	0.017	261.0

Table 5.15: Polar motion variation coefficients for 28 tides based on EOT11a. In addition to nine tides included in the ocean tide model, OTAM values of 19 minor tides are derived from quadratic admittance interpolation. Details about this model 2 is given in Table 5.8.

Tide	Delaunay arguments						Doodson number	Period (hours)	px_s (μ as)	px_c (μ as)	py_s (μ as)	py_c (μ as)
	γ	l	l'	F	D	Ω						
SQ ₁	1	-2	0	-2	0	-2	125.755	28.0062	-2.0	11.2	-11.2	-2.0
σ_1	1	0	0	-2	-2	-2	127.555	27.8484	-2.4	12.7	-12.7	-2.4
	1	-1	0	-2	0	-1	135.645	26.8728	-1.5	11.2	-11.2	-1.5
Q ₁	1	-1	0	-2	0	-2	135.655	26.8684	10.3	30.5	-30.5	10.3
ρ_1	1	1	0	-2	-2	-2	137.455	26.7231	-1.3	10.7	-10.7	-1.3
	1	0	0	-2	0	-1	145.545	25.8234	-3.0	45.5	-45.5	-3.0
O ₁	1	0	0	-2	0	-2	145.555	25.8193	65.1	146.1	-146.1	65.1
	1	1	0	-2	0	-2	155.455	24.8492	1.5	-7.3	7.3	1.5
M ₁	1	-1	0	0	0	0	155.655	24.8332	4.0	-20.4	20.4	4.0
π_1	1	0	-1	-2	2	-2	162.556	24.1321	-0.2	7.0	-7.0	-0.2
P ₁	1	0	0	-2	2	-2	163.555	24.0659	28.1	40.3	-40.3	28.1
	1	0	0	0	0	1	165.545	23.9380	0.4	7.1	-7.1	0.4
K ₁	1	0	0	0	0	0	165.555	23.9345	-113.0	-158.0	158.0	-113.0
	1	0	0	0	0	-1	165.565	23.9310	-2.8	-48.8	48.8	-2.8
J ₁	1	1	0	0	0	0	175.455	23.0985	-13.1	-18.2	18.2	-13.1
OO ₁	1	0	0	2	0	2	185.555	22.3061	-17.5	-8.1	8.1	-17.5
	1	0	0	2	0	1	185.565	22.3030	-11.2	-5.2	5.2	-11.2
2N ₂	2	-2	0	-2	0	-2	235.755	12.9054	-6.6	-0.9	1.1	4.0
μ_2	2	0	0	-2	-2	-2	237.555	12.8718	-6.8	1.3	0.0	-0.1
N ₂	2	-1	0	-2	0	-2	245.655	12.6583	-49.0	-8.7	3.9	33.2
ν_2	2	1	0	-2	-2	-2	247.455	12.6260	-9.1	4.6	-0.6	-5.3
	2	0	0	-2	0	-1	255.545	12.4215	10.1	-4.3	-1.1	7.7
M ₂	2	0	0	-2	0	-2	255.555	12.4206	-282.1	-24.6	51.1	167.8
L ₂	2	1	0	-2	0	-2	265.455	12.1916	8.3	1.0	-0.6	7.2
T ₂	2	0	-1	-2	2	-2	272.556	12.0164	-7.5	-3.3	2.2	-7.2
S ₂	2	0	0	-2	2	-2	273.555	12.0000	-132.3	53.1	56.1	84.3
K ₂	2	0	0	0	0	0	275.555	11.9672	-38.0	12.7	15.5	21.4
	2	0	0	0	0	-1	275.565	11.9664	-9.8	-5.2	4.0	-9.8

Table 5.16: ΔUT1 and ΔLOD variation coefficients for 28 tides based on EOT11a. In addition to nine tides included in the ocean tide model, OTAM values of 19 minor tides are derived from quadratic admittance interpolation. Details about this model 2 is given in Table 5.8.

Tide	Delaunay arguments						Doodson number	Period (hours)	ΔUT1_s (μs)	ΔUT1_c (μs)	ΔLOD_s (μs)	ΔLOD_c (μs)
	γ	l	l'	F	D	Ω						
SQ ₁	1	-2	0	-2	0	-2	125.755	28.0062	-0.1	-0.2	-1.3	0.8
σ_1	1	0	0	-2	-2	-2	127.555	27.8484	-0.2	-0.3	-1.6	1.1
	1	-1	0	-2	0	-1	135.645	26.8728	-0.4	-0.4	-2.1	2.1
Q ₁	1	-1	0	-2	0	-2	135.655	26.8684	3.8	-1.9	-10.8	-21.5
ρ_1	1	1	0	-2	-2	-2	137.455	26.7231	-0.4	-0.4	-2.1	2.1
	1	0	0	-2	0	-1	145.545	25.8234	-2.1	-1.9	-11.0	12.5
O ₁	1	0	0	-2	0	-2	145.555	25.8193	12.6	-10.0	-58.1	-73.4
	1	1	0	-2	0	-2	155.455	24.8492	0.1	0.2	1.1	-0.6
M ₁	1	-1	0	0	0	0	155.655	24.8332	0.3	0.5	2.8	-1.7
π_1	1	0	-1	-2	2	-2	162.556	24.1321	-0.2	-0.2	-1.0	1.0
P ₁	1	0	0	-2	2	-2	163.555	24.0659	3.8	-2.4	-14.8	-24.0
	1	0	0	0	0	1	165.545	23.9380	-0.2	-0.2	-1.0	1.3
K ₁	1	0	0	0	0	0	165.555	23.9345	-13.2	8.0	50.5	83.2
	1	0	0	0	0	-1	165.565	23.9310	1.5	1.1	7.0	-9.3
J ₁	1	1	0	0	0	0	175.455	23.0985	1.7	0.7	4.5	-11.4
OO ₁	1	0	0	2	0	2	185.555	22.3061	2.0	0.7	4.4	-13.5
	1	0	0	2	0	1	185.565	22.3030	1.3	0.4	2.9	-8.8
2N ₂	2	-2	0	-2	0	-2	235.755	12.9054	-0.4	-0.4	-4.3	5.1
μ_2	2	0	0	-2	-2	-2	237.555	12.8718	-0.5	0.5	6.4	6.0
N ₂	2	-1	0	-2	0	-2	245.655	12.6583	-2.7	-2.2	-25.7	32.0
ν_2	2	1	0	-2	-2	-2	247.455	12.6260	-0.5	0.6	7.0	6.5
	2	0	0	-2	0	-1	255.545	12.4215	0.6	-0.7	-8.7	-7.1
M ₂	2	0	0	-2	0	-2	255.555	12.4206	-14.9	-6.9	-84.1	181.1
L ₂	2	1	0	-2	0	-2	265.455	12.1916	0.3	-0.1	-0.6	-4.1
T ₂	2	0	-1	-2	2	-2	272.556	12.0164	-0.4	0.2	2.8	5.0
S ₂	2	0	0	-2	2	-2	273.555	12.0000	-8.0	-1.8	-22.1	100.1
K ₂	2	0	0	0	0	0	275.555	11.9672	-2.1	-0.3	-4.1	26.6
	2	0	0	0	0	-1	275.565	11.9664	-0.6	0.5	6.5	7.9

Chapter 6

Comparison and validation of high-frequency Earth rotation models

The derived high-frequency ERP models from Chapter 5 are validated against the most precise models currently available. In this work, ERP prediction models have been derived from the ocean tide models FES2012, EOT11a, and HAMTIDE11a. From these “independent” models, FES2012 and EOT11a are validated in this chapter. In addition, due to precise space geodetic techniques, ERP models have been derived empirically in recent years (see Chapter 2 for details). The GPS-VLBI combined empirical model from Artz *et al.* (2012) is included in the subsequent comparison.

The following section briefly summarizes the least-squares method, a commonly applied parameter estimation process, also being used in the Vienna VLBI Software VieVS.

6.1 Parameter estimation process

A common method to solve overdetermined systems of possibly non-linear equations,

$$\Phi(\mathbf{x}) = \mathbf{b} \quad (6.1)$$

or, linearized and in matrix notation,

$$\mathbf{Ax} = \mathbf{b}, \quad (6.2)$$

is *Least Squares*. \mathbf{A} is the coefficient or design matrix, either linear or linearized (Jacobian); \mathbf{x} is the parameter vector; and \mathbf{b} is the observation or measurement vector. It minimizes the sum of the squared residuals,

$$\|\mathbf{r}\|^2 = \|\mathbf{Ax} - \mathbf{b}\|^2, \quad (6.3)$$

to estimate a set of (unknown) parameters. If the observations are samples of normally distributed random variables, the least squares method gives the same results as the maximum likelihood

estimation (Mikhail, 1976, p. 48). In addition to the deterministic part of a system (functional model), least squares typically includes a stochastic model to take into account the probabilistic properties of the variables. In practice, the variance-covariance matrix Σ , including variances of the observations as well as correlations between them, represents the stochastic behavior of the system (Perović, 2005). For numerical reasons, the cofactor matrix \mathbf{Q} is often used instead of Σ . It can be calculated by

$$\mathbf{Q} = \frac{1}{\sigma_0^2} \Sigma, \quad (6.4)$$

where σ_0^2 is called variance factor. Then, least squares requires the sum of the weighted residuals squared, $\mathbf{r}^T \mathbf{P} \mathbf{r}$, to be minimized. $\mathbf{P} = \mathbf{Q}^{-1}$ is the weight matrix. The parameter vector can be estimated using

$$\hat{\mathbf{x}} = \mathbf{x}_0 + \mathbf{N}^{-1} \mathbf{A}^T \mathbf{P} \mathbf{l} \quad (6.5)$$

where $\mathbf{N} = \mathbf{A}^T \mathbf{P} \mathbf{A}$ is the normal equation matrix, $\mathbf{l} = \mathbf{b} - \Phi(\mathbf{x}_0)$ is the reduced observation vector, and \mathbf{x}_0 is the a priori parameter vector. The corrections to the observations, i.e., estimated residuals, can be calculated using

$$\hat{\mathbf{r}} = \mathbf{A} \hat{\mathbf{x}} - \mathbf{l} \quad (6.6)$$

and the corrected observation vector is

$$\hat{\mathbf{b}} = \mathbf{b} + \hat{\mathbf{r}}. \quad (6.7)$$

If the model $\Phi(\mathbf{x})$ is linear in all unknowns \mathbf{x} , no a priori parameters are necessary and the least squares solution is given by

$$\hat{\mathbf{x}} = \mathbf{N}^{-1} \mathbf{A}^T \mathbf{P} \mathbf{b}. \quad (6.8)$$

The a posteriori auto-cofactor matrices of (1) the estimated parameters $\hat{\mathbf{x}}$, (2) the estimated residuals $\hat{\mathbf{r}}$, and (3) the estimated observations $\hat{\mathbf{b}}$ are given by (Perović, 2005, p. 89)

$$\mathbf{Q}_{\hat{\mathbf{x}}} = \mathbf{N}^{-1} \quad (6.9)$$

$$\mathbf{Q}_{\hat{\mathbf{r}}} = \mathbf{P}^{-1} - \mathbf{A} \mathbf{N}^{-1} \mathbf{A}^T \quad (6.10)$$

$$\mathbf{Q}_{\hat{\mathbf{b}}} = \mathbf{A} \mathbf{N}^{-1} \mathbf{A}^T = \mathbf{Q}_b - \mathbf{Q}_{\hat{\mathbf{r}}}. \quad (6.11)$$

Similar to Equation 6.4, covariance matrices are obtained by multiplication of the respective co-

factor matrix with the variance factor σ_0^2 . An unbiased estimate for σ_0^2 is given by

$$\hat{\sigma}_0^2 = \frac{\hat{\mathbf{r}}^T \mathbf{P} \hat{\mathbf{r}}}{n - u} \quad (6.12)$$

where n is the number of observations, u is the number of estimated parameters and $(n - u)$ is the degree of freedom. For example, the variance-covariance matrix a posteriori for the estimated parameters can be calculated using

$$\Sigma_{\hat{\mathbf{x}}} = \hat{\sigma}_0^2 \mathbf{Q}_{\hat{\mathbf{x}}}. \quad (6.13)$$

As many physical problems are non-linear, the system needs to be linearized around some a priori values of the parameters. An iterative method can be used to obtain the final solution. However, $\|\mathbf{r}\|^2$ might have multiple local minima and the solution might fail to obtain the desired solution.

The least squares adjustment in the Vienna VLBI Software (VieVS) estimates unknown parameters as piece-wise linear offset functions at integer hours UTC. The partial derivatives of the main VLBI observable, the time delay τ , with respect to the unknown parameters can be found in Teke *et al.* (2012). More details on the parameterization is given in Table 6.1.

For the case of VLBI analysis, the least squares solution requires additional constraints to handle the datum defect. The VLBI stations are bound to the terrestrial reference frame (TRF) only by definition because the free network is actually not attached to the terrestrial coordinates (the origin and the orientation of the coordinate system is not specified by the observations). This creates a rank deficiency in the design matrix which makes the normal equation matrix singular. A free VLBI network has typically a datum defect of six (degrees of freedom): three translations and three rotations if both TRF coordinates and EOP are estimated.

Thus, to define a geodetic datum for a VLBI network, constraints on the station coordinates are required. This can either be achieved by absolute constraints, i.e., fixing some stations, or by imposing no-net-rotation (NNR) and no-net-translation (NNT) conditions on all or on a subset of stations. The latter is achieved by minimizing the rotations and translations of a seven parameter Helmert transformation from an a priori TRF.

6.2 Validation using VLBI observations

Using observations from space geodetic techniques allows to perform an external validation of the ERP model and therewith also of the estimated barotropic currents. For this task VLBI observations are used and analyzed using the Vienna VLBI Software (VieVS, Böhm *et al.*, 2012), an easy-to-use and flexible VLBI data analysis software.

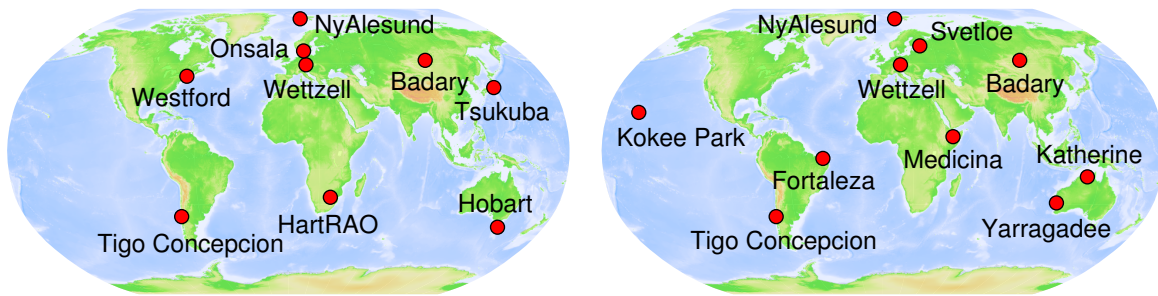


Figure 6.1: VLBI network of International VLBI Service for Geodesy and Astrometry (IVS) R1 (left) and R4 (right) sessions.

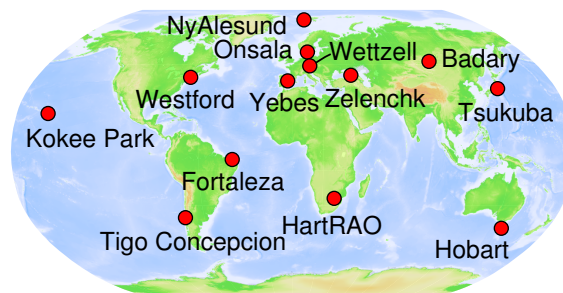


Figure 6.2: VLBI network of IVS CONT11 sessions.

6.2.1 Input data

297 VLBI experiments between 2011 and 2013 from the International VLBI Service for Geodesy and Astrometry (IVS; Schuh & Behrend, 2012) are used in the analysis. R1 and R4 sessions are 24-hours experiments carried out on Mondays and Thursdays, respectively. The main goal of these weekly sessions is to provide EOP on a regular basis. The “R” stands for rapid turnaround, meaning that results should be produced within 15 days after observation. Typical VLBI networks for R1 and R4 sessions are shown in Figure 6.1.

In addition to the weekly R1 and R4 sessions, VLBI experiments from a continuous campaign in 2011 are used in the analysis. The CONT11 campaign, consisting of 15 consecutive days of continuous observations by 13 VLBI stations, was carried out in the second half of September 2011 and should demonstrate the highest achievable accuracy using VLBI systems. As one of the scientific goals of CONT11 was the study of high-frequency ERP variations, these experiments are well suited for the present work. The network of VLBI stations for CONT11 is shown in Figure 6.2.

6.2.2 Analysis strategy

Due to the correlation between precession-nutation and polar motion (cf. Section 2.1), these parameters cannot be estimated simultaneously (Tesmer *et al.*, 2001). Brzeziński (2012), however, describes a technique allowing the simultaneous determination of celestial pole offsets and high-frequency ERP, the so-called complex demodulation. As this analysis technique has not been

Table 6.1: Parametrization of the VLBI analysis for the validation of the ERP model.

Parameter	A priori model	Estimated	Constraint
Ephemerides	JPL421	-	-
CRF	ICRF2	-	-
TRF	VieTRF13 (Krásná <i>et al.</i> , 2014)	Offset ^a	NNT/NNR
Polar motion	Pre-solution ^b [IERS 08 C04] + respective high-frequency model	Hourly [offset ^a]	1 mas after 1 hour
UT1-UTC	Pre-solution ^b [IERS 08 C04] + respective high-frequency model	Hourly [offset ^a]	1 ms after 1 hour
Prec.-Nut.	Pre-solution ^b [IAU2006/2000A]	- [offset ^a]	-
Hydrost. delay	Saastamoinen (p_0), VMF1	-	-
Wet delay ^c	-	Hourly	1.5 cm after 1 hour
Trop. gradients	-	6-hourly	0.5 mm after 6 hours
Clocks ^d	-	Hourly	1.3 cm after 1 hour

^a Per session.

^b EOP are estimated in a first step without estimating high-frequency ERP. Values in square brackets show the prior parametrization.

^c The wet delay was estimated as wet zenith delay.

^d Clocks are estimated as offset plus linear trend plus quadratic term per clock with respect to a reference clock.

implemented, a two-step approach is used: In the first analysis run, celestial pole and polar motion are estimated as daily offsets. In the first run, the IAU2006/2000A model and the IERS 08 C04 series are used as a priori models for precession-nutation and ERP, respectively. In the second run, the daily estimates from the pre-solution are used as a priori values for EOP. Precession-nutation values are then fixed to their a prioris and ERP are estimated hourly (high-frequency). The other parameters, i.e., all but EOP, are estimated with an equal parametrization in both runs.

The remaining estimated parameters are terrestrial coordinates of the VLBI stations (including NNT and NNR conditions), wet zenith delays, tropospheric gradients and clock parameters. The parameters are estimated as piece-wise linear offsets at (fractions of) integer hours UTC. A least-squares algorithm is used for the estimation. An overview of the parametrization as well as constraints is given in Table 6.1.

6.2.3 Validation results

To assess the accuracy of the models, spectral components from hourly ERP residuals of x-pole, y-pole, and UT1–UTC are calculated, for example

$$px(t) = \sum_{i=1}^{35} px_c \cos(\omega_i t) + px_s \sin(\omega_i t), \quad (6.14)$$

where px denotes the time series of one of the parameters (here: x-component of polar motion), ω_i are tidal frequencies, and px_c and px_s denote cosine- and sine-amplitudes, respectively.

Amplitudes and phases are derived in a least squares adjustment at 35 tidal frequencies: Starting from 71 tidal constituents from the IERS Conventions 2010, 36 frequencies are removed which would require observations >1 year to be separated from a larger constituent. Figure 6.3 shows estimated ERP from 2011 to 2013 and corresponding amplitude spectra using four a priori high-frequency ERP models.

The spectral amplitudes of different models are then subtracted from the same amplitudes derived from a reference solution. For example, if the reference model is FES2012, the difference in amplitude spectrum (DAS) is calculated to a test model, e.g. EOT11a, as

$$\text{DAS} = \text{AS}(x_{p(\text{FES2012})}) - \text{AS}(x_{p(\text{EOT11a})}). \quad (6.15)$$

AS stands for the estimated amplitude spectrum at 35 tidal frequencies (see Figure 6.3, right). As post-fit residuals of ERP are expected to be smaller if a model gives more accurate a priori prediction values, the DAS is suitable to assess the quality of the models. For example, if the EOT11a model is more accurate, the ERP residuals are smaller than those using the FES2012 model and DAS will be positive. The DAS of three models, namely (1) the IERS Conventions 2010 model; (2) the empirical ERP model by Artz *et al.* (2011), IGG Bonn; and (3) the model based on empirical ocean tides from EOT11a (model 1 in Table 5.8), with respect to a reference model (FES2012, all available tidal constituents) are shown in Figure 6.4. The model based on empirical ocean tides (EOT11a) shows mostly negative values, indicating that the ERP residuals are larger than those using the reference model FES2012. However, for some tidal frequencies the residuals decrease, such as for K_2 or for J_1 . For partial tides N_2 , M_2 , and T_2 some parameters improve, whereas others deteriorate. Apart from a few larger differences between the reference FES2012 and the EOT11a model, e.g., M_2 or O_1 in the pole coordinates, these two models show a better mutual agreement than with the empirical IGG Bonn model. This is very likely due to the fact that both FES2012 and EOT11a are based on satellite altimetry observations.

The number of tidal constituents might also play an important role in the accuracy of the four ERP models. The model based on EOT11a includes only nine partial tides, whereas the others include considerably more: FES2012 consists of 27 high-frequency tides, the IERS Conventions 2010 model incorporates 71 spectral lines—although it is primarily based on only 12 tides before applying the orthoweights functions—, and the empirical model from IGG Bonn includes 127 tidal constituents. The latter is expected to show the smallest post-fit ERP residuals as it is basically fitted to VLBI and GNSS observations of more than 30 years. Table 6.2 shows the number of tidal lines for all models where the respective model gives smallest ERP residuals. The models IERS2010 and IGG Bonn give on average the smallest residuals. EOT11a performs best for UT1–UTC where 12 of 35 spectral amplitudes are smaller than for all other models.

A common method to assess the accuracy of models in VLBI analysis is baseline scatter. The so-called baseline length repeatability is the standard deviation of the baseline lengths (linear

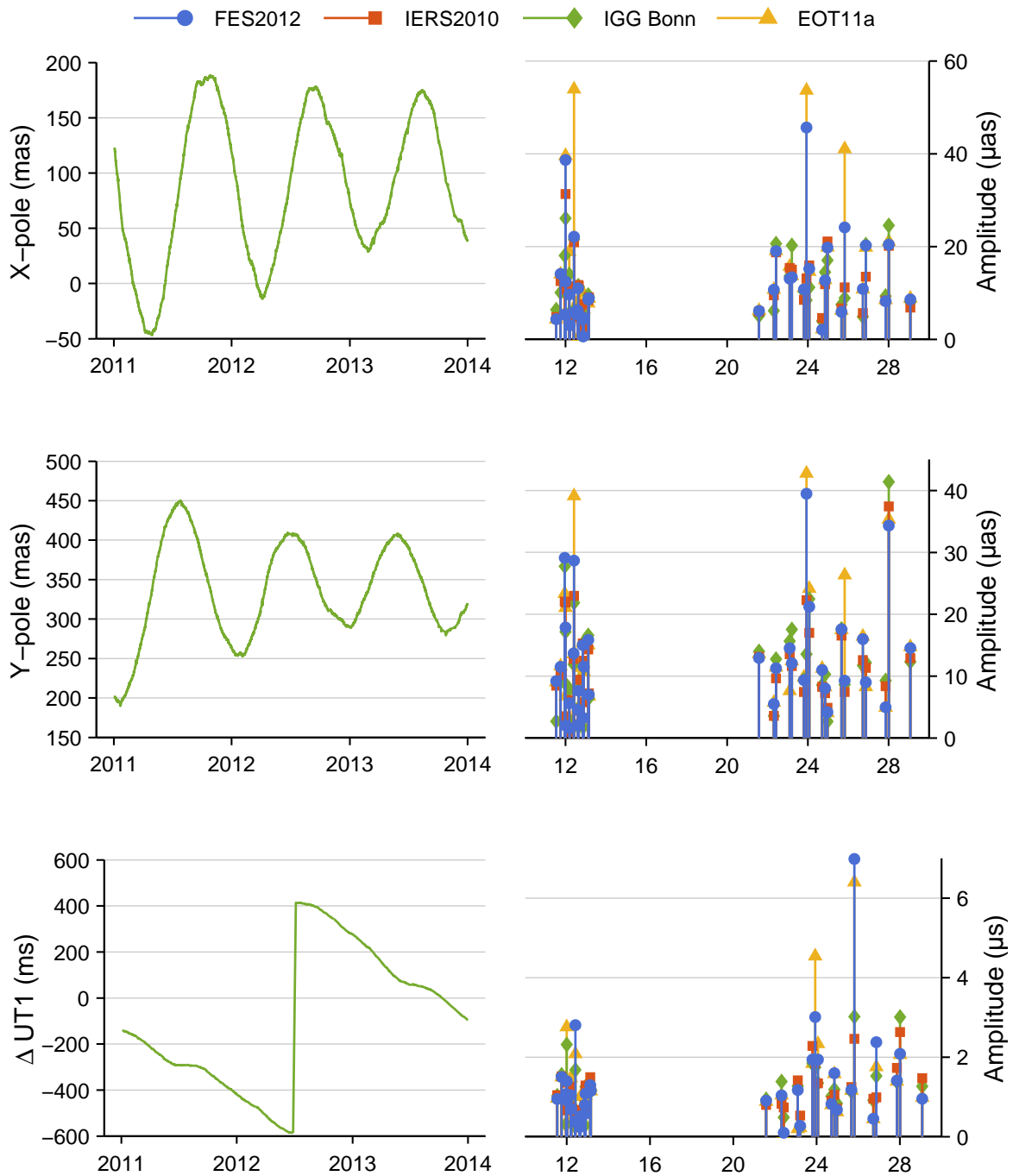


Figure 6.3: ERP estimates of 297 VLBI sessions between 2011 and 2014 using the high-frequency a priori ERP model IGG Bonn (left column). Right column shows corresponding amplitude spectra for (semi-)diurnal frequencies using four different a priori models (y-axis: Period in hours).

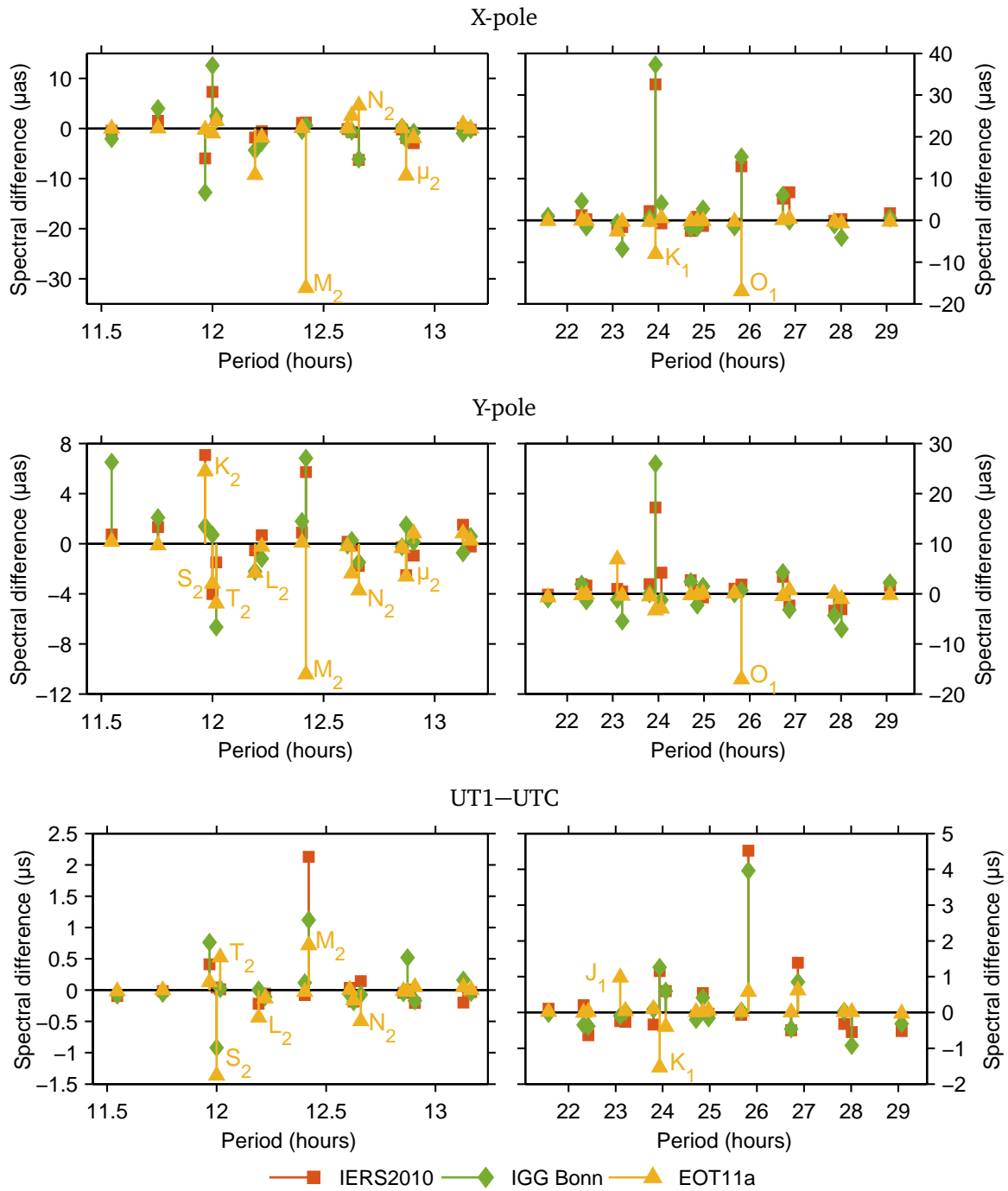


Figure 6.4: Amplitude spectra differences of ERP residuals from a VLBI solution using different high-frequency ERP models. Positive values indicate smaller ERP residuals and, thus, more accurate prediction values compared to a reference model. The reference model is FES2012.

Table 6.2: Number of tidal frequencies where the respective model gives smallest spectral amplitudes.

Model	Smallest residuals			
	X-pole	Y-pole	UT1–UTC	Total
FES2012	10	6	5	21
IERS2010	8	13	10	31
IGG Bonn	11	12	8	31
EOT11a	6	4	12	22

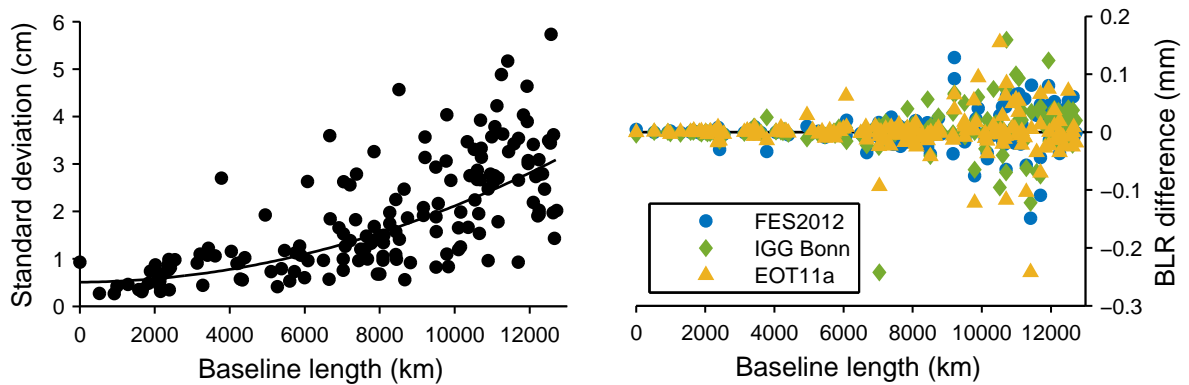


Figure 6.5: Standard deviation of baseline lengths (baseline length repeatability, BLR) from 297 VLBI sessions used for the model validation. The left image shows the repeatability using the IERS Conventions 2010 model. The right image shows repeatability differences for three high-frequency ERP models with respect to the reference (IERS Conventions 2010) model.

trend of station positions removed) over the whole observation period. The smaller it is, the more accurately a priori models describe physical effects. The baseline length repeatability of 161 baselines (these are shown which are included in >10 VLBI sessions) is shown in Figure 6.5 (left). The time series of some baselines is split into parts due to episodic changes of the VLBI reference point due to, e.g., earthquakes. For all these time periods, a standard deviation of baseline length is computed, and the final value is derived using the mean value. In addition, baselines whose estimated and a priori lengths differ by > 0.2 m are considered as being outliers.

The baseline length repeatability plots show hardly any visual differences between different high-frequency ERP models, therefore only the reference model (IERS Conventions 2010) is shown in Figure 6.5 (left). The right image shows the difference between baseline length repeatabilities using various Earth rotation models. There is no clear improvement for any of the models. However, the number of baselines improving due to a change of a priori models allows to assess their accuracy. The empirical model from IGG Bonn improves most baselines: 95 (59%) of 161 baselines are improved if the empirical model is used instead of the conventional model.

Table 6.3: Number of baselines for which the baseline length repeatability decreases (improves) or increases (degrade) if the high-frequency ERP model in the first column is used instead of the IERS Conventions 2010 model. EOT11a denotes the model derived from nine major tides included in the ocean tide model, i.e., model 1 in Table 5.8.

Model	Improved baselines	Degraded baselines
FES2012	77	84
IGG Bonn	95	66
EOT11a	77	84

The two models based on a long time-span of satellite altimetry observations do not show an overall improvement: Both the FES2012 model as well as the EOT11a model improve 77 (48%) baselines and degrade 84 baselines. That means that the models agree very well with respect to baseline length repeatability but do not show an improvement compared to the IERS standard model.

The validation results from baseline length repeatabilities largely agree with the analysis of ERP residuals from the VLBI solutions. Both analysis strategies favor IGG Bonn and IERS2010 as the two most accurate models. The models FES2012 and EOT11a degrade the majority of baselines and also show the least spectral components giving smallest residual amplitudes (Table 6.2).

6.3 Final model validation

Since nine major tides, as originally available from EOT11a, are presumed to be insufficient, minor tides are included in the ERP models as follows. Up to 19 largest additional tidal constituents are derived using the admittance approach on OTAM values. The influence of each partial minor tide is examined and one final model including ten additional tidal constituents is deduced for the ultimate comparison. All ERP models based on EOT11a are summarized in Table 5.8. The final model is denoted as FF5. Compared to the IERS Conventions model, model FF5 improves 74 (46%) of all 161 baselines indicating FF5 to predict ERP variations slightly less accurately than the conventional model. Polar motion and UT1 variation coefficients of model FF5 are written to Table A.1 and A.2, respectively.

The reference for the final validation is the empirical IGG Bonn model. It is compared to following models: FES2012, IERS Conventions 2010, and EOT11a FF5. The differences of spectra for x-pole, y-pole and UT1–UTC is given in Figure A.1. The statistics, i.e., number of components giving smallest residual amplitudes per model is shown in Table A.3. Similar to Figure 6.4, model FF5 based on an empirical ocean tide model shows large post-fit ERP residuals at frequencies of the major tidal constituents O_1 , K_1 , and M_2 . The spectral differences show a similar

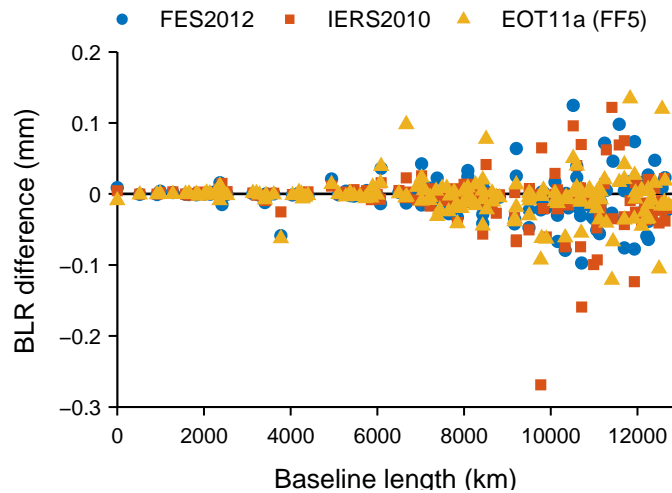


Figure 6.6: Baseline length repeatability differences of three high-frequency ERP models with respect to the reference model IGG Bonn.

behavior for the FES2012-derived ERP model. Especially partial tide K_1 has about twice as large spectral differences for x-pole and y-pole when compared to the EOT11a-derived model. Also, the amplitudes at frequencies of M_2 and O_1 show significant larger negative values than models IERS2010 and IGG Bonn. Due to their derivation based on recent ocean tide models, a feasible explanation are imperfect tidal heights and currents. In any case, the inversion algorithm for the derivation of tidal currents from tidal heights, including all deficiencies as mentioned in Chapter 4, is another source of error. However, from all 105 components (35 frequencies, three Earth rotation parameters), 28% (29) give smallest spectral residual amplitudes using model FF5, indicating the majority (equal IGG Bonn) of improved spectral components. UT1–UTC, in particular, shows smallest amplitudes for 14 (40%) components of 35 frequencies. The reference model IGG Bonn gives generally the smallest residuals, which is also emphasized by the number of smallest components (29, equal EOT11a FF5). Interestingly, the empirical model gives worse results for UT1–UTC than for polar motion, possibly due to a larger weight on GNSS than VLBI observations. Only seven of 35 UT1–UTC spectral components (20%) show smallest residuals using IGG Bonn. The IERS2010 model again performs well in this comparison, improving 27% or 28 of all ERP components.

The baseline length repeatability for all four models is compared as well. Figure 6.6 shows differences in baseline scatter. If the number of improved baselines is compared, there can be found a slightly different result than is indicated by the spectral comparison. The IGG Bonn model still performs best, i.e., shows the smallest baseline length standard deviation for the majority of baselines. The FF5 model shows results similar to the remaining two models and improves 64 (40%) of all 161 baselines. Models FES2012 and IERS2010 are slightly more accurate and improve 68 (42%) and 66 (41%) baselines, respectively. The number of improved baselines with respect to the reference IGG Bonn is shown in Table 6.4.

Thus, model FF5 performs similarly as the IERS conventional model with respect to the re-

Table 6.4: Number of baselines for which the baseline length repeatability decreases (improves) or increases (degrade) if the high-frequency ERP model in the first column is used instead of the empirical IGG Bonn model. EOT11a FF5 denotes the model derived from EOT11a, supplemented by minor tides through OTAM admittance interpolation.

Model	Improved baselines	Degraded baselines
FES2012	68	93
IERS2010	66	95
EOT11a FF5	64	97

peatability of VLBI baselines between 2011 and 2013. The performance is, furthermore, slightly superior to the one based on the assimilation ocean tide model FES2012. The majority of baselines, however, is improved when the empirical ERP model IGG Bonn is used in VLBI analysis.

Chapter 7

Summary and conclusions

Accurate predictions of short-period Earth rotation variations are required for the analysis of space geodetic techniques, especially when parameters are fixed to a priori values due to sparse observations. In addition, studies in this field extend the knowledge of geophysical processes leading to irregularities of Earth rotation. The main part of these high-frequency variations are due to ocean tides. Global and accurate observations of the ocean surface are available from satellite altimetry observations which have been used to deduce the standard prediction model of ERP mentioned in the IERS Conventions 2010. However, this model has deficiencies which might lead to biases in geodetic products. Therefore, an updated model of (semi-)diurnal ERP variations is desired, in order to reduce the systematic discrepancies between observations and predictions. The main goal of the present thesis is to contribute to such a new high-frequency ERP model based on ocean tides. A secondary objective is to verify, if an empirical ocean tide model, being the most independent source of data for this task, can be used to derive accurate ERP prediction values.

Empirical ocean tide models do not include any hydrodynamic assumptions and, thus, lack of oceanic currents. The information of the flow is, however, required to compute the motion term of angular momentum. In order not to introduce any inconsistencies, tidal currents should be derived consistently with the given tidal height field. The estimation of oceanic currents from measured elevations is, therefore, one important and major task of the present thesis. The simple approach, described by Ray (2001), uses simplified hydrodynamic equations and continuity constraints solved in one global inversion process.

Both velocity amplitudes and phases show a very good mutual agreement in a comparison of the inversion algorithm and hydrodynamic models. One issue is the noise in tidal heights of the ocean surface. The high-frequency alternating elevation data map into estimated volume transports and, due to the gradient operator in the hydrodynamic equation, cause even increased noise in the results. This is one likely reason why the weight on the continuity equation in the inversion process is a crucial factor for the accuracy of the estimates. On the OTAM level, results can be easily compared to those from hydrodynamic ocean tide models.

The comparison of resultant OTAM values indicates the necessity for different weights for

different components. Equatorial components of diurnal tides require a large weight of 10000 compared to weights between 400 and 800 for the polar component. Semi-diurnal tides require equatorial weights between 100 and 200, polar components should be weighted between 400 and 2000, depending on tidal constituent.

The use of different weights, i.e., different inversion solutions, for the final set of OTAM values are a drawback of the presented model, especially due to the fact that model consistency is reduced. However, the RMS values of OTAM differ by 40% or more between weights of 400 and 10000. This difference is presumed to be too much as the majority of components between two hydrodynamic assimilation models agree within 10%. If variable weights are used, OTAM values from estimated volume transports and assimilation models differ by 4.7–19.7% (mean over x, y, and z component).

The empirical ocean tide model EOT11a includes tidal height variations of nine tidal constituents. However, additional minor partial tides have a significant effect on OTAM values and, therefore, have to be included in the computation. A widely used method is to interpolate minor tides using the ratio of tidal height and tidal potential which is assumed to be a smooth function of frequency. This work uses another approach: OTAM values instead of tidal heights are interpolated similarly to classical admittance interpolations. Thus, ratios of OTAM and tidal potential are interpolated quadratically to derive a final model including the effect of minor tides.

Several models including different sets of minor tides are developed and used in the analysis of VLBI observations. Best results are found when ten minor tides are included additionally to the nine major tides Q_1 , O_1 , P_1 , K_1 , $2N_2$, N_2 , M_2 , S_2 , and K_2 of EOT11a.

7.1 Discussion of validation results

For the validation, several ERP prediction models are applied a priori in the analysis of VLBI observations using the Vienna VLBI Software VieVS. These are (1) FES2012, a model based on a recent hydrodynamic assimilation ocean tide model including 27 tidal constituents; (2) the standard model mentioned in the IERS Conventions 2010, for which an updated model is highly desirable; (3) the empirical model IGG Bonn, deduced from GPS and VLBI observations and, therefore, presumed to yield smallest residuals; and (4) model EOT11a FF5 based on empirical ocean tides supplemented by ten minor tides derived from quadratic admittance interpolation of OTAM values. Tidal currents of major tides are estimated using the inversion algorithm.

High-frequency ERP are estimated from VLBI observations between 2011 and 2013 using the four a priori models. Differences of ERP residuals spectra indicate, as expected, that model IGG Bonn represents the smallest residuals. The FES2012 model, similar to EOT11a FF5, shows larger discrepancies at frequencies of several major tides, such as O_1 , K_1 , or M_2 . Still, the newly derived model yields, together with IGG Bonn, the largest number of smallest spectral amplitudes. The IERS conventional model is similarly accurate in this comparison, showing smallest ERP residual spectral amplitudes for 27% of all components (IGG Bonn, EOT11a FF5: 28%).

However, a more external validation can be performed using standard deviations of baseline lengths. Even though differences of repeatabilities are small, they are a good measure of model accuracy. The empirical model IGG Bonn improves the majority of baselines and can, therefore, be assumed to be the most accurate ERP prediction model from this comparison. The model EOT11a FF5 performs slightly worse than both FES2012 and the conventional model, improving 64 (40%) of 161 baselines compared to IGG Bonn. FES2012 (68 or 42% improved baselines) and IERS2010 (66 or 41% improved baselines) show larger numbers when comparing baseline length repeatabilities.

7.2 Concluding remarks and outlook

It is shown that an empirical ocean tide model can serve as independent source for the development of an accurate ERP prediction model. The approach for the derivation of oceanic currents presented by Ray (2001) is adequate for the task of determining motion terms of angular momentum. The number of tides available in EOT11a is, however, not sufficient so that additional tidal constituents have to be derived using admittance assumptions. The transfer from interpolating OTAM values instead of tidal heights is shown to be feasible in order to include the effect of minor tides. Nevertheless, empirical estimation of minor tides from altimetry would be preferable to interpolation.

A loss of consistency is clearly introduced due to the use of different continuity equation weights for the final set of angular momentum. If the main reason for large weights is noise in tidal heights, revised ocean tide models might allow the use of more consistent weights in the OTAM determination. The derived model EOT11a FF5 is on the same level of accuracy as other models with respect to VLBI baseline length repeatabilities and spectral comparison for the chosen time period and might serve as updated and independent prediction model of ERP variations in the analysis of space geodetic techniques. Empirical ERP models are still superior to those based on ocean models, however, with the disadvantage of possibly overlaying other geophysical effects.

Finally, it is worth mentioning that the analysis of ERP residuals need not draw the same conclusions as an external validation. In the present validation, model EOT11a FF5 improves the lowest number of baselines but yields, together with IGG Bonn, most smallest residual amplitudes in comparison with the other models.

The validation in this thesis covers three years of VLBI observations. However, as VLBI telescopes have been observing since 1979, a longer time span for the comparison is by all means desirable. Empirical models from only one space geodetic technique do not fully agree in inter-technique comparisons, a validation using other techniques is, therefore, inevitable. A model validation by GNSS is even more important, because polar motion products of the IERS are mostly based on observations from satellite systems.

Satellite altimetry will undergo further improvements in the next years, from more precise observations, to enhanced analysis strategies, and also revised available geophysical models. This,

7.2 Concluding remarks and outlook

in turn, will also facilitate the derivation of more accurate independent Earth rotation models for improved scientific products and a better understanding of processes in geodesy and geophysics.

Appendix A

Auxiliary material

Table A.1: Polar motion variation coefficients for model FF5 based on EOT11a. In addition to nine tides included in the ocean tide model, OTAM values of ten minor tides are derived from quadratic admittance interpolation. Details about this model FF5 is given in Table 5.8.

Tide	Delaunay arguments						Doodson number	Period (hours)	$x_p \sin$ (μas)	$x_p \cos$ (μas)	$y_p \sin$ (μas)	$y_p \cos$ (μas)
	γ	l	l'	F	D	Ω						
	1	-1	0	-2	0	-1	135.645	26.8728	-1.5	11.2	-11.2	-1.5
Q ₁	1	-1	0	-2	0	-2	135.655	26.8684	10.3	30.5	-30.5	10.3
ρ_1	1	1	0	-2	-2	-2	137.455	26.7231	-1.3	10.7	-10.7	-1.3
O ₁	1	0	0	-2	0	-2	145.555	25.8193	65.1	146.1	-146.1	65.1
	1	1	0	-2	0	-2	155.455	24.8492	1.5	-7.3	7.3	1.5
P ₁	1	0	0	-2	2	-2	163.555	24.0659	28.1	40.3	-40.3	28.1
	1	0	0	0	0	1	165.545	23.9380	0.4	7.1	-7.1	0.4
K ₁	1	0	0	0	0	0	165.555	23.9345	-113.0	-158.0	158.0	-113.0
	1	0	0	0	0	-1	165.565	23.9310	-2.8	-48.8	48.8	-2.8
OO ₁	1	0	0	2	0	2	185.555	22.3061	-17.5	-8.1	8.1	-17.5
	1	0	0	2	0	1	185.565	22.3030	-11.2	-5.2	5.2	-11.2
2N ₂	2	-2	0	-2	0	-2	235.755	12.9054	-6.6	-0.9	1.1	4.0
μ_2	2	0	0	-2	-2	-2	237.555	12.8718	-6.8	1.3	0.0	-0.1
N ₂	2	-1	0	-2	0	-2	245.655	12.6583	-49.0	-8.7	3.9	33.2
	2	0	0	-2	0	-1	255.545	12.4215	10.1	-4.3	-1.1	7.7
M ₂	2	0	0	-2	0	-2	255.555	12.4206	-282.1	-24.6	51.1	167.8
L ₂	2	1	0	-2	0	-2	265.455	12.1916	8.3	1.0	-0.6	7.2
S ₂	2	0	0	-2	2	-2	273.555	12.0000	-132.3	53.1	56.1	84.3
K ₂	2	0	0	0	0	0	275.555	11.9672	-38.0	12.7	15.5	21.4

Table A.2: UT1 and LOD variation coefficients for model FF5 based on EOT11a. In addition to nine tides included in the ocean tide model, OTAM values of ten minor tides are derived from quadratic admittance interpolation. Details about this model FF5 is given in Table 5.8.

Tide	Delaunay arguments						Doodson number	Period (hours)	UT1		LOD	
	γ	l	l'	F	D	Ω			sin (μ s)	cos (μ s)	sin (μ s)	cos (μ s)
	1	-1	0	-2	0	-1	135.645	26.8728	-0.4	-0.4	-2.1	2.1
Q_1	1	-1	0	-2	0	-2	135.655	26.8684	3.8	-1.9	-10.8	-21.5
ρ_1	1	1	0	-2	-2	-2	137.455	26.7231	-0.4	-0.4	-2.1	2.1
O_1	1	0	0	-2	0	-2	145.555	25.8193	12.6	-10.0	-58.1	-73.4
	1	1	0	-2	0	-2	155.455	24.8492	0.1	0.2	1.1	-0.6
P_1	1	0	0	-2	2	-2	163.555	24.0659	3.8	-2.4	-14.8	-24.0
	1	0	0	0	0	1	165.545	23.9380	-0.2	-0.2	-1.0	1.3
K_1	1	0	0	0	0	0	165.555	23.9345	-13.2	8.0	50.5	83.2
	1	0	0	0	0	-1	165.565	23.9310	1.5	1.1	7.0	-9.3
OO_1	1	0	0	2	0	2	185.555	22.3061	2.0	0.7	4.4	-13.5
	1	0	0	2	0	1	185.565	22.3030	1.3	0.4	2.9	-8.8
$2N_2$	2	-2	0	-2	0	-2	235.755	12.9054	-0.4	-0.4	-4.3	5.1
μ_2	2	0	0	-2	-2	-2	237.555	12.8718	-0.5	0.5	6.4	6.0
N_2	2	-1	0	-2	0	-2	245.655	12.6583	-2.7	-2.2	-25.7	32.0
	2	0	0	-2	0	-1	255.545	12.4215	0.6	-0.7	-8.7	-7.1
M_2	2	0	0	-2	0	-2	255.555	12.4206	-14.9	-6.9	-84.1	181.1
L_2	2	1	0	-2	0	-2	265.455	12.1916	0.3	-0.1	-0.6	-4.1
S_2	2	0	0	-2	2	-2	273.555	12.0000	-8.0	-1.8	-22.1	100.1
K_2	2	0	0	0	0	0	275.555	11.9672	-2.1	-0.3	-4.1	26.6

Table A.3: Number of tidal frequencies where the respective model gives smallest spectral amplitudes.

Model	Smallest residuals			
	X-pole	Y-pole	UT1–UTC	Total
FES2012	10	5	4	19
IERS2010	6	12	10	28
IGG Bonn	10	12	7	29
EOT11a FF5	9	6	14	29

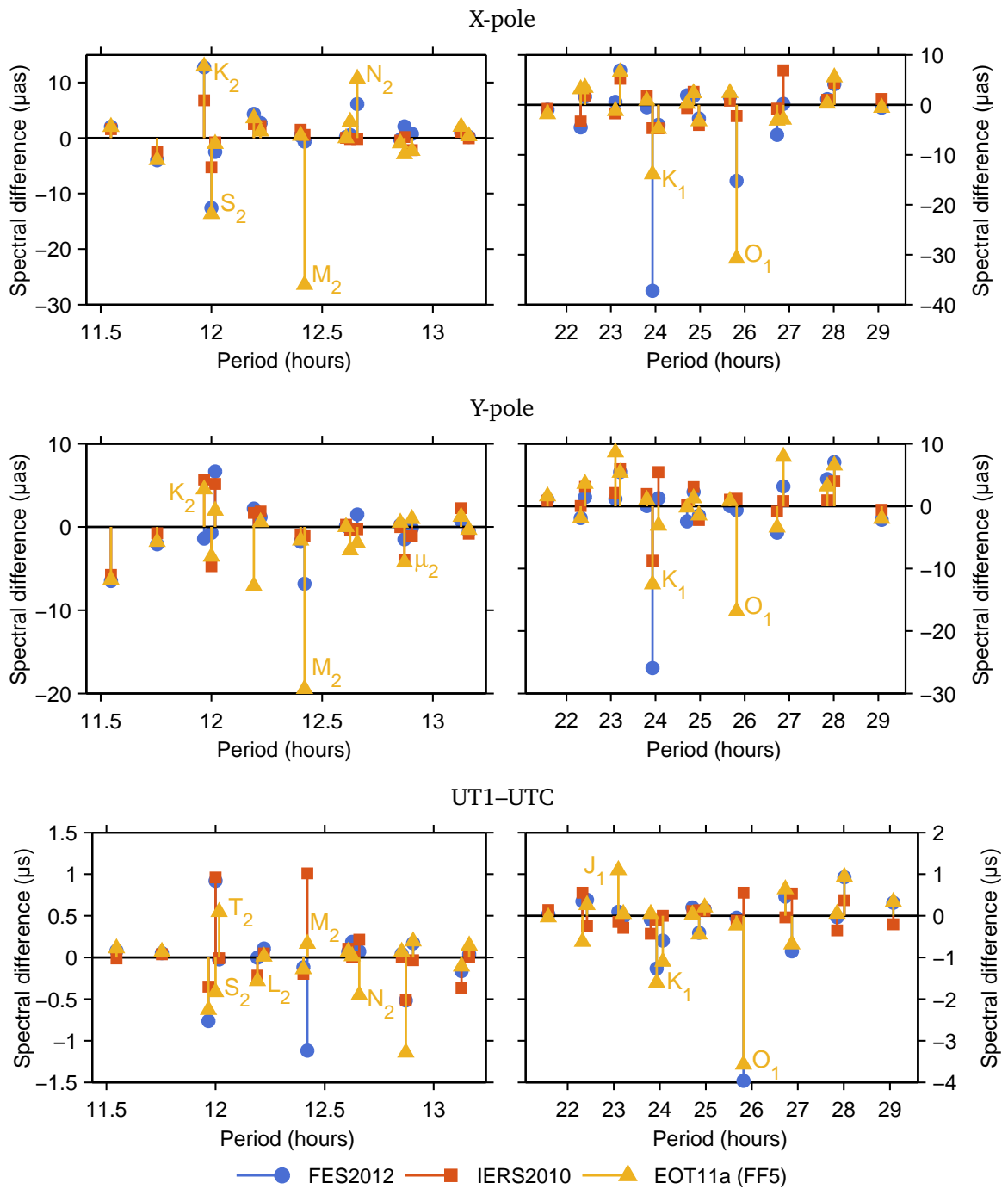


Figure A.1: Amplitude spectra differences of ERP residuals from a VLBI solution using different high-frequency ERP models. Positive values indicate smaller ERP residuals and, thus, more accurate prediction values compared to a reference model. Reference is the empirical IGG Bonn model.

List of Figures

2.1	Frequency convention of the CIP	8
2.2	Observed LOD variations from the combined IERS C04 time series	9
2.3	Observed polar motion variations from the combined IERS C04 time series	10
2.4	Geometric principle of VLBI	16
3.1	Illustration of the tidal force	22
3.2	Illustration of some spherical harmonics.	25
3.3	Tidal potential amplitudes from the HW95 catalog	27
3.4	Tidal height variations from HAMTIDE11a	35
4.1	Equilibrium tides at $t = 0$ for K_1 and M_2	42
4.2	Green's function values for vertical displacement	44
4.3	Self-attraction and loading (SAL) tides for K_1 and M_2	45
4.4	Layout of finite difference C-grid	45
4.5	Sparsity pattern of design matrix	46
4.6	Validation of inversion algorithm for K_1	48
4.7	Validation of inversion algorithm for M_2	49
4.8	Latitude profile of tidal height amplitudes of K_1	50
4.9	Latitude profile of tidal height amplitudes of M_2	50
4.10	RMS of estimated M_2 volume transports	51
4.11	GEBCO bathymetry	52
4.12	Bathymetry differences	53
4.13	Comparison of inversion results using different bathymetries	54
5.1	Comparison of OTAM from oceanic currents	62
5.2	Volume transports of O_1 and K_1 from the inversion algorithm	64
5.3	Volume transports of M_2 and S_2 from the inversion algorithm	65
5.4	Phasor diagrams of OTAM from several ocean tide models	69
5.5	Phasor diagrams for ERP variations for eight major tidal constituents	72
5.6	Admittance theory for the interpolation of OTAM mass term	75
5.7	Admittance theory for the interpolation of OTAM motion term	76

6.1	VLBI network of IVS R1 and R4 sessions	88
6.2	VLBI network of IVS CONT11 sessions	88
6.3	ERP estimates of 297 VLBI sessions between 2011 and 2013 and corresponding amplitude spectra	91
6.4	Amplitude spectra differences of ERP residuals from a VLBI solution using different high-frequency ERP models	92
6.5	Baseline length repeatability from 297 VLBI sessions	93
6.6	Baseline length repeatability differences of three models with respect to IGG Bonn .	95
A.1	Amplitude spectra differences of ERP residuals with respect to IGG Bonn	103

List of Tables

3.1	Doodson arguments	27
3.2	Fundamental (Delaunay) arguments	28
3.3	Largest tidal harmonics	30
3.4	Tidal constituents included in selected ocean tide models	33
4.1	Astronomical amplitudes and Love number factors for the calculation of the equilibrium tide	42
4.2	Median RMS values for the comparison of volume transports using different bathymetries	54
4.3	Relative RMS values for the comparison of OTAM using different bathymetries	55
4.4	Comparison of derived OTAM values	56
4.5	Comparison of relaxing factors for the no-flow boundary condition	57
4.6	Influence of weighting of the continuity equation	58
4.7	Proper weights from the “calibration” experiments for the continuity equation	59
5.1	Applied weights for the continuity equation in the least-squares adjustment	63
5.2	OTAM derived from the empirical ocean tide model EOT11a	66
5.3	OTAM from the assimilation model HAMTIDE11a	67
5.4	OTAM from the assimilation model FES2012	68
5.5	Relative RMS values of OTAM motion terms	68
5.6	Polar motion variation coefficients for nine major tides based on EOT11a	70
5.7	UT1 and LOD variation coefficients for nine major tides based on EOT11a	70
5.8	Overview of ERP models derived from the empirical ocean tide model EOT11a	71
5.9	Admittance interpolation coefficients for the five largest diurnal tides not included in EOT11a	74
5.10	Admittance interpolation coefficients for the six largest semi-diurnal tides not included in EOT11a	75
5.11	Comparison of OTAM derived from three alternative ways	78
5.12	Pivot waves for quadratic admittance interpolation	79
5.13	Weights on the continuity equation for the OTAM interpolation of minor tides	80
5.14	OTAM of minor tides from the empirical ocean tide model EOT11a	81

5.15	Polar motion variation coefficients for 28 tides based on EOT11a	82
5.16	UT1 and LOD variation coefficients for 28 tides tides based on EOT11a	83
6.1	Parametrization of the VLBI analysis for the validation of the ERP model	89
6.2	Number of tidal frequencies where the respective model gives smallest spectral amplitudes	93
6.3	Comparison of baseline length repeatabilities with respect to the IERS model	94
6.4	Comparison of baseline length repeatabilities with respect to the IGG Bonn model .	96
A.1	Polar motion variation coefficients for model FF5	101
A.2	UT1 and LOD variation coefficients for model FF5	102
A.3	Number of tidal frequencies where the respective model gives smallest spectral amplitudes	102

Acronyms

μas	Microarcseconds
μs	Microseconds
BIH	Bureau International de l'Heure
BTS	BIH Terrestrial System
CEP	Celestial ephemeris pole
CIP	Celestial intermediate pole
CONT	Continuous VLBI campaign
cpsd	Cycles per sidereal day
CRS	Celestial reference system
CW	Chandler wobble
cy	Century
DORIS	Doppler Orbitography Radiopositioning Integrated by Satellites
EOP	Earth orientation parameters
ERP	Earth rotation parameters
ESA	European Space Agency
FCN	Free Core Nutation
GEBCO	General Bathymetric Chart of the Oceans
GGOS	Global Geodetic Observing System
GLONASS	Globalnaja Nawigazionnaja Sputnikowaja Sistema
GMST	Greenwich mean sidereal time
GNSS	Global Navigation Satellite Systems
GPS	Global Positioning System
IAU	International Astronomical Union
ICRF	International Celestial Reference Frame
IERS	International Earth Rotation and Reference Systems Service

IGS	International GNSS Service
ITRF	International Terrestrial Reference Frame
ITRS	International Terrestrial Reference System
IVS	International VLBI Service for Geodesy and Astrometry
LLR	Lunar Laser Ranging
LOD	Length-of-day
mas	Milliarcseconds
ms	Milliseconds
NNR	No-net rotation
NNT	No-net translation
OTAM	Oceanic tidal angular momentum
ppb	Parts per billion
RFI	Radio Frequency Interference
RMS	Root mean square
SLR	Satellite Laser Ranging
SRTM	Shuttle Radar Topography Mission
SSB	Sea state bias
SSH	Sea surface height
SWH	Significant wave height
TCB	Barycentric Coordinate Time
TRF	Terrestrial reference frame
TRS	Terrestrial reference system
UT1	Universal Time 1
UTC	Universal Time Coordinated
VGOS	VLBI2010 Global Observing System
VLBI	Very Long Baseline Interferometry
VMF	Vienna Mapping Functions

Bibliography

- ACCAD, Y. AND PEKERIS, C.L. (1978). Solution of the tidal equations for the M_2 and S_2 tides in the world oceans from a knowledge of the tidal potential alone. *Philosophical Transactions of the Royal Society of London. Series A, Mathematical and Physical Sciences*, 290, No. 1368, 235–266.
- AGNEW, D.C. (2007). Earth Tides. In T. Herring, ed., *Treatise on Geophysics, Volume 3*, 163–195, Elsevier.
- ALTAMIMI, Z., COLLILIEUX, X. AND MÉTIVIER, L. (2011). ITRF2008: an improved solution of the international terrestrial reference frame. *Journal of Geodesy*, 85, 457–473.
- ANGERMANN, D., SEITZ, M. AND DREWES, H. (2013). Global terrestrial reference systems and their realizations. In G. Xu, ed., *Sciences of Geodesy - II*, Vol. 24, 97–132, Springer-Verlag Berlin Heidelberg.
- ARAKAWA, A. AND LAMB, V.R. (1977). Computational design of the basic dynamical processes of the UCLA general circulation model. *Methods of Computational Physics*, 17, 173–265.
- ARBIC, B. (2005). Atmospheric forcing of the oceanic semidiurnal tide. *Geophysical Research Letters*, 32, L02610, doi:10.1029/2004GL021668.
- ARBIC, B.K., GARNER, S.T., HALLBERG, R.W. AND SIMMONS, H. (2004). The accuracy of surface elevations in forward global barotropic and baroclinic tide models. *Deep-Sea Research II*, 51, 3069–3101, doi:10.1016/j.dsr2.2004.09.014.
- ARTZ, T. (2011). *Determination of Sub-daily Earth Rotations Parameters from VLBI Observations*. Ph.D. thesis, Universität Bonn.
- ARTZ, T., TESMER NÉE BÖCKMANN, S. AND NOTHNAGEL, A. (2011). Assessment of periodic sub-diurnal Earth rotation variations at tidal frequencies through transformation of VLBI normal equation systems. *Journal of Geodesy*, 85, 565–584.
- ARTZ, T., BERNHARD, L., NOTHNAGEL, A., STEIGENBERGER, P. AND TESMER, S. (2012). Methodology for the combination of sub-daily Earth rotation from GPS and VLBI observations. *Journal of Geodesy*, 86, 221–239.

- BECKER, J.J., SANDWELL, D.T., SMITH, W.H.F., BRAUD, J., BINDER, B., DEPNER, J., FABRE, D., FACTOR, J., INGALLIS, S., KIM, S.H., LADNER, R., MARKS, K., NELSON, S., PHARAOH, A., TRIMMER, R., VON ROSENBERG, J., WALLACE, G. AND WEATHERALL, P. (2009). Global Bathymetry and Elevation Data at 30 Arc Seconds Resolution: SRTM30_PLUS. *Marine Geodesy*, 32:4, 355–371.
- BEUTLER, G., MERVART, L. AND VERDUN, A. (2005). *Methods of Celestial Mechanics, Volume II: Application to Planetary System, Geodynamics and Satellite Geodesy*. Springer.
- BÖHM, J., BÖHM, S., NILSSON, T., PANY, A., PLANK, L., SPICAKOVA, H., TEKE, K. AND SCHUH, H. (2012). The new Vienna VLBI Software VieVS. In S. Kenyon, M.C. Pacino and U. Marti, eds., *Proceedings of IAG Scientific Assembly 2009*, Vol. 136, 1007–1011, International Association of Geodesy.
- BÖHM, S. (2012). *Tidal excitation of Earth rotation observed by VLBI and GNSS*. Ph.D. thesis, Vienna University of Technology.
- BLEWITT, G. (2007). GPS and Space-Based Geodetic Methods. In T. Herring, ed., *Treatise on Geophysics, Volume 3*, 351–390, Elsevier.
- BOSCH, W., SAVCENKO, R., FLECHTNER, F., DAHLE, C., MAYER-GÜRR, T., STAMMER, D., TAGUCHI, E. AND ILK, K.H. (2009). Residual ocean tide signals from satellite altimetry, GRACE gravity fields, and hydrodynamic modeling. *Geophysical Journal International*, 178, 1185–1192.
- BOSCH, W., DETTMERING, D., SCHWATKE, C. AND PANZETTA, F. (2014). Case-study on minor tides – modeling, computation or estimation? Poster, OSTST Meeting, 22-31 October, Konstanz, Germany.
- BROSCHE, P., SEILER, U., WÜNSCH, J. AND SUENDERMANN, J. (1989). Periodic changes in Earth's rotation due to oceanic tides. *Astronomy and Astrophysics*, 220, 318–320.
- BRZEZIŃSKI, A. (2012). On estimation of high frequency geophysical signals in Earth rotation by complex demodulation. *Journal of Geodynamics*, 62, 74–82.
- BRZEZIŃSKI, A. AND CAPITAINE, N. (2011). The use of the precise observations of the celestial ephemeris pole in the analysis of geophysical excitation of Earth rotation. *Journal of Geodesy*, 85, 457–473.
- BRZEZIŃSKI, A. AND NASTULA, J. (2002). Oceanic excitation of the Chandler wobble. *Advances in Space Research*, 30, 195–200.
- CAPITAINE, N. (2000). Definition of the Celestial Ephemeris Pole and the Celestial Ephemeris Origin. In K. Johnston, D. McCarthy, B. Luzum and G. Kaplan, eds., *Towards Models and Constants for Sub-microarcsecond Astrometry*, Proceedings of IAU colloquium 180, 153–163, Washington, DC : U.S. Naval Observatory.

- CARRÈRE, L. AND LYARD, F. (2003). Modeling the barotropic response of the global ocean to atmospheric wind and pressure forcing – comparisons with observations. *Geophysical Research Letters*, 30.
- CARRÈRE, L., LYARD, F., CANCEL, M., GUILLOT, A. AND ROBLOU, L. (2012). FES2012: A new global tidal model taking advantage of nearly 20 years of altimetry. In L. Ouwehand, ed., *Proceedings of 20 Years of Progress in Radar Altimetry*, ESA, Venice, Italy, ISBN 978-92-9221-274-2.
- CARTWRIGHT, D.E., RAY, R.D. AND SANCHEZ, B.V. (1992). A Computer Program for Predicting Oceanic Tidal Currents. NASA Technical Memorandum 104578. Goddard Space Flight Center, Greenbelt, Maryland 20771, USA.
- CHAO, B.F. AND RAY, R.D. (1997). Oceanic tidal angular momentum and Earth's rotation variations. *Progress in Oceanography*, 40, 399–421.
- CHAO, B.F., RAY, R.D., GIPSON, J.M., EGBERT, G.D. AND MA, C. (1996). Diurnal/semidiurnal polar motion excited by oceanic tidal angular momentum. *Journal of Geophysical Research*, 101, 20151–20163.
- DAHLEN, F.A. (1976). The passive influence of the oceans upon the rotation of the Earth. *Geophysical Journal of the Royal Astronomical Society*, 46, 363–406.
- DEFRAIGNE, P. AND SMITS, I. (1999). Length of day variations due to zonal tides for an inelastic earth in non-hydrostatic equilibrium. *Geophysical Journal International*, 139, 563–572.
- DEHANT, V. AND MATHEWS, P.M. (2007). Earth Rotation Variations. In T. Herring, ed., *Treatise on Geophysics, Volume 3*, 295–349, Elsevier.
- DEHANT, V. AND MATHEWS, P.M. (2015). *Precession, Nutation and Wobble of the Earth*. Cambridge University Press.
- DICK, W.R. AND THALLER, D., eds. (2014). *IERS Annual Report 2012*. International Earth Rotation and Reference Systems Service, Central Bureau, Verlag des Bundesamts für Kartographie und Geodäsie, Frankfurt am Main.
- DICKMAN, S.R. (1993). Dynamic ocean-tide effects on Earth's rotation. *Geophysical Journal International*, 112, 448–470.
- DICKMAN, S.R. (2003). Evaluation of "effective angular momentum function" formulations with respect to core-mantle coupling. *Journal of Geophysical Research*, 108(B3), 2150, doi:10.1029/2001JB001603.
- DICKMAN, S.R. (2005). Rotationally consistent Love numbers. *Geophysical Journal International*, 161, 31–40.

- DOODSON, A.T. (1921). The Harmonic Development of the Tide-Generating Potential. *Proceedings of the Royal Society of London*, 100.
- DOODSON, A.T. AND WARBURG, H.D. (1941). *Admiralty manual of tides*. Hydrographic department, Admiralty.
- EGBERT, G.D. AND BENNETT, A.F. (1996). Data assimilation methods for ocean tides. In P. Malanotte-Rizzoli, ed., *Modern Approaches to Data Assimilation in Ocean Modeling*, Vol. 61 of *Elsevier Oceanography Series*, 147 – 179, Elsevier.
- EGBERT, G.D. AND EROFEEVA, S.Y. (2002). Efficient Inverse Modeling of Barotropic Ocean Tides. *Journal of Atmospheric and Oceanic Technology*, 19, 183–204.
- EGBERT, G.D., BENNETT, A.F. AND FOREMAN, M.G.G. (1994). TOPEX/POSEIDON tides estimated using a global inverse model. *Journal of Geophysical Research*, 99(C12), 24821–24852, doi:10.1029/94JC01894.
- ENGELN-MÜLLGES, G., NIEDERDRENK, K. AND WODICKA, R. (2011). *Numerik-Algorithmen*. Springer, Berlin Heidelberg.
- EUBANKS, T.M. (1993). Variations in the orientation of the Earth. In D.E. Smith and D.L. Turcotte, eds., *Contributions of Space Geodesy to Geodynamics: Earth Dynamics*, Vol. 24, 1–54, American Geophysical Union, Washington D.C.
- FARRELL, W.E. (1973). Earth Tides, Ocean Tides and Tidal Loading. *Philosophical Transactions of the Royal Society of London. Series A, Mathematical and Physical Sciences*, 274, 253–259.
- FEY, A.L., GORDON, D. AND JACOBS, C.S. (2009). *The Second Realization of the International Celestial Reference Frame by Very Long Baseline Interferometry*. IERS Technical Note No. 35, Verlag des Bundesamts für Kartographie und Geodäsie, Frankfurt am Main.
- FOK, H.S. (2012). Ocean Tides Modeling using Satellite Altimetry. Tech. Rep. 501, The Ohio State University, Columbus, Ohio 43210.
- FREEDEN, W. AND SCHREINER, M. (2009). *Spherical Functions of Mathematical Geosciences*. Springer-Verlag Berlin Heidelberg.
- GIPSON, J.M. (1996). Very long baseline interferometry determination of neglected tidal terms in high-frequency Earth orientation variation. *Journal of Geophysical Research*, 101(B12), 28051–28064, doi:10.1029/96JB02292.
- GROSS, R. (1993). The effect of ocean tides on the earth's rotation as predicted by the results of an ocean tide model. *Geophysical Research Letters*, 20, 293–296.
- GROSS, R. (2000). The excitation of the Chandler wobble. *Geophysical Research Letters*, 27, 2329–2332.

- GROSS, R. (2007). Earth Rotation Variations – Long Period. In T. Herring, ed., *Treatise on Geophysics, Volume 3*, 239–294, Elsevier.
- GROSS, R., FUKUMORI, I., MENEMENLIS, D. AND GEGOUT, P. (2004). Atmospheric and oceanic excitation of length-of-day variations during 1980–2000. *Journal of Geophysical Research*, 109.
- HAAS, R., SEKIDO, M., HOBIGER, T., KONDO, T., KURIHARA, S., TANIMOTO, D., KOKADO, K., WAGNER, J., RITAKARI, J. AND MUJUNEN, A. (2010). Ultra-rapid DUT1-observations with E-VLBI. *Artificial Satellites*, 45, Issue 2, 75–79.
- HARTMANN, T. AND WENZEL, G. (1995). The HW95 Tidal Potential Catalogue. *Geophysical Research Letters*, 22, 3553–3556.
- HENDERSHOTT, M.C. (1972). The Effects of Solid Earth Deformation on Global Ocean Tides. *Geophysical Journal of the Royal Astronomical Society*, 29, 389–402.
- HERRING, T.A. AND DONG, D. (1994). Measurement of diurnal and semidiurnal rotational variations and tidal parameters of Earth. *Journal of Geophysical Research*, 99(B9), 18051–18071.
- HOFMANN-WELLENHOF, B., LICHTENEGGER, H. AND WASLE, E. (2008). *GNSS – Global Navigation Satellite Systems*. Springer-Verlag, Wien.
- IGS (2013). IGS products webpage. <http://www.igs.org/products>, accessed: 2014-09-15.
- JAKOBSSON, M., MAYER, L., COAKLEY, B., DOWDESWELL, J.A., FORBES, S., FRIDMAN, B., HODNESDAL, H., NOORMETS, R., PEDERSEN, R., REBESCO, M., SCHENKE, H.W., ZARAYSKAYA, Y., ACCETTELLA, D., ARMSTRONG, A., ANDERSON, R.M., BIENHOFF, P., CAMERLENGHI, A., CHURCH, I., EDWARDS, M., GARDNER, J.V., HALL, J.K., HELL, B., HESTVIK, O., KRISTOFFERSEN, Y., MARCUSSEN, C., MOHAMMAD, R., MOSHER, D., NGHIEM, S.V., PEDROSA, M.T., TRAVAGLINI, P.G. AND WEATHERALL, P. (2012). The International Bathymetric Chart of the Arctic Ocean (IBCAO) Version 3.0. *Geophysical Research Letters*, 39.
- KANTHA, L.H. AND CLAYSON, C.A. (2000). Tides and tidal modeling. In L.H. Kantha and C.A. Clayson, eds., *Numerical Models of Oceans and Oceanic Processes*, Vol. 66 of *International Geophysics*, 375 – 492, Academic Press.
- KÄMPF, J., ed. (2010). *Advanced Ocean Modelling: Using Open-Source Software*. Springer.
- KOVALEVSKY, J., MUELLER, I.I. AND B., K., eds. (1989). *Reference Frames in Astronomy and Geophysics*. Kluwer Academic Publisher.
- KRÁSNÁ, H., BÖHM, J., PLANK, L., NILSSON, T. AND SCHUH, H. (2014). Atmospheric Effects on VLBI-Derived Terrestrial and Celestial Reference Frames. In C. Rizos and P. Willis, eds., *Earth on the Edge: Science for a Sustainable Planet*, Vol. 139 of *International Association of Geodesy Symposia*, 203–208, Springer Berlin Heidelberg.

- LAMBECK, K. (1980). *The Earth's variable rotation: Geophysical causes and consequences*. Cambridge University Press.
- LAMBECK, K. (1988). The Earth's variable rotation: some geophysical causes. In A.K. Babcock, ed., *The Earth's Rotation and Reference Frames for Geodesy and Geodynamics*, 1–20, International Astronomical Union.
- LE PROVOST, C., LYARD, F. AND MOLINES, J.M. (1991). Improving ocean tide predictions by using additional semidiurnal constituents from spline interpolation in the frequency domain. *Geophysical Research Letters*, 18(5), 845–848.
- LE PROVOST, C., LYARD, F., MOLINES, J., GENCO, M. AND RABILLOUD, F. (1998). A hydrodynamic ocean tide model improved by assimilating a satellite altimeter-derived data set. *Journal of Geophysical Research: Oceans*, 103, 5513–5529.
- LIAO, D., LIAO, X. AND ZHOU, Y. (2003). Oceanic and atmospheric excitation of the Chandler wobble. *Geophysical Journal International*, 152, 215–227.
- LOGUTOV, O.G. AND LERMUSIAUX, P.F.J. (2008). Inverse barotropic tidal estimation for regional ocean applications. *Ocean Modelling*, 25, 17–34.
- LYARD, F., LEFEVRE, F., LETELLIER, T. AND FRANCIS, O. (2006). Modelling the global ocean tides: modern insights from FES2004. *Ocean Dynamics*, 56, 394–415.
- MARKS, K.M. AND SMITH, W.H.F. (2006). An evaluation of publicly available global bathymetry grids. *Marine Geophysical Researches*, 27, 19–34.
- MATHEWS, P.M., BUFFETT, B.A., HERRING, T.A. AND SHAPIRO, I.I. (1991). Forced nutations of the Earth: Influence of inner core dynamics 2. Numerical results and comparisons. *Journal of Geophysical Research*, 96, 8243–8257.
- MAYER-GÜRR, T., SAVCENKO, R., BOSCH, W., DARAS, I., FLECHTNER, F. AND DAHLE, C. (2012). Ocean tides from satellite altimetry and GRACE. *Journal of Geodynamics*, 59–60, 28–38.
- MCCARTHY, D.D. AND PETIT, G. (2004). *IERS Conventions 2003*. IERS Technical Note No. 32, Verlag des Bundesamts für Kartographie und Geodäsie, Frankfurt am Main.
- MCCARTHY, D.D. AND SEIDELMANN, P.K. (2009). *Time – From Earth Rotation to Atomic Physics*. WILEY-VCH Verlag GmbH & Co. KGaA, Weinheim.
- MCINTOSH, P.C. AND BENNETT, A.F. (1984). Open Ocean Modeling as an Inverse Problem: M2 Tides in Bass Strait. *Journal of Physical Oceanography*, 14(3), 601–614.
- MIKHAIL, E.M. (1976). *Observations and Least Squares*. Thomas Y. Crowell Company, Inc.

- MIRABITO, C., DAWSON, C., KUBATKO, E.J., WESTERINK, J.J. AND BUNYA, S. (2011). Implementation of a discontinuous Galerkin morphological model on two-dimensional unstructured meshes. *Computer Methods in Applied Mechanics and Engineering*, 200.
- MÜLLER, M., CHERIAWSKY, J.Y., FOREMAN, M.G.G. AND VON STORCH, J.S. (2012). Global M_2 internal tide and its seasonal variability from high resolution ocean circulation and tide modeling. *Geophysical Research Letters*, 39, L19607.
- MÜLLER, P. AND VON STORCH, H. (2004). *Computer Modelling in Atmospheric and Oceanic Sciences*. Springer-Verlag Verlin Heidelberg.
- MORITZ, H. AND MUELLER, I. (1987). *Earth rotation: Theory and Observation*. Ungar.
- MUNK, W.H. AND CARTWRIGHT, D.E. (1966). Tidal Spectroscopy and Prediction. *Philosophical Transactions of the Royal Society of London. Series A, Mathematical and Physical Sciences*, 259, 533–581.
- MUNK, W.H. AND MACDONALD, G.J.F. (1960). *The Rotation of the Earth: A Geophysical Discussion*. Cambridge University Press.
- NIELL, A., WHITNEY, A., PETRACHENKO, B., SCHLÜTER, W., VANDENBERG, N., HASE, H., KOYAMA, Y., MA, C., SCHUH, H. AND TUCCARI, G. (2006). VLBI2010: Current and Future Requirements for Geodetic VLBI Systems. IVS Memorandum 2006-008v01, <ftp://ivscc.gsfc.nasa.gov/pub/memos/ivs-2006-008v01.pdf>.
- NILSSON, T., BÖHM, J. AND SCHUH, H. (2010). Sub-diurnal Earth Rotation Variations Observed by VLBI. *Artificial Satellites*, 45(2), 49–55, doi:10.2478/v10018-010-0005-8.
- PAIGE, C.C. AND SAUNDERS, M.A. (1982). LSQR: An Algorithm for Sparse Linear Equations and Sparse Least Squares. *ACM Transactions on Mathematical Software*, 8, No. 1, 43–71.
- PEROVIĆ, G. (2005). *Least Squares (Monograph)*. TON, Belgrade, Belgrade. ISBN: 86-907409-0-2.
- PETIT, G. AND LUZUM, B. (2010). *IERS Conventions*. IERS Technical Note No. 36, Verlag des Bundesamts für Kartographie und Geodäsie, Frankfurt am Main.
- PLAG, H.P., ALTAMIMI, Z., BETTADPUR, S., BEUTLER, G., BEYERLE, G., CAZENAVE, A., CROSSLEY, D., DONNELLAN, A., FORSBERG, R., GROSS, R., HINDERER, J., KOMJATHY, A., MA, C., MANNUCCI, A.J., NOLL, C., NOTHNAGEL, A., PAVLIS, E.C., PEARLMAN, M., POLI, P., SCHREIBER, U., SENIOR, K., WOODWORTH, P.L., ZERBINI, S. AND ZUFFADA, C. (2009). The goals, achievements, and tools of modern geodesy. In H.P. Plag and M. Pearlman, eds., *Global Geodetic Observing System - Meeting the Requirements of a Global Society on a Changing Planet in 2020*, 15–87, Springer, DOI: <http://doi.org/10.1007/978-3-642-02687-4>.

- POMA, A. (2000). The markowitz wobble. In S. Dick, D. McCarthy and B. Luzum, eds., *Polar Motion: Historical and Scientific Problems, ASP Conference Series*, Vol. 208, 351–354, Astronomical Society of the Pacific Conference Series.
- PONSAR, S., DEHANT, V., HOLME, R., JAULT, D., PAIS, A. AND VAN HOOLST, T. (2003). The core and fluctuations in the earth's rotation. In V. Dehant, ed., *Earth's Core: Dynamics, Structure, Rotation, Geodyn. Ser.*, Vol. 31, 251–261, AGU, Washington, D.C.
- PONTE, R.M. (1994). Understanding the relation between wind- and pressure-driven sea level variability. *Journal of Geophysical Research*, 99, 8033–8039.
- PUGH, D. AND WOODWORTH, P. (2014). *Sea-level science: Understanding tides, surges, tsunamis and mean sea-level changes*. Cambridge University Press.
- RAY, R.D. (1998). Ocean self-attraction and loading in numerical tidal models. *Marine Geodesy*, 21, 181–192, doi:10.1080/01490419809388134.
- RAY, R.D. (1999). A Global Ocean Tide Model From TOPEX/POSEIDON Altimetry: GOT99.2. NASA Tech. Memo. 209478, National Aeronautics and Space Administration.
- RAY, R.D. (2001). Inversion of oceanic tidal currents from measured elevations. *Journal of Marine Systems*, 28, 1–18.
- RAY, R.D. AND EGBERT, G.D. (2004). The Global S1 Tide. *Journal of Physical Oceanography*, 34, 1922–1935.
- RAY, R.D., STEINBERG, D.J., CHAO, B.F. AND CARTWRIGHT, D.E. (1994). Diurnal and semidiurnal variations in the earth's rotation rate induced by oceanic tides. *Science*, 264 (5160), 830–832, doi:10.1126/science.264.5160.830.
- RAY, R.D., EGBERT, G.D. AND EROFEEVA, S.Y. (2011). Tide predictions in shelf and coastal waters: Status and prospects. In S. Vignudelli, A.G. Kostianoy, P. Cipollini and J. Benveniste, eds., *Coastal Altimetry*, 191–216, Springer Berlin Heidelberg.
- ROBERTSON, R. (2001). Internal tides and baroclinicity in the southern Weddell Sea: Part II: Effects of the critical latitude and stratification. *Journal of Geophysical Research*, 106, 27017–27034.
- ROTHACHER, M., BEUTLER, G., HERRING, T.A. AND WEBER, R. (1999). Estimation of nutation using the Global Positioning System. *Journal of Geophysical Research*, 104, 4835–4859, doi:10.1029/1998JB900078.
- ROTHACHER, M., BEUTLER, G., WEBER, R. AND HEFTY, J. (2001). High-frequency variations in Earth rotations from Global Positioning System data. *Journal of Geophysical Research*, 106, 13711–13739.

- RUMMEL, R., BEUTLER, G., DEHANT, V., GROSS, R., ILK, K.H., PLAG, H.P., POLI, P., ROTHACHER, M., STEIN, S., THOMAS, R., WOODWARTH, P.L., ZEBINI, S. AND ZLOTNICKI, V. (2009). Understanding a dynamic planet: Earth science requirements for geodesy. In H.P. Plag and M. Pearlman, eds., *Global Geodetic Observing System - Meeting the Requirements of a Global Society on a Changing Planet in 2020*, 89–133, Springer, DOI: <http://doi.org/10.1007/978-3-642-02687-4>.
- SAVCENKO, R. AND BOSCH, W. (2012). EOT11a – Empirical ocean tide model from multi-mission satellite altimetry. Tech. Rep. 89, Deutsches Geodätisches Forschungsinstitut (DGFI), München, Germany.
- SCHINDELEGGER, M. (2013). *Atmosphere-induced short period variations of Earth rotation*. Ph.D. thesis, Vienna University of Technology.
- SCHINDELEGGER, M., BÖHM, S., BÖHM, J. AND SCHUH, H. (2013). Atmospheric effects on earth rotation. In J. Böhm and H. Schuh, eds., *Atmospheric Effects in Space Geodesy*, Springer-Verlag Berlin Heidelberg.
- SCHUH, H. AND BEHREND, D. (2012). VLBI: A fascinating technique for geodesy and astrometry. *Journal of Geodynamics*, 61, 68 – 80.
- SCHUH, H. AND BÖHM, J. (2013). Very long baseline interferometry for geodesy and astrometry. In G. Xu, ed., *Sciences of Geodesy - II*, Vol. 24, 339–376, Springer-Verlag Berlin Heidelberg.
- SEILER, U. (1991). Periodic changes of the angular momentum budget due to the tides of the world ocean. *Journal of Geophysical Research: Solid Earth*, 96, 10287–10300.
- SIMON, J.L., BRETAGNON, P., CHAPRONT, J., CHAPRONT-TOUZE, M., FRANCOU, G. AND LASKAR, J. (1994). Numerical expressions for precession formulae and mean elements for the Moon and the planets. *Astronomy and Astrophysics*, 282, no.2, 663–683.
- SMITH, M.L. AND DAHLEN, F.A. (1981). The period and Q of the Chandler wobble. *Geophysical Journal of the Royal Astronomical Society*, 64, 223–281.
- SMITH, W.H.F. AND SANDWELL, D.T. (1997). Global seafloor topography from satellite altimetry and ship depth soundings. *Science*, 277, 1957–1962.
- SOFFEL, M. AND LANGHANS, R. (2013). *Space-Time Reference Systems*. Springer-Verlag Berlin Heidelberg, 4th edn.
- SOFFEL, M., KLIONER, S.A., PETIT, G., WOLĘ P., KOPEIKIN, S.M., BRETAGNON, P., BRUMBERG, V.A., CAPITAINE, N., DAMOUR, T., FUKUSHIMA, T., GUINOT, B., HUANG, T.Y., LINDEGREN, L., MA1, C., NORDTVEDT, K., RIES, J.C., SEIDELMANN, P.K., VOKROUHLICKÝ, D., WILL, C.M. AND XU, C. (2003). The IAU 2000 Resolutions for Astrometry, Celestial Mechanics, and Metrology in the Relativistic Framework: Explanatory Supplement. *The Astronomical Journal*, 126, 2687–2706.

- SOVERS, O.J., FANSELOW, L. AND JACOBS, C. (1998). Astrometry and geodesy with radio interferometry: experiments, models, results. *Reviews of Modern Physics*, 70, 1393–1454, doi:10.1103/RevModPhys.70.1393.
- SPRINGER, T.A., BEUTLER, G. AND ROTHACHER, M. (1999). A New Solar Radiation Pressure Model for GPS Satellites. *GPS Solutions*, 2, 50–62.
- STAMMER, D., RAY, R.D., ANDERSEN, O.B., ARBIC, B.K., BOSCH, W., CARRÈRE, L., CHENG, Y., CHINN, D.S., DUSHAW, B.D., EGBERT, G.D., EROFEEVA, S.Y., FOK, H.S., GREEN, J.A.M., GRIFFITHS, S., KING, M.A., LAPIN, V., LEMOINE, F.G., LUTHCKE, S.B., LYARD, F., MORISON, J., MÜLLER, M., PADMAN, L., RICHMAN, J.G., SHRIVER, J.F., SHUM, C.K., TAGUCHI, E. AND YI, Y. (2014). Accuracy assessment of global barotropic ocean tide models. *Reviews of Geophysics*, 52, 243–282, doi:10.1002/2014RG000450.
- STEIGENBERGER, P. (2009). Reprocessing of a Global GPS Network. In *Deutsche Geodätische Kommission, Reihe C, Heft 640*, Verlag der Bayerischen Akademie der Wissenschaften, München.
- STEPANOV, V.N. AND HUGHES, C.W. (2004). Parameterization of ocean self-attraction and loading in numerical models of the ocean circulation. *Journal of Geophysical Research*, 109, C03037.
- STEWART, R. (2008). *Introduction to Physical Oceanography*.
- SVERDRUP, H.U., JOHNSON, M.W. AND FLEMING, R.H. (1942). *The Oceans, their physics, chemistry and general biology*. Prentice-Hall, Inc.
- TAGUCHI, E., STAMMER, D. AND ZAHTEL, W. (2014). Inferring deep ocean tidal energy dissipation from the global high-resolution data-assimilative HAMTIDE model. *Journal of Geophysical Research: Oceans*, 119, 4573–4592.
- TEKE, K., TANIR KAYIKCI, E., BÖHM, J. AND SCHUH, H. (2012). Modelling Very Long Baseline Interferometry (VLBI) observations. *Journal of Geodesy and Geoinformation*, 1, 17–26.
- TESCHL, G. (2014). *Mathematical methods in quantum mechanics*, Vol. 157 of *Graduate Studies in Mathematics*. American Mathematical Society, Providence, RI, 2nd edn.
- TESMER, V., KUTTERER, H., RICHTER, B. AND SCHUH, H. (2001). Reassessment of highly resolved EOP determined with VLBI. In A. Rius and D. Behrend, eds., *Proceedings of the 15th Working Meeting on European VLBI for Geodesy and Astrometry*, 83–90, Institut d’Estudis Espacials de Catalunya, Consejo Superior de Investigaciones Científicas.
- TORGE, W. AND MÜLLER, J. (2012). *Geodesy*. Walter de Gruyter, 4th edn.
- USGS (2004). Shuttle Radar Topography Mission, 30 Arc Second grid, Global Land Cover Facility, University of Maryland, College Park, Maryland, <http://www.landcover.org/data/srtm/>.

- VONDRÁK, J. (1999). Secular and long-periodic polar motion as derived from combination of astrometric and space geodetic observations. *Journées 1998 – Systèmes de référence spatio-temporels: Conceptual, conventional and practical studies related to Earth rotation*, 208, 195–201.
- WAHR, J.M. (1981). Body tides on an elliptical, rotating, elastic and oceanless earth. *Geophysical Journal of the Royal Astronomical Society*, 64, 677–703.
- WAHR, J.M. (1982). The effects of the atmosphere and oceans on the Earth's wobble – I. Theory. *Geophysical Journal of the Royal Astronomical Society*, 70, 349–372.
- WAHR, J.M. (2005). Polar motion models: Angular momentum approach. In H.P. Plag, B. Chao, R. Gross and T. Van Dam, eds., *Forcing of Polar Motion in the Chandler Frequency Band: A Contribution to Understanding Interannual Climate Change*, Vol. 24, 89–102, Luxembourg: Cahiers du Centre Européen de Géodynamique et de Séismologie.
- WAHR, J.M. AND SASAO, T. (1981). A diurnal resonance in the ocean tide and in the Earth's load response due to the resonant free 'core nutation'. *Geophysical Journal of the Royal Astronomical Society*, 64, 747–765.
- WAHR, J.M., SASAO, T. AND SMITH, M.L. (1981). Effect of the fluid core on changes in the length of day due to long period tides. *Geophysical Journal of the Royal Astronomical Society*, 64, 635–650.
- WATKINS, M. AND EANES, R. (1993). Diurnal and Semidiurnal Variations in Earth Orientation Determined from Lageos Laser Ranging. In H. Montag and C. Reigber, eds., *Geodesy and Physics of the Earth*, Vol. 112 of *International Association of Geodesy Symposia*, 400–403, Springer Berlin Heidelberg.
- WILSON, C.R. AND VICENTE, R.O. (1980). An analysis of the homogeneous ILS polar motion series. *Geophysical Journal of the Royal Astronomical Society*, 62, 605–616.
- WUNSCH, C., HAIDVOGEL, D.B., ISKANDARANI, M. AND HUGHES, R. (1997). Dynamics of the long-period tides. *Progress in Oceanography*, 40, 81–108.
- ZAHHEL, W. (1991). Modeling ocean tides with and without assimilating data. *Journal of Geophysical Research*, 96, 20379–20391.
- ZAHHEL, W. (1995). Assimilating ocean tide determined data into global tidal models. *Journal of Marine Systems*, 6, 3–13.

Curriculum vitae

Matthias Madzak, Dipl.-Ing., Proj. Ass.

Vienna University of Technology

Department of Geodesy and Geoinformation

Gußhausstraße 27–29, 1040 Vienna

E-mail: matthias.madzak@tuwien.ac.at

Tel.: +43 1 58801 12828

Date of birth: June 16, 1986

Place of birth: Vienna, Austria

University and education

03/2011 – 09/2015	Doctoral Program in Technical Sciences, Vienna University of Technology
02/2009 – 03/2011	Master Program Geodesy and Geophysics, Vienna University of Technology. Degree: Dipl.-Ing. (M.Sc., March 7, 2011). Thesis Title: <i>Externe troposphärische Korrekturen in der geodätischen VLBI</i>
10/2005 – 01/2009	Bachelor studies, Geodesy and Geoinformatics, Vienna University of Technology. Degree: Bakk.techn (B.Sc., February 19, 2009)
09/1996 – 06/2004	Grammar School, Bernoullistraße 3, 1220 Vienna

Employment record

03/2011 – present	Project assistant at the Vienna University of Technology, Institute of Geodesy and Geophysics
10/2009 – 12/2010	Project scientist (part-time) at the Vienna University of Technology, Institute of Photogrammetry and Remote Sensing